5-2021

Characterization of Si-MOSFETs for Terahertz Detection: Development for a Potential Future Astrophysical Sensor Technology

Katherine E. Seery
kes4610@rit.edu

Characterization of Si-MOSFETs for Terahertz Detection: Development for a Potential Future Astrophysical Sensor Technology

---

Ph.D. *Doctor of Philosophy*

in Astrophysical Sciences and Technology

Katherine E. Seery

School of Physics and Astronomy

Rochester Institute of Technology

Rochester, New York

May 2021

ASTROPHYSICAL SCIENCES AND TECHNOLOGY

COLLEGE OF SCIENCE

ROCHESTER INSTITUTE OF TECHNOLOGY

ROCHESTER, NEW YORK

Ph.D. DISSERTATION DEFENSE

Candidate: .....

Dissertation Title: .....

Adviser: .....

Date of defense: .....

The candidate's Ph.D. Dissertation has been reviewed by the undersigned. The Dissertation

(a) is acceptable, as presented.

(b) is acceptable, subject to minor amendments.

(c) is not acceptable in its current form.

Written details of required amendments or improvements have been provided to the candidate.

Committee:

Dr. Alan Raisanen, Committee Chair

Dr. Joel Kastner, Committee Member

Dr. Judy Pipher, Committee Member

Dr. Zoran Ninkov, Thesis Advisor

Please submit form to AST Graduate Program Coordinator

ASTROPHYSICAL SCIENCES AND TECHNOLOGY
COLLEGE OF SCIENCE
ROCHESTER INSTITUTE OF TECHNOLOGY
ROCHESTER, NEW YORK

CERTIFICATE OF APPROVAL

Ph.D. DEGREE DISSERTATION

The Ph.D. Degree Dissertation of *Katherine E. Seery* has been examined and approved by the dissertation committee as satisfactory for the dissertation requirement for the Ph.D. degree in Astrophysical Sciences and Technology.

Dr. Alan Raisanen, Committee Chair

Dr. Joel Kastner, Committee Member

Dr. Judy Pipher, Committee Member

Dr. Zoran Ninkov, Thesis Advisor

Date

Characterization of Si-MOSFETs for Terahertz Detection: Development for a Potential Future Astrophysical Sensor Technology

By

Katherine E. Seery

A dissertation submitted in partial fulfillment of the requirements for the degree of Ph.D. in Astrophysical Sciences and Technology, in the College of Science, Rochester Institute of Technology.

May, 2021

Approved by

Dr. Andrew Robinson	Date
Director, Astrophysical Sciences and Technology	

Abstract

Terahertz (THz) commonly refers to a region of the electromagnetic spectrum with frequencies ranging between 0.1 to 10 THz (wavelengths of 3 mm to 30 μm). The technology available for detection and generation in this spectral region has been less developed than in the adjoining infrared and visible domains. For the astronomy community, THz observation provides information related to various phenomena including, for example, the study of cosmic microwave background radiation (CMBR), emission from proto-planetary disks, and planetary atmospheric remote sensing. Many molecules have emission and absorption spectral features in the THz regime whose observation provides the ability to extract information on chemical composition, abundances, and environmental conditions.

Current detector technology utilized for THz astrophysics typically utilizes bolometers or kinetic inductance devices (KIDs) that must be cooled and are available in limited array size. Detectors that could be operated in a fashion similar to that available in the visible, both in format and array size, would be very welcome. Bow-tie antenna-coupled silicon metal oxide semiconductor field effect transistors (Si-MOSFETs) have shown promise in detecting THz radiation for terrestrial applications. They have been fabricated in array formats and scaling to formats of interest to astronomers is straightforward. However, the characterization of such devices is insufficient to determine if they could be operated and optimized to be useful in some astronomical applications.

This dissertation presents the characterization and analysis of such bow-tie antenna-coupled Si-MOSFETs designed for detection near 0.2 THz. Design parameters for the Si-MOSFETs,

such as antenna size and source region, were varied in devices manufactured using MOSIS foundry access. These devices were extensively tested in this work to determine the fabrication parameters providing optimal performance. An exploration of the detection mechanism for the devices and its consistency with the characterization results will also be presented. This characterization will include a study of the nonlinearity of these devices with incident power. The detector sensitivity and noise requirements for a small-scale space mission will be discussed and compared to the devices tested. Finally, a discussion on potential future development for these detectors will be provided.

Acknowledgements

This work was funded in part by New York State Foundation for Science, Technology, and Innovation (NYSTAR) and Harris Corporation. This work was done in collaboration with individuals from RIT, Harris Corporation, and the University of Rochester. Those at RIT include Zoran Ninkov (academic advisor) and Jack Horowitz. Those from Harris Corporation include J. Daniel Newman, Andrew P. Sacco, and Kenneth D. Fourspring. Those from the University of Rochester include Paul P. K. Lee, Judith L. Pipher, Craig W. McMurtry, Zeljko Ignjatovic, and Moeen Hassanalieragh. This work would not have been possible without their collaboration and help.

I have been very fortunate to have the guidance and support from my advisor, Zoran Ninkov, through my years at RIT. I am so thankful that everyone in the AST program helped make me feel welcome and supported. I especially would like to thank Jen Connelly and Cheryl Merrell for their unending support and invaluable help with anything that came up, especially when it was something difficult. A special thank you to Greg Fertig for training me to take over this project when I first arrived at RIT and Jack Horowitz for working with me and being someone to always be able to bounce ideas off of.

I've made many friends, too many to list, throughout my time at RIT but I would like to especially thank Yashashree Jadhav and Jesse Bublitz. They have always listened when I needed it and I always look forward to our weekly video chat ('Cat Chat') so we can talk

and I can share my love of Star Wars. Triana Almeyda, Brittany Vanderhoof, and Meaghann Stoelting helped me so much as well and I have always enjoyed our (usually long) conversations whenever we saw each other. Kevan Donlon and Kate Oram always made the lab such a welcoming place and I always knew I could ask them for advice and support.

My undergraduate professors at Alfred University, in particular Dave Toot, Roger Loucks, and David DeGraff, gave me an invaluable knowledge base through their classes that I have used every day. I loved my time at Alfred and being at the observatory. I would also like to thank my long-time friend from high school, Aaron Jackson, for constantly listening to me when I needed it. I always make so many good memories whenever we are together. He has always encouraged me whenever I needed it.

I would like to thank my husband, Eric Shormann, for always sticking by me, supporting me, and helping me get through everything throughout the years. Especially through some of the hardest times of our lives with the tornado and the pandemic. It's been a unique and challenging few years, and I couldn't imagine being able to do it without him. I am so thankful to always have my sister, Jen, and my Mom to get through my entire life with and always being there for me. I'm so happy that we have our phones and can video chat so that we can talk all the time even though I'm in a different state. I would not be where I am today without my entire family who have supported me through my entire life and academic career. They've given me advice and help whenever I have needed it without question. I am so glad to have all of them in my life.

And lastly, a special thanks to my cats, Cassiopeia (Cassirole), Nova (Novaball), and Orion (the Booper), who have helped in the writing of this dissertation (occasionally laying on the keyboard to give their input). They all made wonderful office mates and they have truly enriched my life. They always know when I need them most.

None of this would have been possible without everyone's love and support. I am immensely grateful to have you all in my life.

Contents

List of Figures

List of Tables

Chapter 1

Introduction and Background

The terahertz (THz) and the sub-THz spectral band is a region of millimeter/submillimeter light on the electromagnetic spectrum between microwave and far infrared region, with wavelengths from 30 μm to 3000 μm (or 100 GHz to 10 THz). THz radiation has been utilized very little compared to other portions of the electromagnetic spectrum up until the past 20 years or so (Widicus Weaver, 2019; Rogalski, 2011; Lewis, 2019b). Historically both the remote sensing and astronomy communities have avoided the THz regime is because of the low atmospheric transmission. This resulted in the late development of basic research in the physics of technologies used in THz (Widicus Weaver, 2019; Rogalski, 2011; Sizov, 2018; Lewis, 2019b). This lack of research has led to the term the 'terahertz gap' in technology for THz sensing and generation (Redo-Sanchez and Zhang, 2008; Creidhe O'Sullivan, 2012; Lewis, 2019b). This gap and delayed development of research has resulted in a diminished capability of astronomical object detection from a THz standpoint and limited number of observations compared to other regions of the electromagnetic spectrum (Rogalski, 2011). This lack of data is quickly catching up with more investigation into sensing technologies Widicus Weaver (2019); Sizov (2018).

In their paper, "Terahertz Detectors And Focal Plane Arrays," Rogalski and Sizov determined that of all detectable photons that have been emitted since the beginning of the universe, ninety-eight percent fall in the THz and far-infrared regions (Rogalski, 2011). Many

of these photons derive from the Cosmic Microwave Background Radiation (CMBR), other significant emission comes from an abundance of excited molecules that have bright spectral emission features in the THz regime (Stacey, 2011).

THz sensing technology has a variety of applications in addition to astrophysical phenomena. For example, THz technology is utilized for security, medical, packaging, and manufacturing quality control. This work will discuss a few of these applications but focus primarily on the astrophysical applications. The various THz detector technologies currently available each have their own advantages and disadvantages. Low sensitivity levels and slow response times are some of the drawbacks of existing technologies, but these are quickly improving (Rogalski, 2011; Stacey, 2011; Lewis, 2019b). These drawbacks often result in sensor systems with small focal plane arrays and require scanning techniques to generate useful images.

THz radiation has characteristics similar to the adjoining spectral regimes of radio and infrared. Many materials—including cardboard, paper, some plastics, et cetera—are transparent to THz radiation. The ability to peer through objects like cardboard using THz imaging makes this spectral region ideal for applications such as packaging and security (Corcos et al., 2015). THz radiation is also non-ionizing, meaning it does not harm humans because the radiation does not ionize electrons from atoms resulting in harmful radiation-induced biological effects(Fertig, 2014). This energy is able to penetrate materials without carrying high enough energies to cause harm (Stacey, 2011; Zhu et al., 2009).

From an astrophysical perspective, THz photons that are emitted or absorbed are large (about 100-1000 μm) compared to typical interstellar dust grains (around 0.1 μm). (Lesser, 2019; Walker, 2016/2019; Rogalski, 2011). Due to the large photon size with respect to dust grains, extinction effects do not plague observations like that of other spectral regimes such as optical and ultraviolet light (Lesser, 2019; Walker, 2016/2019; Rogalski, 2011). A major drawback of THz radiation for some applications is its absorption by water (Lesser, 2019). THz frequencies are highly absorbed by water due to rotational transitions giving rise to many absorption line features (Rogalski, 2011; Fertig, 2014; Horowitz, 2017). By extension, the water vapor in the atmosphere also strongly absorbs THz (Yasuko and Takamasa, 2008; Sizov,

2018; Walker, 2016/2019). There are a few atmospheric windows that exist and allow for the transmission of some THz radiation through the atmosphere. For astrophysical applications, to maximize throughput through such windows, observations normally must be obtained at a high elevation location (i.e., on top of the Chajnantor Plateau in Chile where Atacama Large Millimeter/Submillimeter Array (ALMA) is located) (Walker, 2016/2019; Walker et al., 2008). Alternatively, instruments can be deployed on a plane or suborbital rocket above most of Earth's atmosphere, or launched into space (Walker et al., 2008).

In addition to atmospheric attenuation, the astronomical background in the THz regime can create more complexity. There is dust emission from the Milky Way galaxy, zodiacal emission, and the cosmic microwave background radiation (SAO, 2017; Rogalski, 2011). Realistically for a photometric instrument, NEPs must be below 10^{-18} W/Hz$^{1/2}$ (Rogalski, 2011; Swinyard and Wild, 2013) in order to be able to distinguish sources from the background.

1.1 Spectroscopy Basics

1.1.1 Continuous Spectra, Emission Lines, and Absorption Lines

Gustav Kirchhoff and Robert Bunsen established the foundations of spectroscopy as we know it today (Carroll and Ostlie, 2007). They designed a device to look at a spectrum by passing light of a heated element through a prism (Carroll and Ostlie, 2007). They found that there was a specific pattern of dark and bright lines for each element (Carroll and Ostlie, 2007). Each pattern of emission (bright) and absorption (dark) lines were always at the same wavelengths for the same element (Carroll and Ostlie, 2007). This paved the way for identifying different elements based on it's spectrum.

Kirchhoff developed three laws to describe the patterns, now known as Kirchhoff's laws (Carroll and Ostlie, 2007):

1. A *continuous spectrum* where there are no dark lines is produced from hot, dense gas or hot solid (Carroll and Ostlie, 2007).

2. *Emission lines*, or bright spectral lines, are produced from hot but diffuse gas (Carroll

and Ostlie, 2007).

3. *Absorption lines*, or dark spectral lines within a continuous spectrum, are produced from cool and diffuse gas in front of a source with a continuous spectrum (Carroll and Ostlie, 2007).

These laws were quickly applied to looking at the spectra of our Sun and other stars resulting in learning the composition of elements that make up the stars.

Any object emits all wavelengths of light (with varying intensities). A continuous spectrum, in the first law, occurs when there is a blackbody of a specific temperature (Carroll and Ostlie, 2007; Walker, 2016/2019). A blackbody is an ideal emitter where it absorbs all light and re-emits it. A blackbody of a specific temperature emits a continuous spectrum where there is some energy at all wavelengths and has a peak energy at a specific wavelength corresponding with that temperature (Carroll and Ostlie, 2007; Walker, 2016/2019). This relationship of energy versus wavelength for a given temperature is given through Planck's law (Carroll and Ostlie, 2007; Walker, 2016/2019) which will be discussed more later on in this chapter.

The underlying processes that result in emission and absorption lines rely on a few other principles of physics. One piece to understanding this is the Compton effect, which treats light like a massless particle called a photon, instead of a wave (Carroll and Ostlie, 2007). Arthur Holly Compton was able to measure a change in wavelength of X-ray photons when they were scattered by free electrons (Carroll and Ostlie, 2007). By treating the light as a photon, Compton considered it a collision between a photon and a free electron which is initially at rest (Figure 1.1) (Carroll and Ostlie, 2007). Initially the photon starts with one wavelength, but the photon then collides with the electron. The collision both momentum and energy are conserved (Carroll and Ostlie, 2007).

In addition to the Compton effect, the Bohr model of atoms helps us understand the basic process for these emission and absorption lines. Prior to the Bohr model of atoms, atoms were looked at as a nucleus of protons and neutrons with electrons orbiting all around the nucleus like planetary bodies (of Encyclopaedia Britannica, 2020). Bohr changed this view to restrict electron orbits to specific, discrete radii (Figure 1.2) with specific energies

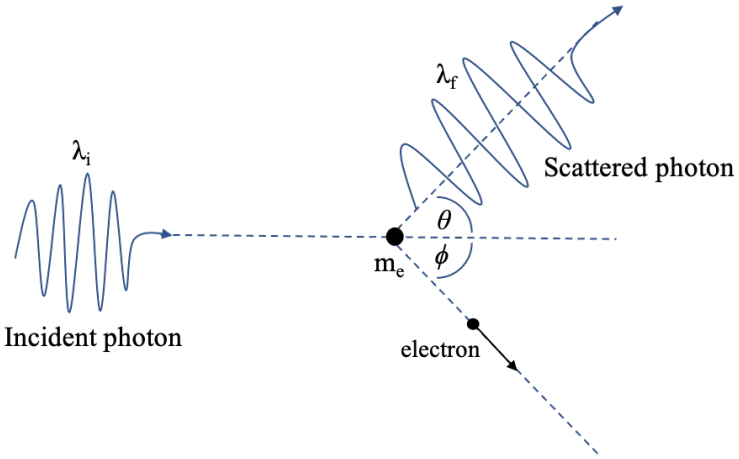

Figure 1.1: Illustration of the Compton Effect. The scattering angles of the photon and electron are θ and ϕ respectively (Carroll and Ostlie, 2007).

(of Encyclopaedia Britannica, 2020; Carroll and Ostlie, 2007). Each discrete radius, called the Bohr radius (equation 1.1.1), had it's associated 'allowed energy' (equation 1.1.2 for hydrogen) for a Bohr atom (Carroll and Ostlie, 2007).

$$r_n = \frac{4\pi\epsilon_0\hbar^2}{\mu e^2}n^2 = a_0 n^2 \tag{1.1.1}$$

$$E_n = -\frac{\mu e^4}{32\pi^2\epsilon_0^2\hbar^2}\frac{1}{n^2} = -13.6 \text{ eV}\frac{1}{n^2} \tag{1.1.2}$$

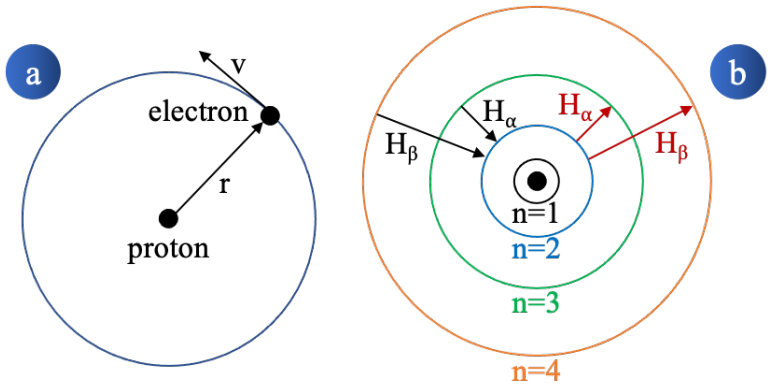

Figure 1.2: (a) Illustration of the Bohr model of a hydrogen atom. (b) Example of Balmer emission lines (black) and absorption lines (red) in a hydrogen atom (Carroll and Ostlie, 2007).

Bohr theorized that light is emitted because a photon 'carries away' the energy that is lost

when an electron transitions to a lower orbit (Carroll and Ostlie, 2007; of Encyclopaedia Britannica, 2020). With this understanding, we can understand what processes are occurring for the emission lines and absorption lines in Kirchoff's laws. A hot, diffuse gas will glow at specific wavelengths and these wavelengths occur when an electron 'falls' from a higher orbit to a lower orbit (figure 1.2b). The energy lost from the electron is emitted into the photon at the wavelength at that energy ($E_{photon} = \frac{hc}{\lambda}$) causing the emission lines (Carroll and Ostlie, 2007). Absorption lines occur when there is a cool, diffuse gas in front of a source with a continuous spectrum. Photons from the continuous spectrum that have the right energy can push electrons in the gas in front to higher orbits by the electrons absorbing that energy Carroll and Ostlie (2007). This absorption produces the dark lines in spectra.

1.1.2 Angular Momentum and Rotational Spectroscopy

Later on, quantum mechanics developed new ways of describing atoms. In a single electron atom (hydrogen) there are multiple sources of angular momentum (Tennyson, 2005). These are electron orbital angular momentum (referred to as l), electron spin angular momentum (s), and nuclear spin angular momentum (i) (Tennyson, 2005). A change in angular momentum also results in specific spectral features. For atoms with more than one electron, these values must be taken into account for each electron (Tennyson, 2005). Total angular momentum must be conserved making it important to account for each angular momenta quantity into one quantity that is conserved (Tennyson, 2005). Typically the orbital angular and electron spin momentum terms are combined into one quantity (vectorially adding) called total electron angular momentum, j (Tennyson, 2005).

$$\vec{j} = \vec{l} + \vec{s} \tag{1.1.3}$$

The nuclear spin and total electron angular momentum are then also added vectorially into one final angular momentum, f (Tennyson, 2005).

$$\vec{f} = \vec{j} + \vec{i} \tag{1.1.4}$$

1.1.3 Fine and Hyperfine Structure

Electron orbital angular momentum and electron spin are coupled together due to the relativistic or magnetic effects from quantum mechanics (Tennyson, 2005). 'Fine structure' in energy levels are due to the total electron angular momentum being split between combinations of both l and s for the same principal quantum number, n (Tennyson, 2005). In other words, the principal energy states are split up into various states depending on what the values of l and s are. Adapted from Tennyson (2005), table 1.1 gives a brief example of the fine structure splitting of nl orbitals in a hydrogen atom. l is given letter designations s, p, d, et cetera from spectroscopic notations which can be found in Tennyson (2005). The fine structure splitting is very small for hydrogen but the fine structure is much more important for more complex, multi-electron atoms (Tennyson, 2005).

Including nuclear spin further splits energy levels creating the 'hyperfine structure' for atoms (Tennyson, 2005). In hydrogen the nuclear spin is $i = \frac{1}{2}$ giving a final angular momentum for hydrogen of $f = j \pm \frac{1}{2}$ (Tennyson, 2005). The 21 cm (1420.406 MHz) line which is used to trace hydrogen atom densities throughout the interstellar medium (ISM) is caused by magnetic effects splitting between $f = 0$ or 1 (Tennyson, 2005).

***nl* Configuration**	***l***	***s***	***j***	**H atom**	**Level**
ns	0	$\frac{1}{2}$	$\frac{1}{2}$	$ns_{\frac{1}{2}}$	$n^2S_{\frac{1}{2}}$
np	1	$\frac{1}{2}$	$\frac{1}{2}$,$\frac{3}{2}$	$np_{\frac{1}{2}}$,$np_{\frac{3}{2}}$	$n^2P^o_{\frac{1}{2}}$,$n^2P^o_{\frac{3}{2}}$
nd	2	$\frac{1}{2}$	$\frac{3}{2}$,$\frac{5}{2}$	$nd_{\frac{3}{2}}$,$nd_{\frac{5}{2}}$	$n^2D_{\frac{3}{2}}$, $n^2D_{\frac{5}{2}}$
nf	3	$\frac{1}{2}$	$\frac{5}{2}$,$\frac{7}{2}$	$nf_{\frac{5}{2}}$,$nf_{\frac{7}{2}}$	$n^2F^o_{\frac{5}{2}}$, $n^2F^o_{\frac{7}{2}}$

Table 1.1: Example of Hydrogen atom fine structure levels. Adapted from Tennyson (2005).

1.2 Astrophysical Applications

1.2.1 Astrophysical Terahertz Targets

This section will comprise of a discussion of the wealth of different types of astrophysical phenomena that emit in the THz regime. Exploring these phenomena in multiple different

regimes of light can present valuable information into the deeper processes at work that looking into only one regime cannot give. THz traces cooling dust which occurs in a variety of processes from protoplanetary disks to the cooling of the universe in the cosmic microwave background radiation.

1.2.2 Interstellar Medium (ISM)

As discussed in section 1.1.3, the 21 cm line is used to trace the ISM. The ISM is the gas and dust existing in the regions between stars (Carroll and Ostlie, 2007). The ISM is critical in the cyclical evolution of stars (Carroll and Ostlie, 2007). Stars are 'born' or created with the dust and gas of the ISM Carroll and Ostlie (2007). When stars 'die,' much of the contents of the star is then returned to the ISM from stellar winds or explosions, which in turn feeds into new future stars (Carroll and Ostlie, 2007). Hydrogen, in many forms such as neutral hydrogen (HI), ionized hydrogen (HII), and molecular hydrogen (H_2), is the main component of the ISM making up about 70% (Carroll and Ostlie, 2007). Helium makes up most of the remaining materials in the ISM with metals (more complex molecules than hydrogen or helium) comprising only a few percent (Carroll and Ostlie, 2007). The 21 cm line traces neutral hydrogen in the ISM and occurs when the spin of the electron flips (Carroll and Ostlie, 2007). When the electron spin is aligned with the spin of the proton, the atom has slightly more energy (Carroll and Ostlie, 2007). The transition from anti-aligned to aligned means the atom gained a small amount of energy by absorbing a photon (Carroll and Ostlie, 2007). If the electron spin flips from aligned to anti-aligned, the atom loses energy and emits a photon (Carroll and Ostlie, 2007). Temperature of diffuse HI clouds can be calculated by studying the 21 cm line and the presence of this implies temperatures of 30 to 80 K (Carroll and Ostlie, 2007). The 21 cm line is extremely valuable in determining structure and kinematics in galaxies as well (Carroll and Ostlie, 2007).

Other molecules can be used to calculate different quantities to probe and study the ISM. Many of these can be found as bright lines in the THz regime (Carroll and Ostlie, 2007; Walker, 2016/2019). Table 1.2 lists a few bright spectral lines that are used to probe the ISM (Carroll

and Ostlie, 2007; Walker, 2016/2019).

Species	⇒ Line	Transition	Frequency (THz)	Wavelength (μm)
O^0	⇒ [OI]	$^3P_1 \rightarrow ^3P_2$	4.745	63.18
		$^3P_0 \rightarrow ^3P_1$	2.060	145.53
O^{++}	⇒ [OIII]	$^3P_2 \rightarrow ^3P_1$	5.786	51.82
		$^3P_1 \rightarrow ^3P_0$	3.393	88.36
C^+	⇒ [CII]	$^2P_{3/2} \rightarrow ^2P_{1/2}$	1.901	157.74
N^+	⇒ [NII]	$^3P_2 \rightarrow ^3P_1$	2.459	121.90
		$^3P_1 \rightarrow ^3P_0$	1.461	205.18
N^{++}	⇒ [NIII]	$^2P_{3/2} \rightarrow ^2P_{1/2}$	5.230	57.32
C^0	⇒ [CI]	$^3P_2 \rightarrow ^3P_1$	0.893	370.42
		$^3P_1 \rightarrow ^3P_0$	492.2	609.14
^{12}CO		$J = 3 \rightarrow 2$	0.3458	867.55
		$J = 4 \rightarrow 3$	0.4610	650.76
		$J = 6 \rightarrow 5$	0.6915	433.56
		$J = 7 \rightarrow 6$	0.8067	371.65

Table 1.2: Common bright THz lines. Adapted from Walker (2016/2019).

1.2.3 Protoplantary Disks

Young stellar objects (YSOs) with disks (protoplanetary disks) are abundant in species like HCO+ and CO. Relative abundances of molecular and atomic species within YSOs puts constraints and bounds on models and disk masses (Kevin France, 2014). Molecular hydrogen (H_2) is more abundant than HCO+ and CO, but without strong outflows, the ro-vibrational lines are difficult to characterize (Kevin France, 2014; Henning and Semenov, 2013). The spacing between energy levels is large because there are some forbidden transitions and have weak transitions (Kevin France, 2014). This makes H_2 difficult in the IR observations. Most of the mass contained within the disk have temperatures too low to emit in these ro-vibrational transitions (Henning and Semenov, 2013). The high-J rotational transitions (J is the rotational quantum number) of HCO+, CO, and other species emit bright emission lines in the THz region (SAO, 2017). The cool protoplanetary disks emit bright emission lines in abundance in the (sub)millimeter regime. For example, the data obtained from the protoplanetary disk of HL Tau taken in 2014 by the Atacama Large Millimeter/submillimeter Arrary (ALMA) resulted in continuum images at 2.9, 1.3, and 0.87 mm (103.4, 230.6, and 344.6 GHz) in Figure 2 of

ALMA Partnership (2015). Data led to first time being able to spatially resolve the morphology of the molecular disk creating channel maps of the HCO+(1-0) emission (ALMA Partnership, 2015). Different species of molecules like ^{13}CO not only distinguished where these species fall in the disk, but it is also indicative of planet formation in rings around the central star (SAO, 2017). Observing species such as [O I], CO, and H_2O are indication of outflows, jets, flows, and the shocks associated with these phenomena Farrah et al. (2019). There are some young protostars (ages of only 25000 years) that are only visible in the far-infrared (Farrah et al., 2019)

1.2.4 Galaxy Star Formation

Within a galaxy, there are regions and clouds of gas and dust that form stars by collapsing. For sustained collapsing of these clouds, they must also cool. As the clouds collapse to form young stars, they emit THz radiation (A.J. Barger, et al., 2008). Measuring the intensity of certain molecular lines, such as the bright CO cooling emission line, can give clues to the number of stars that are forming within a galaxy or nebulae (SAO, 2017; Stacey, 2011).

Star formation rates (SFRs) can have many implications for galaxies. Studying SFRs in different types of galaxies can point to clues of galactic merger histories (Stacey, 2011). About 70% of a class of galaxies, called ultra luminous infrared galaxies (ULIRGs), are believed to be powered by star formation and the rest by Active Galactic Nuclei (AGN) activity (Stacey, 2011). Using THz to map these SFRs in ULIRGs could help identify other characteristics and underlying reasons for the driving mechanism for both types of ULIRGs (Stacey, 2011).

1.2.5 Remote Sensing of Planetary Atmospheres

In remote sensing, visible light is used to track the top surface of clouds and radio/infrared is used to peer through the clouds to look at the planetary structures below (Yasuko and Takamasa, 2008). THz frequencies are able to partially observe through clouds with higher spatial resolution than radio and infrared because of the smaller wavelengths (Yasuko and Takamasa, 2008). These frequencies let scientists look at abundances of different molecules to

help glimpse some of the internal microphysical processes of clouds on both Earth and other planets without the light being scattered (Yasuko and Takamasa, 2008; Fertig, 2014).

For terrestrial applications, there are significant water and water vapor absorption lines in the THz regime (Fertig, 2014; Lis, 2007). Monitoring these lines could provide insight into water in the atmosphere. Over 50% of the long-wavelength radiation from Earth is in the THz region and, as such, is a crucial region to explore (Yasuko and Takamasa, 2008). Since water vapor is a large contributor to the greenhouse effect, monitoring it on a planet-wide scale using THz remote sensing could provide valuable information to understand the physics of Earth's atmosphere.

1.2.5.1 Mars

Infrared spectroscopy techniques have been utilized to measure the abundance of water vapor in the Martian atmosphere to understand the role it has had in Martian history (Gurwell et al., 2000). Understanding the vertical structure of water in atmosphere is key to understanding the Martian climate (Gurwell et al., 2000). The photochemistry of the atmosphere is directly dependent on abundances of water vapor and the water vapor altitude depends on the temperature distribution (Gurwell et al., 2000). Observing the variations that occur annually on Mars is key to unraveling the climate history on Mars (Gurwell et al., 2000).

The infrared methods being used to detect the water vapor abundances are unable to measure the distribution of water throughout the altitudes of Mars' atmosphere (Stacey, 2011; Gurwell et al., 2000). In order to understand the chemistry of Mars' atmosphere, a direct measurement of the distribution of water vapor is necessary (Gurwell et al., 2000). This can be achieved through THz spectral observations of resolved pressure-broadened lines (Gurwell et al., 2000; Stacey, 2011). Another easy measurement to make is observation of the species CO in the atmosphere to determine the distribution and the variation of temperature (Gurwell et al., 2000; Stacey, 2011).

1.2.5.2 Venus

The atmosphere of Venus also comprises mainly of CO which has strong spectral features in the THz regime. Measuring the CO in the atmosphere give unique temperature profiles and column densities. (de Pater, 1991)

Based on data obtained using the Nobeyama Millimeter Array, mapping of the ^{12}CO (J=1-0 at 0.115 THz) in the atmosphere traced this gas to altitude of about 70 to 100 km (the mesosphere) (Sagawa, 2008). Through the data taken in 2004 through 2006, extreme variations of wind patterns and circulation exist for the mesosphere. This radiation is currently the only remote sensing method to observe altitude differences from the bottom of the cloud layer to the top of the atmosphere for Venus (Sagawa, 2008). Some 0.103 THz measurements were able to get measurements from altitudes of 50 km (the bottom of the cloud layers). These measurements of the 0.103 THz continuum map showed higher inhomogeneity than expected (Sagawa, 2008). Understanding the molecular makeup and vertical distribution in the middle to high atmosphere is important to understanding the weather on Venus now and in its past.

1.2.5.3 Titan and Enceladus

Titan, one of Saturn's moons, is the second largest moon in our solar system and even larger than the planet Mercury. It is the only moon that has a considerable atmosphere (E. Lellough, 2010). The atmosphere consists mostly of Nitrogen like Earth's atmosphere, but has a surface pressure of 1.5 times that on Earth (Hörst, 2017). It's the only other solar system body with stable liquid on the surface in the form of methane and ethane lakes. Titan also has a subsurface water ocean (Hörst, 2017). This combination of the surface organics and unique atmosphere makes Titan an important object to study in the search for life and the conditions for biological life (Hörst, 2017).

The Cassini-Huygens mission provided a wealth of new information about Titan and it's atmosphere. It was found to be much more complex than every theorized previously (Hörst, 2017; E. Lellough, 2010). The Cassini spacecraft was primarily studying Saturn and only deviated to study moons for certain experiments making global coverage of Titan impossible.

Cassini has studied the lower atmosphere (stratosphere, 40-300 km and lower mesosphere, 300-500 km) using the composite infrared spectrometer (CIRS) revealing a complex and changing system with wind, temperature, and distribution of haze and minor species all interacting together (E. Lellough, 2010). The upper mesosphere and lower thermosphere (500 to 900 km) has only been sampled once by the Huygens decent probe and in the UV and near-IR by the UVIS and VIMS instruments onboard the Cassini spacecraft (E. Lellough, 2010). In order to more fully understand the atmospheric interactions in Titan's atmosphere, this region of the atmosphere must be studied in greater detail (E. Lellough, 2010).

Understanding the vertical distribution of different molecular species is where THz spectroscopy could be beneficial. Some ground-based measurements have been made and obtained a few measurements of wind speeds and isotopic ratios of different species but the measurements all have low spatial resolution (E. Lellough, 2010). E. Lellough (2010) modeled the Titan atmospheric spectrum in their figure 3. The continuum at 0.5 THz in the model appears to have a temperature of 60 K but there is a high density of emission lines in the spectrum and the emission lines give a temperature of approximately 150 K (E. Lellough, 2010).

E. Lellough (2010) also suggested a science mission for another of Saturn's moons, Enceladus. Enceladus is an icy body which has active plumes of water shooting out into space. The plumes are the result of cryovolcano activity. In addition to the cryovolcano, there is evidence for a subsurface ocean of water (E. Lellough, 2010). Observing the species contained within the plumes could give hints to the interior of Enceladus. With many species detectable in the THz regime, observing the plume-makeup over time could prove interesting.

1.2.6 Requirements for a Mission

An extremely sensitive device is needed to distinguish a very faint object in the THz regime from the CMBR (Sizov, 2018; Rogalski, 2011; Farrah et al., 2019). The primary continuum backgrounds in the IR are the CMBR, Cosmic Infrared Background, Galactic ISM emission and Zodiacal emission from interplanetary dust (Farrah et al., 2019). This makes each measurement only a relative measurement between the background and target and making absolute

measurements extremely difficult (Farrah et al., 2019; Birkinshaw, 1999). The CMBR peaks at 0.16 THz which is near the 'area of interest' in terms of frequency for these devices at 0.2 THz (Figure 1.3) (Birkinshaw, 1999). Doing an all-sky survey type mission to detect faint THz objects like galaxies or far away protoplanetary disks will require extremely sensitive devices to meet the sensitivity requirements to meet the levels of photon background and detect a small signal. The required NEP limits necessary for both photometry and spectroscopy are shown in multiple figures such as figure 1 in Goldsmith et al. (2007) or figure 8 in Farrah et al. (2019) which was based on the Goldsmith (2007) figure. As this chapter details the device characterization, these devices will not replace the current TES or MKIDs devices used for this type of mission and should not be developed in hopes of a dark all-sky survey application. Despite the CMBR, these devices will be useful for a different type of astrophysical mission: planetary remote sensing. The signals from planets while in orbit will be much larger and easier to distinguish than attempting to detect a faint object. The requirements for a detector for this mission will be detailed in the next section.

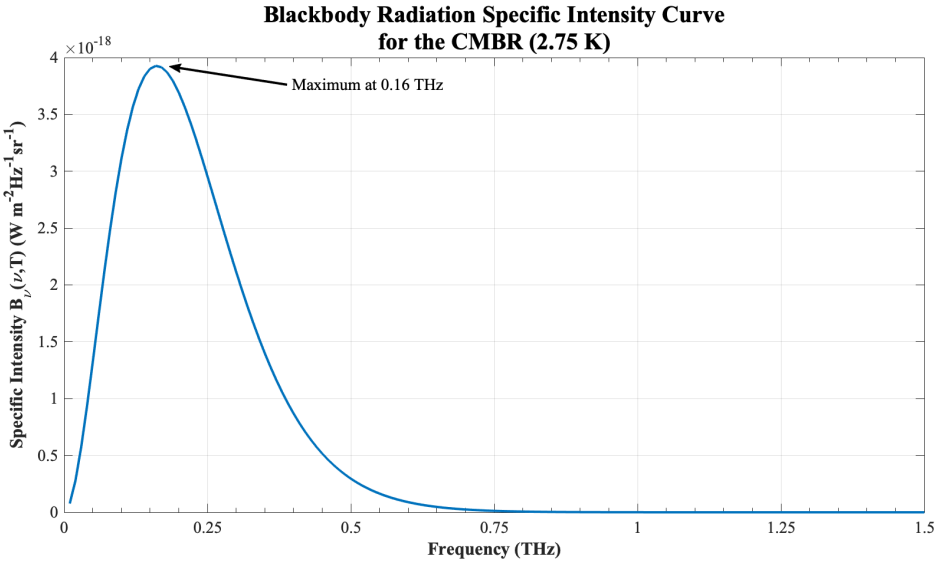

Figure 1.3: Blackbody radiation specific intensity curve for the CMBR at 2.75 K.

Many of the sources are reported in brightness temperature as shown in table 1.3. The brightness temperature is the temperature that a blackbody radiator would need to be at in order to give off the same specific intensity as the observed object. These numbers will need

Planet	Wavelength (μm)	Frequency (GHz)	Brightness Temperature (K)
Venus	750	400	323 ± 41
	450	668	277 ± 24
Jupiter	1744	172	169 ± 2
	1332	227	170.9 ± 3.9
	1049	286	166 ± 2
	890	337	174.3 ± 5.1
	750	400	162 ± 18
Saturn	1744	172	141 ± 3
	1049	286	126 ± 2
	609	492	112 ± 2
Uranus	1498-999	200-300	92
	750	400	94 ± 16
Neptune	1498-999	200-300	86.2
	750	400	117 ± 24

Table 1.3: Brightness Temperatures of planets adapted from (Walker, 2016/2019)

to be converted to a power that would be received by the detector in order to determine if these FETs would be able to detect a source. This section will outline these calculations.

As discussed in section 1.1.1, produces varying energy at all wavelengths with a peak wavelength related to the temperature. A blackbody radiator relates to temperature through Planck's Law,

$$B_\lambda(\lambda, T) = \frac{2hc^2}{\lambda^5} \frac{1}{exp(hc/\lambda kT) - 1}, \tag{1.2.5}$$

in units of $Wm^{-2}m^{-1}sr^{-1}$ where h is Planck's constant, c is the speed of light, lambda is the wavelength, k is Boltzmann's constant, and T is the temperature.

Similar to the measurements compiled in table 1.3, if the detector was located on Earth these planets could be treated as a point source and the power falling on the detector on Earth is straightforward. As an example, Jupiter was measured as 170.9 ± 3.9 K at 227 GHz (1.332 mm). Utilizing equation 1.2.5, we get a spectral radiance, B_λ, of $0.44Wm^{-2}Hz^{-1}sr^{-1}$. To convert this to the power falling on the detector, we need to calculate the solid angle, surface area of Jupiter, and the bandwidth of the detector. The solid angle here is calculated:

$$\Omega = \frac{A_{detector}}{4\pi r^2_{Earth-Jupiter}} = 2.5 \times 10^{-26} sr. \tag{1.2.6}$$

The surface area of Jupiter is $4\pi r^2 = 6.14 \times 10^{16} m^2$ and the frequency bandwidth of our detector is about 15 GHz or about 28 mm in wavelength. To get the approximate power at the detector, we take $B_\lambda \times \Omega \times SA_{Jupiter} \times \Delta\lambda = 1.89 \times 10^{-11} W$. The NEP of the detector in watts will have to be smaller than this number in order for it to be detected on Earth.

If we instead calculate this for a satellite in orbit around Jupiter, this calculation will change since we can no longer treat Jupiter as a point source. We can calculate it in the following way:

$$E(\lambda) = \int_{discJupiter} B_\lambda cos\alpha d\Omega \tag{1.2.7}$$

where

$$d\Omega = \frac{dA_{proj}}{r_{d-J}^2} = \frac{r_{Jup}^2 sin\theta cos\theta d\theta d\varphi}{r_{d-J}^2} \tag{1.2.8}$$

$$\implies E(\lambda) = \int_{\varphi=0}^{2\pi} d\varphi \int_{\theta=0}^{\frac{\pi}{2}} \frac{r_{Jup}^2}{r_{d-J}^2} B_\lambda sin\theta cos\theta d\theta = 42 \times 10^3 \tag{1.2.9}$$

The result from this then needs to be multiplied by the bandwidth and area of the detector to get 1.3 μW falling on the detector if it was in orbit at a distance of 4200 km assuming no optics and just a single detector.

1.3 Terrestrial Detector Applications

1.3.1 Packaging and Quality Control

Commercial assembly lines are in need of a quick way to look for defects and monitor the quality of the products being manufactured (Fertig, 2014). With a THz imager, it would be possible to look at a component and scan for defects in materials. Using this technology, one could image for quality control purposes and see if there is any damage on millimeter/submillimeter scales (Fertig, 2014). When shipping fragile items, many shipping and packaging companies would like to be able to look through the box and check the condition of the contents without opening the box for fragile contents. Quality control could potentially be greatly improved with non-contact rapid THz imaging (Fertig, 2014).

1.3.2 Security

THz imaging has many security applications in a variety of situations (Fertig, 2014; Sherry, 2013; Zhu et al., 2009). Since clothes are transparent but metals are opaque to THz, a small camera system could be designed to be worn by police officers that could image people and search for concealed weapons, providing early warning in potentially dangerous situations (Fertig, 2014; Zhu et al., 2009). Additionally, at large sporting events, spectators typically must pass through a metal detector to gain entry. A system could be deployed where people could just walk through a hallway illuminated with THz and a camera could image the people as they walked through to search for weapons (Horowitz, 2017). This system could potentially decrease waiting times significantly at large crowd events. This same concept can be extended to airport security (Horowitz, 2017). Current airport scanners use millimeter waves to search for hidden weapons, but by switching to a THz (submillimeter) scanner to search would give the Travel Security Agency (TSA) better spatial resolution to scan specific areas if a dangerous item has been detected (Fertig, 2014; Horowitz, 2017). This is due to the Rayleigh criterion stating that minimum resolvable element is proportional to the wavelength (Fertig, 2014). Since many chemicals have spectral features in the THz, it can also be used to screen for dangerous chemicals that can be identified at airport security and sporting events.

1.3.3 Medical

Since many materials are transparent to THz radiation including some human tissues (like the outer layers of teeth and small layers of skin), it's conceivable that THz imaging could be used as an alternative to X-ray imaging in certain cases (Zhu et al., 2009). The human body is made mostly of water which absorbs THz radiation quickly, but in certain places like teeth, hands, and feet, it would be possible to see through the skin to the bones which are denser and are opaque to THz (Wallace et al., 2005; Pickwell-MacPherson and Wallace, 2009). A person can only have a certain number of X-ray images taken because ionizing X-rays, which in large quantities are harmful to the human body (KARAGOZ et al., 2015). As stated before, THz is non-ionizing, or not harmful to humans, so THz imaging could mitigate some of the deleterious

cumulative effects of X-ray images (Fertig, 2014; Wallace et al., 2005; Pickwell-MacPherson and Wallace, 2009).

Many chemicals have emission, absorption lines, and other spectral characteristics within the THz region. This could be applied to imaging a vein or skin in the hand and monitor changes in those corresponding spectral characteristics to determine certain chemical abundances (Cherkasova et al., 2016). This method could extend to monitoring specific THz spectral changes that correspond with glucose levels in the blood, which could make it so that people with diabetes would just image through their hands non-invasively as opposed to having to draw blood to test for glucose levels (Kai-Eric Peiponen and Kuwata-Gonokami, 2013; Sherry, 2013; Zhu et al., 2009; Cherkasova et al., 2016).

1.4 A Few Current Detector Technologies

1.4.1 Bolometers/Microbolometers

Bolometers are made of a resistive material that has a high thermal conductivity and a small thermal capacity (Richards, 1994; Lewis, 2019a; Fertig, 2014; Horowitz and Winfield, 1980; Rogalski, 2011). The radiation incident on the detector deposits energy, resulting in a change in temperature and thus resistance within the material (Richards, 1994). The basic operation of this can be seen in Figure 1.4. This detection does not involve a photon interacting with an electron directly. Bolometers' response times can be slow, however, because of the time it can take the detector to cool down (Fertig, 2014). This often limits bolometers to single element detectors or small arrays requiring scanning techniques to produce an image and take data. There are larger arrays of bolometers now, however they require complex multiplexing systems to read out (Richards, 1994; Rogalski, 2011; Siegel, 2002; Woodcraft, 2009).

1.4.2 Transition Edge Sensors (TES)

TES is essentially a bolometer made from a superconducting film that is cooled to a constant temperature at which the film transitions between normal metal and superconductor. At this

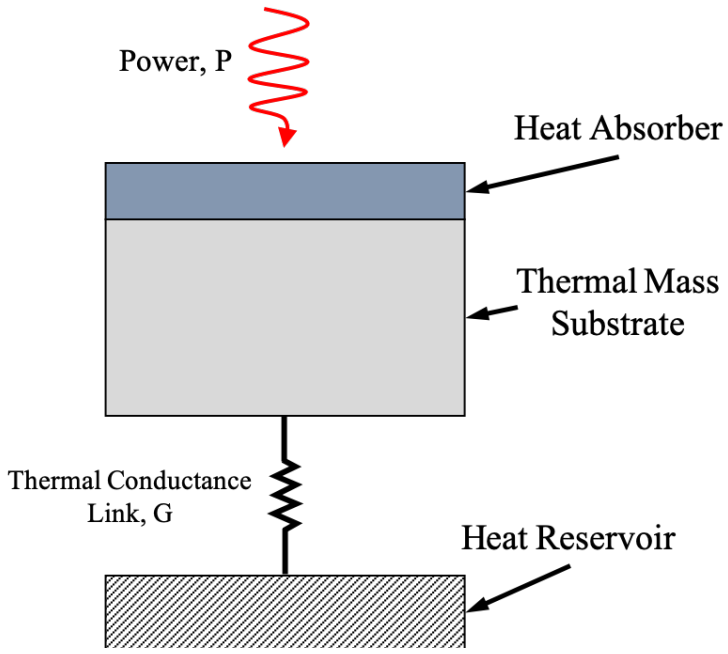

Figure 1.4: Illustration of how a basic bolometer works.

temperature (typically less than 10 K), the film is highly sensitive to changes in temperature due to incoming radiation (Woodcraft, 2009). This temperature change causes a large resistance change. An immediate drawback of this technique is the need for extremely low cryogenic temperatures. TES often also have significant dark current noise (current inherent within the detector in the absence of a signal) (Woodcraft, 2009). Superconducting quantum interference devices (SQUIDs) are also necessary to amplify the signal from a TES. A SQUID is an extremely sensitive magnetometer using superconducting materials (Carlstrom et al., 2011). The current measured by the TES is fed into an inductor in order to direct magnetic flux to the SQUID. The SQUID, run at cryogenic temperatures, must be shielded from stray magnetic flux that it is very sensitive to. The signal is then run to room temperature readout electronics (Lewis, 2019a; Carlstrom et al., 2011; Sizov, 2018). These leads on the device must be short to avoid signal dissipation as discussed in Carlstrom et al. (2011). This limits the mechanical design of the detectors. In addition to limited mechanical design, the TES devices have a high cost due to expensive materials that are used. The 10 meter South Pole Telescope (SPT), Submillimetre Common-User Bolometer Array 2 (SCUBA-2) (A.J. Barger,

et al., 2008), and Atacama Cosmology Telescope utilize TES technology (Bock, 2008; Benford et al., 2000; Siegel, 2007, 2002).

1.4.3 Kinetic Inductance Detectors (KIDs)

Kinetic inductance is charge carrier inertia causing inductance within a material. KIDs take advantage of this in a superconductor material. Superconductors have two charge carriers called Cooper pairs, current-carrying electron pairs without resistance, and quasiparticle excitations, with resistance (Szypryt, 2017; Mazin, 2004). When the superconductor material is cooled to low temperatures, the kinetic inductance of the Cooper pairs dominates. Using this to measure changes in temperature is possible because the effect is highly temperature dependent. When a photon with energy greater than two times the energy gap of the superconductor falls on the superconductor film, it breaks up Cooper pairs resulting in quasiparticle excitations (Baselmans, 2012; Mazin, 2004, 2009). The change in the quasiparticles changes the surface impedance which is mainly inductive. The superconducting film is part of a resonant circuit into a feedline which can be read at the resonance frequency Szypryt (2017). A simple representation of this can be seen in Figure 1.5 where the film is represented by a variable inductor. KIDs are very promising in that they can be implemented into large arrays without the drawbacks of other technologies described. The disadvantage here is that the detectors must be operated at extremely low cryogenic temperatures (Baselmans, 2012; Mazin, 2004, 2009). The Caltech Submillimeter Observatory has the instrument call Multiwavelength Submillimeter kinetic Inductance Camera (MUSIC) which uses KIDs with 576 pixels for four wavelengths (850, 1100, 1300, and 2000 μm) (Schlaerth et al., 2008; Maloney et al., 2010). There is also the AMKID instrument on the Atacama Pathfinder EXperiment (APEX) with 3520 pixels (347 GHz detection) and 21600 pixels (850 GHz detection) (Baselmans, 2012; Mazin, 2004, 2009).

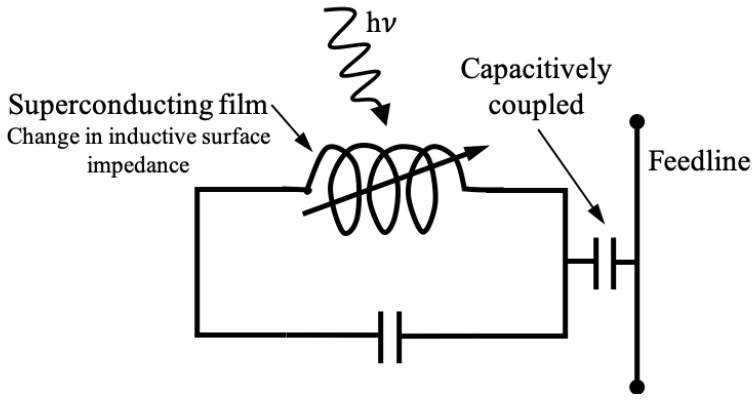

Figure 1.5: Illustration of the resonant circuit and feedline for an MKID. Based off of Mazin (2004).

1.4.4 SBDs and SIS Mixers

Schottky barrier diodes (SBDs) use a semiconductor and metal junction to create a diode. Whisker-contacted diodes are most often used for THz frequencies. Whiskers are extremely fragile driving up the cost of Schottky diodes (Rogalski, 2011). Superconducting-insulator-superconductor tunnel junction (SIS), also called a superconducting tunnel junction (STJ), uses two layers of semiconductors that are separated using the thin insulating layer. Current flows through the insulator through the quantum tunneling process (Rogalski, 2011; Schlaerth et al., 2008). SISs and SBDs use heterodyne technology, meaning detecting the radiation requires a technique called mixing. Mixing is where a lower frequency (LF) driven by a solid-state local oscillator (LO) is either added or subtracted with the received signal frequency (RF). High-powered sources are needed as the LF and, aside from free electron lasers, most THz sources are often limited to producing microwatts to milliwatts of power. This technique translates the signal to a lower frequency that electronics are more easily able to handle, avoiding losses in cabling, pickup from outside sources, et cetera (Rogalski, 2011). The major drawbacks to these detectors are: the cost, the detectors are fragile, the responsivities tend to be low, and they are more susceptible to noise. NASA's Submillimeter Wave Astronomy Satellite used Schottky diodes and ALMA uses SIS detectors (Rogalski, 2011; Siegel, 2002).

1.4.5 Pyroelectric and Golay Cells

A pyroelectric detector uses a crystalline material that changes the atoms' positions slightly when heated or cooled. This change in position affects the polarization of the material, resulting in a voltage across the crystal as illustrated in Figure 1.6. Detection requires that the THz radiation must be modulated or chopped (Byrd, 2008; Rogalski, 2011). Pyroelectric detectors are exceedingly susceptible to heat and light interference. The response of these detectors is also not well standardized and sensitivity can be limited. Pyroelectric detectors can be made to respond quickly, but sensitivity will drop proportionately with faster response times (Byrd, 2008; Rogalski, 2011; Siegel, 2002). Pyroelectric detectors are used in biomedical imaging, pollution detection, and gas analyzers (Byrd, 2008).

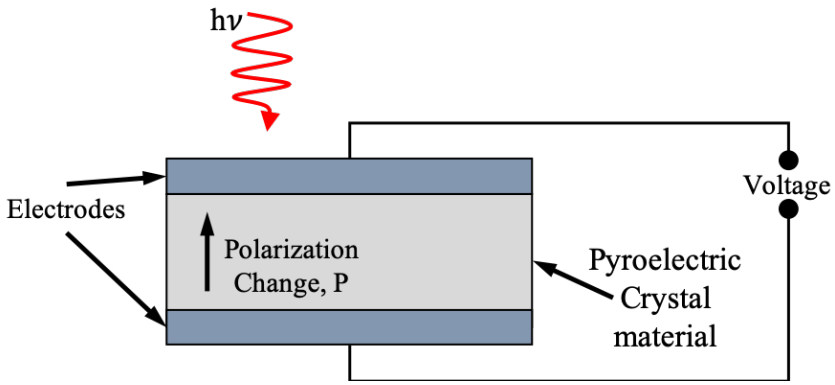

Figure 1.6: Illustration of a basic pyroelectric detector. Based off of Domke and Odon (2012).

Golay cells are a single-element detector that is made of a sealed chamber filled with gas (e.g., xenon gas) that, when exposed to radiation heats up and causes the gas and chamber to expand. The expansion deforms a membrane that is attached to a mirror. This mirror is exposed to a beam of light and the movement reflects light into a photodiode, producing a signal. This is illustrated in Figure 1.7. These devices are often expensive, very fragile, and extremely vulnerable to vibrational noise. The Golay cell is also incredibly slow to respond, on the order of 15 milliseconds (Rogalski, 2011). While Golay cells are rarely used for astrophysics anymore, they have been used in some smaller-scale telescope experiments like SOLAR-T presented in Pierre Kaufmann1 and Timofeevsky (2015).

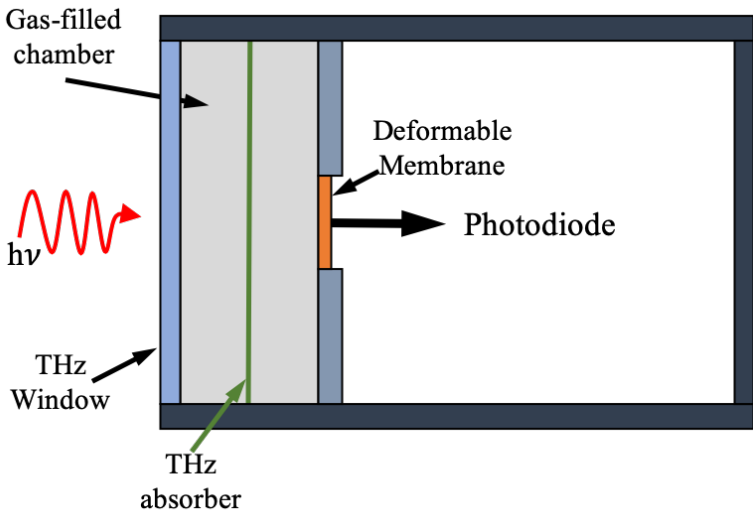

Figure 1.7: Illustration of a basic golay cell detector. Based off of Andreone et al. (2016).

1.4.6 Detector Comparisons

Noise equivalent power (NEP) is an important quantity when characterizing a detector. NEP is essentially the amount of power incident on the detector that is required to give an output signal that is equal to the noise, in other words, the amount of incident power to achieve a signal-to-noise ratio (SNR) of 1. NEP is expressed in the units Watts/$\sqrt{Hz}$) (the power required within a 1 Hz bandwidth). This can be written in terms of responsivity (detector signal over input power, $\frac{V}{P}$ or $\frac{I}{P}$) in this way:

$$NEP = \frac{N_V}{R_V} = \frac{N_I}{R_I} \tag{1.4.10}$$

where N is the noise density with subscript for volts (V) or amps (I) ($V/\sqrt{Hz}$ or $I/\sqrt{Hz}$) depending on detector output and R is responsivity with the same subscripts (V/W or I/W). Table 1.4 shows some of the major technologies explained above with some typical NEP values for uncooled single-element devices.

Some cooled detectors are able to reach much lower NEP and better sensitivity. Cooled bolometers and KIDs currently have some of the best NEPs up to 0.4x10^{-19} to 3x10^{-19} W/$\sqrt{Hz}$ for bolometers and on the order of 10^{-20} W/$\sqrt{Hz}$ (Fyhrie et al., 2018). Cooling the bolometers

Uncooled Single Element THz Detector Technology			
Technology	Detected Frequencies (THz)	Responsivity (kV/W)	NEP(pW/Hz$^{1/2}$)
Bolometer	0.2-30	—	0.1-10
Schottky Barrier Diode	0.4	211.00	1-20
Golay Cell	0.2-30	0.1-45	200-400
Pyroelectric Detector	0.1-30	150	400

Table 1.4: Comparisons of uncooled single element THz technologies. Adapted and modified from Table 11 in (Rogalski, 2011).

results in a long response time. The Cosmic Background Explorer (COBE) instrument Far-InfraRed Absolute Spectrophotometer (FIRAS) instrument used bolometers. Herschel Space Observatory also utilized bolometers in a 326-pixel array in its Spectral and Photometric Imaging Receiver (SPIRE). Bolometer (and most of these technologies) are implemented in small scale arrays only due to isolation and readout limitations (Rogalski, 2011). This makes the low NEPs extremely important. With larger focal plane arrays (FPA), a detector could gather a larger spot on the sky (Rogalski, 2011). Some current and past instruments with some technical specifications can be seen in table 1.5 .

Over the past 20 years, the far infrared (far-IR) observations have increased immensely due to the rapid expansion of sensing technologies. Prior to space- or air-borne observatories like Herschel, there were single-dish observatories were used to obtain the far-IR data (Widicus Weaver, 2019). Single-dish observatories leading the far-IR measurements included the National Radio Astronomy Observatory (NRAO) 12-m telescope, the Institut de Radioastronomie Millimétrique (IRAM) 30-m telescope, the now-decommissioned Caltech Submillimeter Observatory (CSO), the James Clerk Maxwell Telescope (JCMT), and the Atacama Pathfinder Experiment (APEX) Widicus Weaver (2019). While using the data to identify molecules, spectral line features could potentially be confused due to sources being inhomogeneous Widicus Weaver (2019). Spatial distribution maps of molecules were created by interferometric observations to address this. Interferometric observatories such as Plateau de Bure Interferometer (PdBI), Owen's Valley Radio Observatory (OVRO), the Smithsonian

Terahertz & Far-IR Astronomical Instruments						
Instrument	Observatory	Wavelength Ranges (μm)	NEP (W/$\sqrt{Hz}$)	Number of Elements	Detector Type	Status
SCUBA	JCMT	450/850	2×10^{-16}	5000/5000	TES	Decommissioned 2005
SCUBA2	JCMT	450/850	2×10^{-16}	91/36	Bolometer	Operational
ZEUS-2	CSO/APEX	200 to 600	4×10^{-17}	555	TES	Operational
A-MKID	APEX	350/850	1×10^{-15}	25000	KID	Operational
MAKO	CSO	350	7×10^{-16}	500	KID	Decommissioned 2015
Z-Spec	CSO	960 to 1500	3×10^{-18}	160	Bolometer	Decommissioned 2015
HAWC+	SOFIA	40 to 250	6.6×10^{-17}	2560	TES	Operational
HIRMES	SOFIA	25 to 122	2.2×10^{-17}	1024	TES	Cancelled 2020
SPIRE	Herschel	200 to 600	4×10^{-17}	326	Bolometer	Decommissioned 2013
PACS bol.	Herschel	60 to 210	2×10^{-16}	2560	Bolometer	Decommissioned 2013
PACS phot.	Herschel	50 to 220	5×10^{-18}	800	Photoconductors	Decommissioned 2013
NIKA2	IRAM	1250/2000	1.7×10^{-17}	4000/1000	KID	Operational
HFI	Planck	300 to 3600	1.8×10^{-17}	54	Bolometer	Decommissioned 2013

Table 1.5: A list of some of the instruments in the Terahertz and Far-IR regime along with their respective technical specifications (Farrah et al., 2019; Rogalski, 2011).

Millimeter Array (SMA), and the Combined Array for Millimeter/Submillimeter Astronomy (CARMA) mapped some molecular distributions. More recently ALMA has expanded the far-IR capabilities, able to observe with subarcsecond spatial resolution and observing spectral features with a broadband (Widicus Weaver, 2019). ALMA produces high-spatial resolution and high-sensitivity spectral data that allow for obtaining spectra at each spatial point and simultaneously producing images (Widicus Weaver, 2019).

1.5 Motivations for Further Technology Development

KIDs and some TES systems seem to be showing the most promise in developing larger arrays of devices and can achieve lower noise (Farrah et al., 2019). However, they are still more expensive to manufacture because of material costs. To make THz astronomy more accessible, detectors will need to be lower cost and smaller footprint devices in order to be launched for small-scale satellite missions (Fertig, 2014; Horowitz, 2017). It is important to develop THz technologies for space due to the fact that there is so much information to be gained in observing in the THz regime. Chapter 1.2.1 will discuss the importance of THz astronomy in detail. Finding a technology that is easily reproduced into a focal plane array and implemented into simple readout electronics to reduce total detector size will be key to making it easier to launch for missions. The purpose of this work is to determine whether or not Si-MOSFET devices would be suitable to fill this gap and what astrophysical science would be possible. It is unlikely for FETs to replace KIDs or TES devices, but determining if they are usable for smaller scale missions could make more small-scale THz astrophysical missions more of a reality.

Chapter 2

Si-MOSFETs

2.1 Anatomy of a MOSFET

The field effect transistor (FET) was proposed by Lilienfeld and Heil in 1930 but a working device was not created until 1948 by Shockley and Pearson. Years later, metal-oxide semiconductor FETs (MOSFETs) were created and have since been utilized in most every kind of integrated circuit in use today (Horowitz, 2017). In its simplest form, a MOSFET is a switch. Since MOSFETs are used in most electronics—digital and analog circuits—they are extremely cheap and easy to manufacture (Yavorskiy et al., 2012). Creating large arrays out of FETs are extremely cost effective and can be made relatively small and lightweight (Fertig, 2014; Horowitz, 2017). The technology is well understood and fairly standardized in manufacturing. MOSFETs take very little current to turn the switch to the on position compared to the traditional transistor switch (Fertig, 2014).

MOSFETs utilize the concept of PN junctions (Horowitz, 2017). The devices utilize one type of semiconductor as a substrate and then two regions of the opposite type created through ion implementation. A layer of SiO_2 is grown on top for insulation and a metal placed on top to form the gate terminal (Horowitz and Winfield, 1980). MOSFETs are devices with four terminals: Gate, Source, Drain, and Substrate. Often the substrate is tied to the source, making it a three-terminal device (Horowitz and Winfield, 1980). Figure 2.1 shows a simplified cross-section of a three-terminal MOSFET. There are two types of MOSFETs: NMOS and

PMOS. NMOS has a p-type semiconductor substrate and two conductive n-type semiconductor regions in the source and drain. PMOS are the opposite: n-type substrate and p-type source and drain regions (Horowitz and Winfield, 1980; Streetman and Banerjee, 2006; Sze and Ng, 2007; Ytterdal et al., 2003). For the purposes of this work, we will focus on NMOS devices because the devices being tested are NMOS.

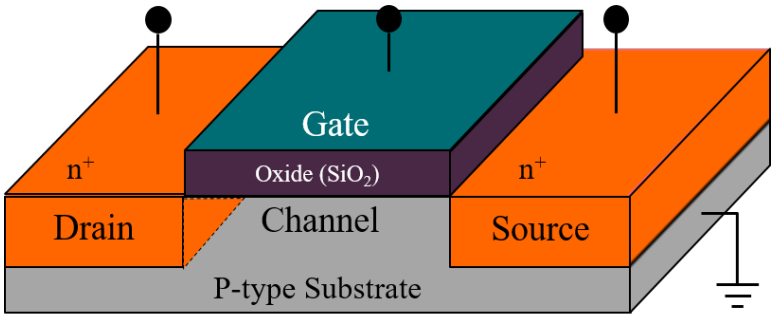

Figure 2.1: Illustration of a basic MOSFET (NMOS)

2.2 Gate Voltage Effects

There are many different types of operation of a MOSFET depending on how the device is run. A major factor in the operation of a FET is the gate voltage (Horowitz and Winfield, 1980; Pierret, 1990). The gate voltage controls the conduction of the channel. In an ideal FET, if there is no voltage placed on the gate, the device is in an equilibrium state and no electrons can flow from source to drain (or drain to source) (Pierret, 1990). In real-world devices there is always a small amount of conduction of electrons allowing some current to flow. This can be called the leakage current. When there is a voltage placed on the gate that is enough to establish a channel so that electrons can flow in the channel from source to drain (or drain to source), this voltage is known as the threshold voltage (Horowitz and Winfield, 1980; Pierret, 1990). The threshold voltage is also known as the turn on voltage. The threshold voltage will be explored further in section 2.3. The main regimes with respect to the gate operation are:

(1) **off** with no current flow;

(2) **subthreshold or weak inversion** with small currents due to diffusion only, this is also called the *cutoff region*; and

(3) **strong inversion** where current is able to flow through the channel.

In the following description, the FET is an NMOS device; for a PMOS device, the charges are the opposite. When there is no voltage on the gate, the FET is off and no current is flowing through the device (Pierret, 1990; Horowitz and Winfield, 1980). When the applied voltage on the gate is equal to or greater than the threshold voltage, the FET is on, and electrons can move in a channel underneath the gate resulting in current flow.

Figure 2.2 illustrates the progression of turning a FET on in order to understand how the channel is formed and current begins flowing (Pierret, 1990). When a voltage is applied to the gate that is less than the threshold voltage ($V_{GS} < V_T$), the channel, also called the inversion layer, is not completely formed, but some current is able to flow through the device through the process of diffusion (Pierret, 1990).

The positive voltage on the gate repulses the positive charges (holes) in the substrate creating a region depleted of the majority charge carrier. This region is called the depletion region (Pierret, 1988, 1990; Horowitz and Winfield, 1980). There are still negative charges (electrons) in the substrate underneath the gate. These particles start diffusing between the source and drain. This motion is caused by the particles spreading out due to random thermal motion (Pierret, 1988). The particles tend to wander to areas with low concentration of particles—the depletion region—from higher concentrations—like the source and drain (Pierret, 1988).

As the positive voltage on the gate is increased towards the threshold voltage, these electrons start to form a small layer beneath the gate at the substrate-oxide interface (Pierret, 1990). This surface appears to change character from p-type to n-type, or the majority carriers (holes) to minority carriers (electrons). This behavior is called inversion (Pierret, 1988, 1990). The inversion layer is the channel through which electrons are able to flow from the source to drain or drain to source.

When the inversion layer is fully formed, the device can be looked at like a parallel plate capacitor. The Si-Oxide (common material) is an insulator forming the capacitor with the gate

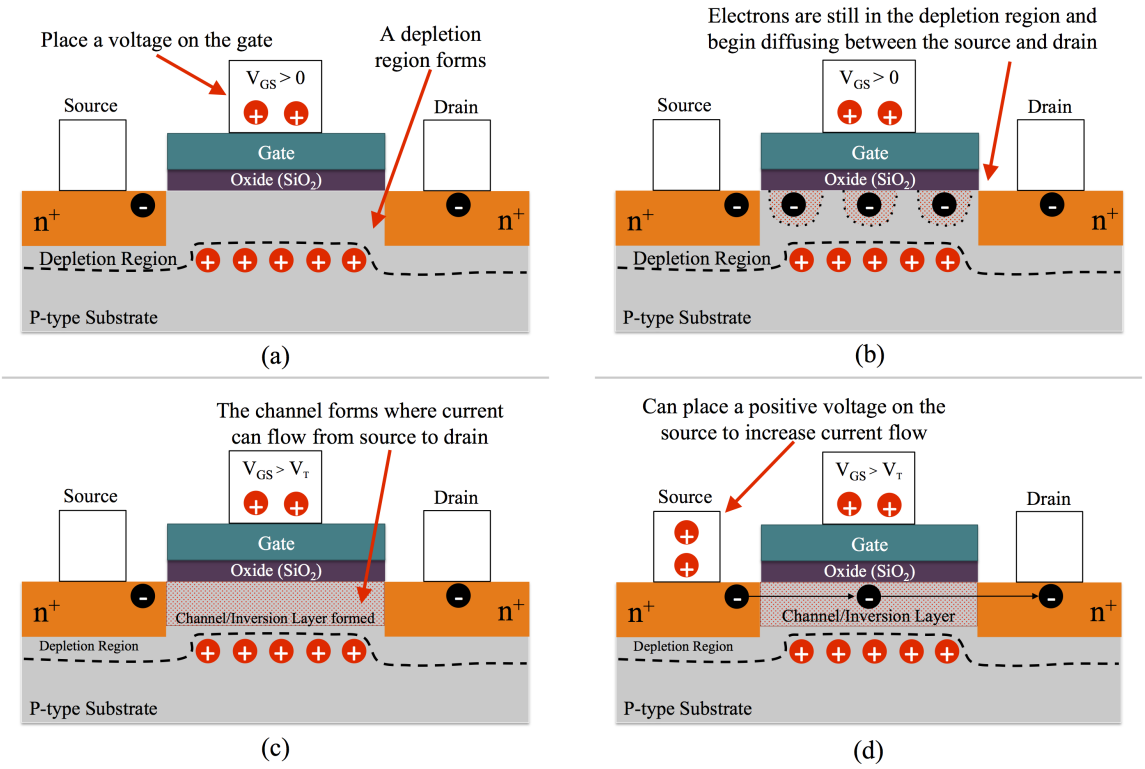

Figure 2.2: Illustration of the basic operation of a MOSFET (NMOS): (a) Depletion region is formed, (b) Electrons gather under the gate, (c) Inversion layer or channel is formed where electrons can move through easily, and (d) biasing the source (or drain) with a positive voltage increases the current flow.

as one plate and the area beneath the insulator, or the channel, as the other plate (Pierret, 1990; Horowitz and Winfield, 1980). Placing a positive voltage on the gate induces negative charges to go into the channel. This increases the conductivity of the channel (Fertig, 2014; Horowitz and Winfield, 1980).

2.3 Threshold Voltage and Subthreshold Regime

The threshold voltage is the gate voltage at which the charge density in the inversion layer is the same as the density of charge carriers in the substrate and the channel is fully formed (Neamen, 2000). Current can still trickle through the device in the subthreshold region, when the gate is almost closed, where the FET is in a partially on state (Horowitz and Winfield, 1980; Streetman and Banerjee, 2006; Sze and Ng, 2007).

This current is due mainly to diffusion. Diffusion is proportional to the carrier concentration gradients (∇p for holes and ∇n for electrons) in the device (Pierret, 1988):

$$\begin{aligned} I_N &= qD_N\nabla n \\ I_P &= qD_P\nabla p \end{aligned} \tag{2.3.1}$$

This current can be calculated as a function as gate voltage (VGS) as follows from (Sharroush et al., 2009; Streetman and Banerjee, 2006):

$$I_{sub} = \mu(C_d + C_{it})\frac{Z}{L}\left(\frac{kT}{q}\right)^2 \cdot \left(1 - exp\left[\frac{-qV_d}{kT}\right]\right) \cdot exp\left[\frac{q(V_{GS} - V_T)}{kTC}\right] \tag{2.3.2}$$

where

Variable	Definition
μ	Electron mobility
C	$C = 1 + \frac{C_d + C_{it}}{C_{ox}}$
C_d	Capacitance of the depletion region
C_{it}	Capacitance of fast interface states
Z	Channel width
L	Channel length
k	Boltzmann constant
T	Temperature
q	Electron charge
V_T	Threshold voltage
V_D	Constance drain voltage
V_{GS}	Gate voltage

2.4 Biasing in Strong Inversion

Adding in a voltage on the drain (V_{DS}) creates additional operational parameters through biasing (Pierret, 1990). There are two regimes when biasing the drain: (1) Linear (also called

Ohmic or Triode) and (2) Saturation. Linear occurs when the FET is fully turned on (when $V_{GS} > V_T$) and V_{DS} is set less than the saturation voltage, V_{DSat} (Horowitz and Winfield, 1980; Pierret, 1990). Saturation occurs when the drain voltage is set to greater than V_{DSat} (Horowitz and Winfield, 1980).

When there is a positive voltage, that is lower than the saturation voltage, placed on the drain the depletion region on the drain side gets larger (Pierret, 1990). In this regime, the FET is essentially acting as a resistor (Pierret, 1990). The output current is inversely proportional to the drain voltage. The current from drain to source (or source to drain) in the strong inversion regime (linear/ohmic/triode) goes as (Horowitz and Winfield, 1980; Pierret, 1990)

$$I_{DS,Strong} = \mu_e C_{ox} \frac{X}{L} \left((V_{GS} - V_T) V_{DS} - \frac{V_{DS}^2}{2} \right). \tag{2.4.3}$$

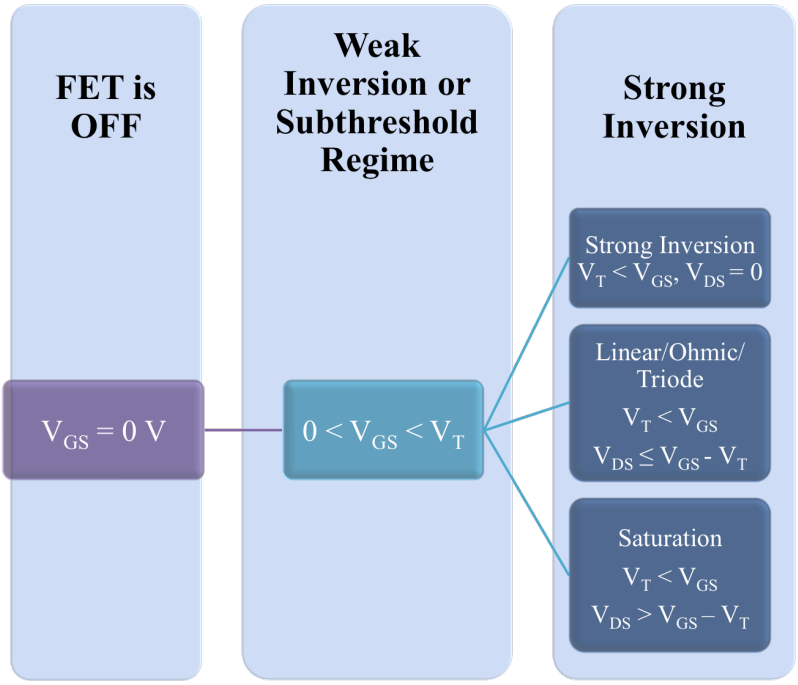

Figure 2.3: Visual description of the multiple modes of operation for a FET.

The saturation voltage can be calculated from the threshold voltage, V_T (Horowitz and Winfield, 1980; Pierret, 1990):

$$V_{DSat} = V_G - V_T. \tag{2.4.4}$$

The drain current in this regime is as follows (Horowitz and Winfield, 1980; Pierret, 1990):

$$I_{DS,Sat} = \frac{1}{2}\mu_e C_{ox}\frac{Z}{L}(V_{GS} - V_T)^2 \tag{2.4.5}$$

The drain current in all of these regimes will be discussed more in section 2.5.

2.5 I-V Characteristics of a MOSFET

One way to characterize a MOSFET is using its current-voltage (I-V) characteristics. Understanding the threshold voltage and turn on characteristics is important to understand the detection mechanism, estimate detector response, and determining the best mode of operation for these detectors (Pierret, 1990). I-V characteristic curves (sometimes referred to as the I-V family of curves) of a FET can indicate biasing voltages for each regime discussed above. There are two curves in particular, Drain Current (I_{DS}) versus Drain Voltage (V_{DS}) and I_{DS} versus Gate Voltage (V_{GS}) (Pierret, 1990). An example curve can be seen in Figure 2.4.

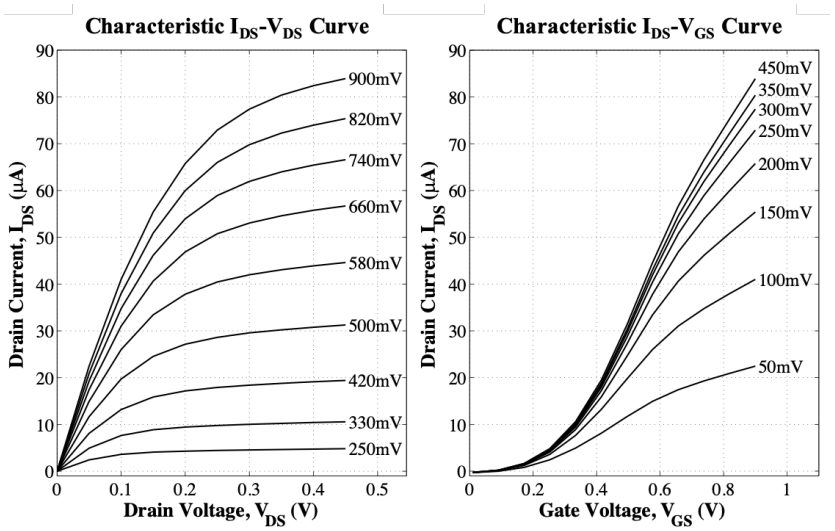

Figure 2.4: Example I-V Characteristic curves for a MOSFET. The left plot is the $I_{DS} - V_{DS}$ curve for various V_{GS} and the right is the $I_{DS} - V_{GS}$ for various V_{DS}.

As discussed previously, placing a voltage on the gate attracts in the substrate just under the gate and, eventually with the threshold voltage, creating the conductive channel. Theo-

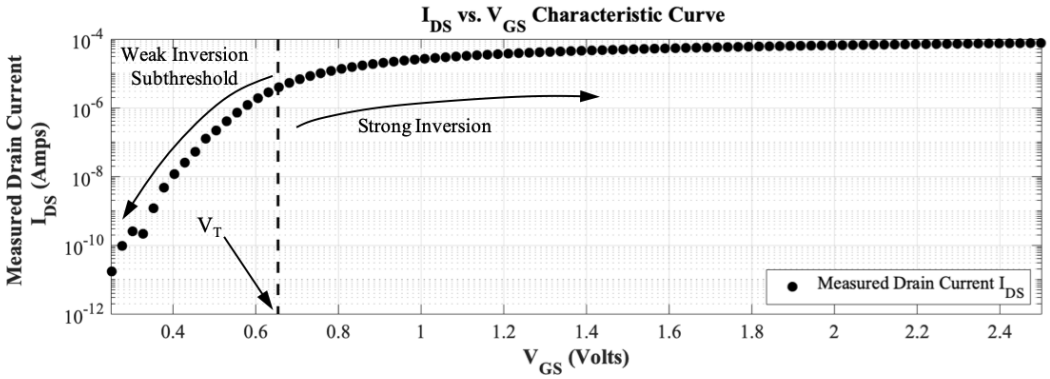

Figure 2.5: Example $I_{DS} - V_{GS}$ characteristic curve for a MOSFET with the weak inversion and strong inversion regimes labeled.

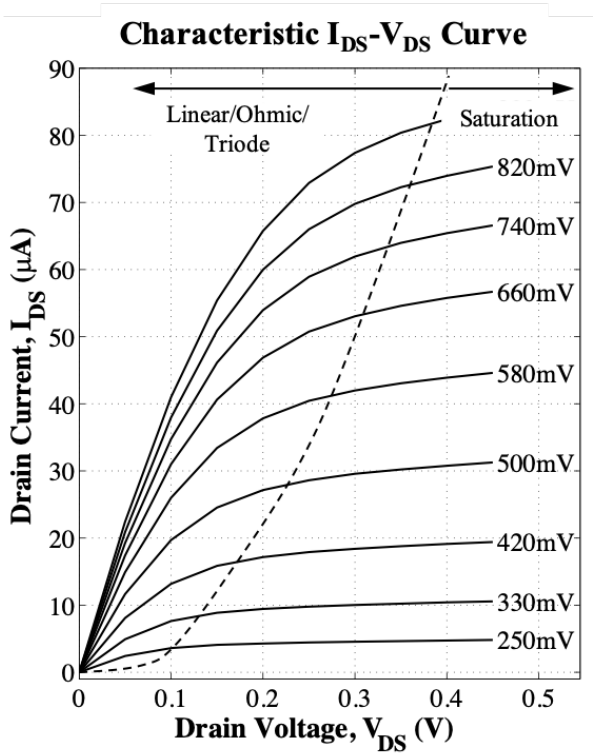

Figure 2.6: Example $I_{DS} - V_{DS}$ characteristic curves (for various V_{GS}) for a MOSFET with the linear and saturation regimes labeled.

retically, one can calculate the threshold voltage from the following expression:

$$V_T = 2\phi_F + \frac{K_S x_o}{K_O}\sqrt{\frac{4qN_A}{K_S\epsilon_0}\phi_F} \tag{2.5.6}$$

where ϕ_F is the reference voltage in relation to semiconductor doping concentration and $\phi_F = (kT/q)ln(N_A/n_i)$ where n_i is intrinsic carrier concentration, K_S is semiconductor dielectric constant, K_O is oxide dielectric constant, N_A is the bulk semiconductor doping level, x_o is oxide thickness, and ϵ_0 is the permittivity of free space (Pierret, 1990).

Some of the parameters above may be unknown and the threshold voltage may not be able to be calculated theoretically. The threshold voltage of the device can be found experimentally using the method described in section 2.2 of (Ortiz-Conde et al., 2002) that is called the extrapolation in the linear region (ELR). As described by the equation above, the drain current in the subthreshold region is a function of gate voltage. Plotting the drain current (I_{DS}) versus V_{GS} (I_{DS}-V_{GS} curve), the threshold voltage can be estimated (Ortiz-Conde et al., 2002). The I_{DS}-V_{GS} curve will look like Figure 2.7. In the I_{DS}-V_{GS} curve, there is a region called the linear region (around I_{DS} of 0.5 to 0.7 V in the example in Figure 2.4) where the drain current depends linearly on gate voltage. By finding the point where the slope is the greatest and fitting a line to it, the threshold can be found where the line intercepts the gate voltage axis (Ortiz-Conde et al., 2002; Sze and Ng, 2007). This is illustrated in Figure 2.7.

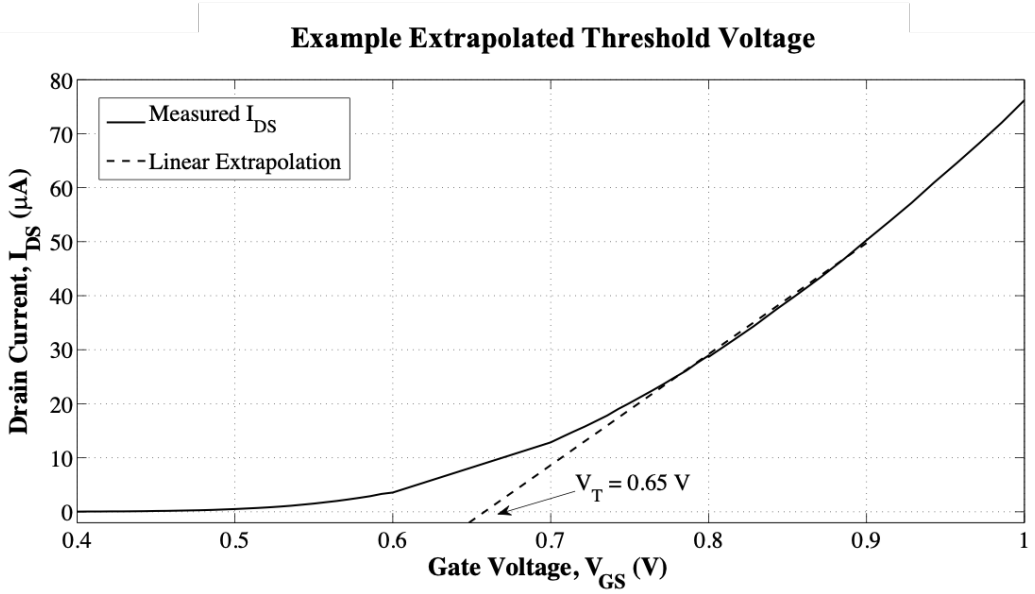

Figure 2.7: Example of using the ELR method to find the threshold voltage.

Chapter 3

Devices and Experimental Setup

The devices presented in this dissertation were designed and tested with RIT in collaboration with the University of Rochester and Harris Corporation. The pixels included an extended source region. The original hypothesis was that increasing the source region increased the resistance of that region which would lead to better antenna matching. This will be discussed more in the next section.

The first generation designs showed a much larger increase in response with extended source extension than expected. This result informed the future designs and approach for this dissertation. The next few sections will detail the different devices. The third generation (GEN3) was tested entirely by the University of Rochester and will not be outlined here.

Each of the devices presented here were designed by the collaboration, fabricated in the Metal Oxide Silicon Implementation Service (MOSIS) facility by the Taiwan Semiconductor Manufacturing Company Limited (TSMC), and packaged in Malaysia.

3.1 Antenna Designs

To detect THz radiation, an antenna must be attached to a FET in order to couple the radiation into the device. The antennas on the devices in this work are mainly bow-tie antennas. One petal of the antenna is attached to the gate and the other petal is attached to the source contact (shown in Figure 3.1). This configuration will be expanded upon more in Chapter 4.

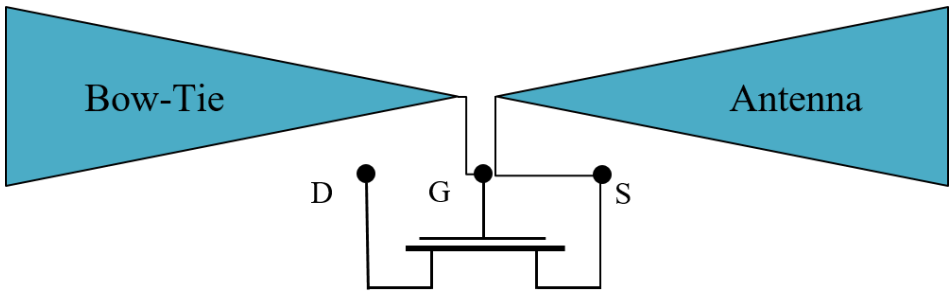

Figure 3.1: Illustration of how the bow-tie antennas are attached in a THz detector configuration.

As a receiving antenna, these antennas take the electromagnetic radiation (THz) and convert it into electrical signals (current, voltage). The electromagnetic field induces charges within the conducting antenna to move resulting in the signal. This works in reverse for transmitter antennas, a current is run through the antenna which emits EM radiation. In order for the maximum transfer of power, the antenna impedance should match the load impedance, otherwise some energy will be reflected back to the ends of the antenna and lost. This is called the maximum power transfer theorem (Carr, 2001).

The antennas used for this work are quarter wave antennas. The total length is determined by the wavelength divided by four. These aluminum antennas are surrounded by silicon oxide on the chips, so the index of refraction of the silicon oxide must be taken into account when determining the length:

$$l = \frac{\lambda_{medium}}{4} = \frac{1}{4}\frac{c}{nf}. \tag{3.1.1}$$

A majority of the devices discussed in this work are the bow-tie antennas but there are a few dipole antennas as well. In his thesis, Chao Zhang modeled different antenna configurations. After the first experiments were complete by the collaboration, Zhang used extrapolated material properties—extrapolated from curves in the microwave and IR regimes—to redesign antennas for the single frequency Gunn diode 0.188 THz source. The responses of different shapes of antennas were simulated and the bow-tie antenna with a total length of 220 μm was selected going forward with new designs.

Bow-tie antennas were chosen because the frequency response would be wider than a simple dipole. This would help if the extrapolated material property parameters in the simulations were slightly different than the actual parameters. A microscope close up image of one of the bow-tie antennas can be seen in Figure 3.2.

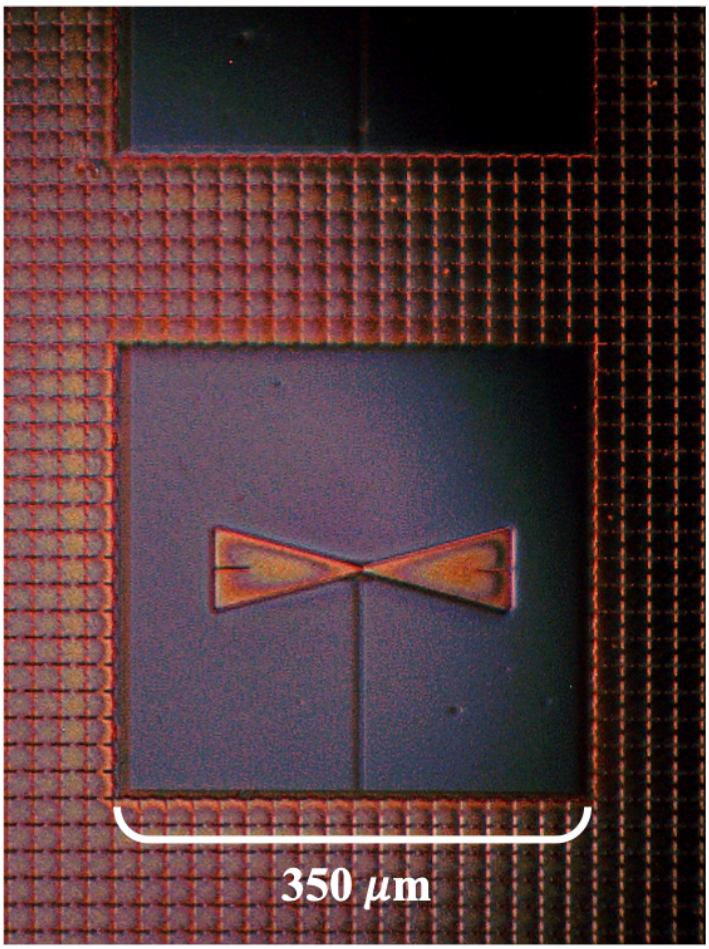

Figure 3.2: A microscope image of a bow-tie antenna on one of the chips.

3.2 Devices Tested: 350 nm Single Test Structures

These devices utilized 350 nm silicon Complimentary Metal Oxide Semiconductor (CMOS) process at TSMC MOSIS. Each design was built using the previous iteration results to inform improvements of the pixel designs. This work will focus on results from the individual test pixels (test structures), not the arrays, on these devices.

3.2.1 First Generation Chip (GEN1)

The first generation of chip design (GEN1) was designed by the collaboration to have four different arrays with separate antenna configurations and included 5 test structures. The whole chip is about 4.7 mm by 4.2 mm and is shown in Figure 3.3 below. The results from the test structures informed future chip designs. This device was characterized by Gregory Fertig in 2014 (Fertig, 2014) but a summary of those results will be discussed.

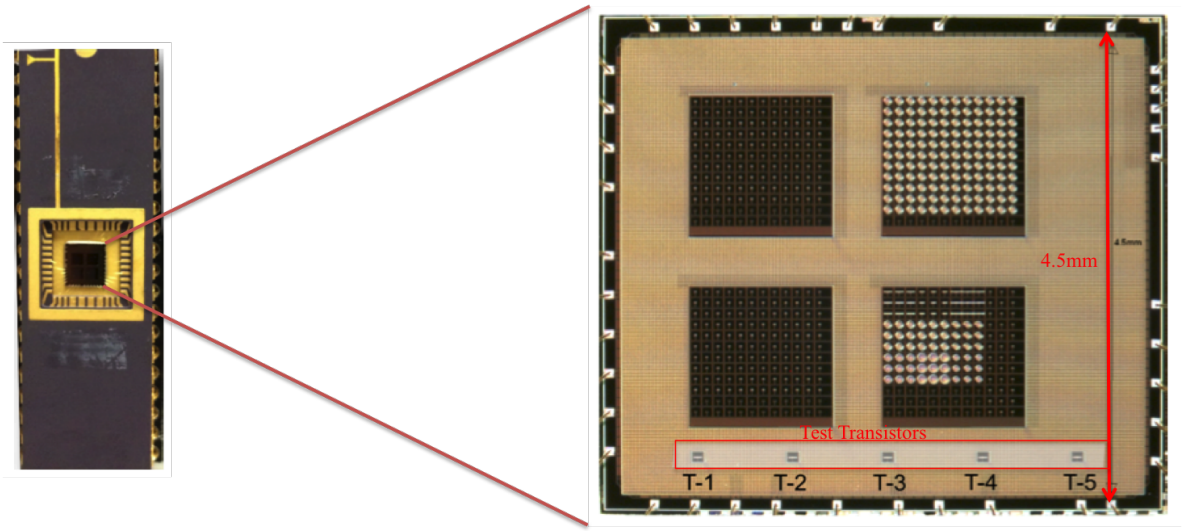

Figure 3.3: First chip design in a DIP40 package (left) and a close up view of the chip with the five individual pixels T1 through T5 highlighted (right). Close up photo taken by the collaboration.

The test structures on this chip were designated test structure 1 (T1) through test structure 5 (T5). The FET and bow-tie antenna designs are all identical with the exception of the source region length. T1 starts with a symmetric, traditional FET where the source and drain length are the same. T2 extends the source region by 0.5 μm as compared to the drain region length all the way up to T5 with a 2.0 μm extension. Table 3.1 contains the dimensions of the five test structures on this chip.

Throughout the testing of these devices, T5 was shown to have the largest response to the 0.188 THz Gunn diode source (see Figure 4.26 in Fertig (2014)). Originally at 1.6 THz source was going to be utilized, but the Gunn diode source was obtained and used for a majority of the experiments. For the next round of pixel designs, we used the T5 extension as a basis and

Pixel Name	Source Extension (μm)	Antenna Length (μm)
T1	0.0	68.4
T2	0.5	68.4
T3	1.0	68.4
T4	1.5	68.4
T5	2.0	68.4

Table 3.1: Table of GEN1 important test FET dimensions.

redesigned the antenna for this source.

3.2.2 Second Generation Chip (GEN2)

The second generation (GEN2) devices included 15 individual test pixels with design variations (e.g., antenna size, source extension length) and one 7x7 pixel T5 imaging array (see Figure 3.5). The naming convention from GEN1 was continued since T5 was the basis of the GEN2 test structures. One test structure, called T5 Old, is a duplicate of the T5 on GEN1, including the antenna, so that a direct comparison could be made to the rest of the designs.

As discussing in section 3.1 Zhang modeled different antennas and determined the dimensions for 0.188 THz (Zhang, 2014). This antenna design was put onto a T5 device in GEN2 and called T5 100%. Figure 3.4 shows the layout and design created for T5 100%. To observe the effect antenna length variations on detector response, T5 90% and T5 110% were designed. The 90 refers to 90% of the length of the 100% antenna and 110% is 110% the length of the 100% antenna. These were chosen to see the effect of a change of $\pm$10% in length. A wider bow-tie antenna was designed onto T5 Fat Bow-tie to observe the effect on frequency response. Many other characteristics were varied including a wider gate, longer channel, et cetera. There is also a T6 and T7 which each have the 100% antenna and use a 2.5 μm and 3.0 μm source extension respectively. The details of each FET can be seen in Table [INSERT ref]. The purpose of the GEN2 chip test structures was to optimize FET and antenna designs to create better future designs and to observe the way that each variation affected response.

The GEN2 devices were mainly run in current-mode, meaning a voltage was placed on the gate, the drain was biased with a voltage and the current was measured from the source. This

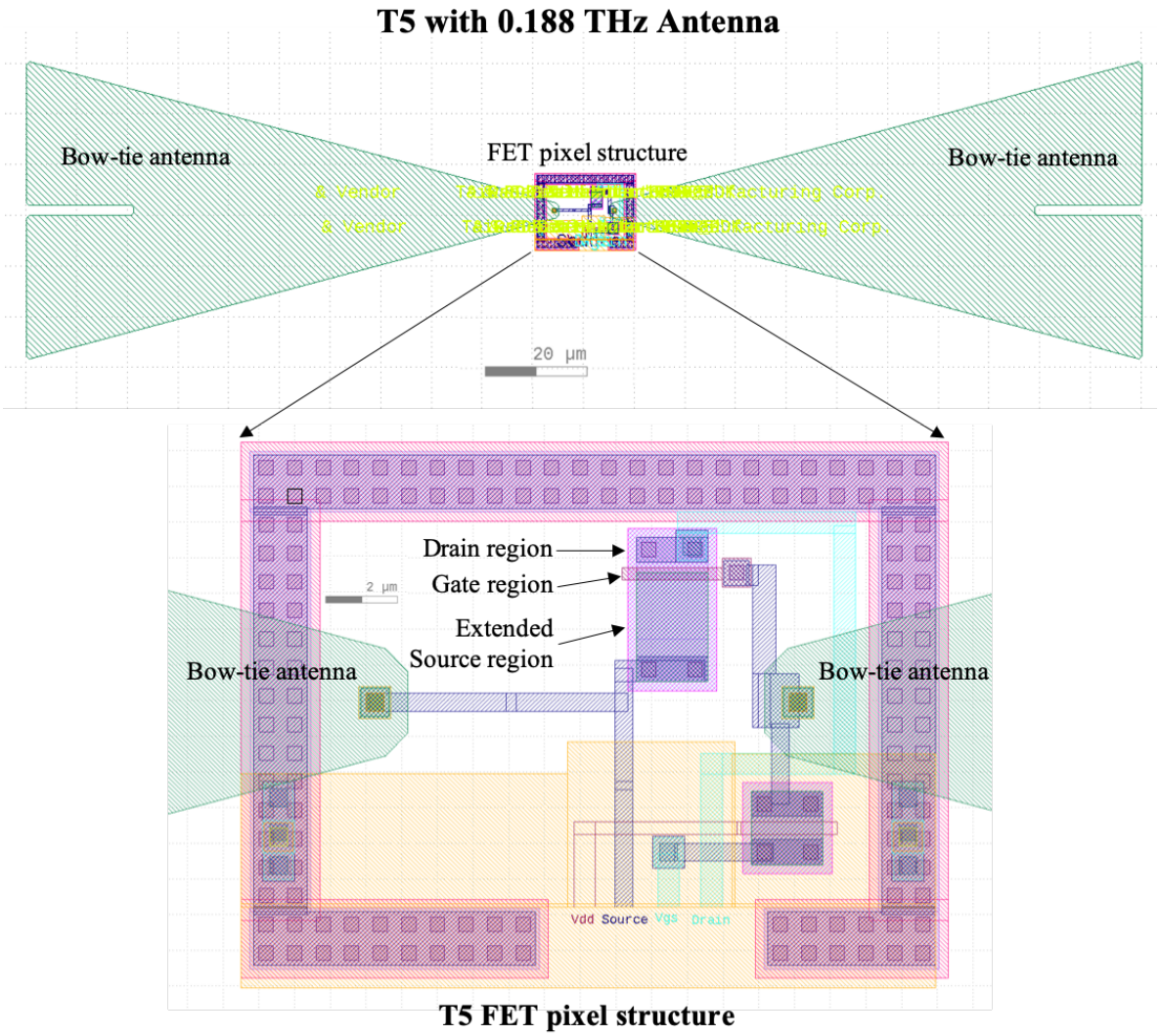

Figure 3.4: The GDS (global database system file format) layout of T5 100% with important areas highlighted. Design by Zeljko Ignjatovic.

was done to better understand the way the devices worked and the noise inherent within the FETs.

3.2.3 Fourth Generation Chip (GEN4)

The fourth generation (GEN4) design consists of only individual test structures with different variations of designs. GEN4 was mostly run in voltage mode for three reasons: (1) the large drain current inherent in the devices, (2) as compared to the much smaller THz-induced signal

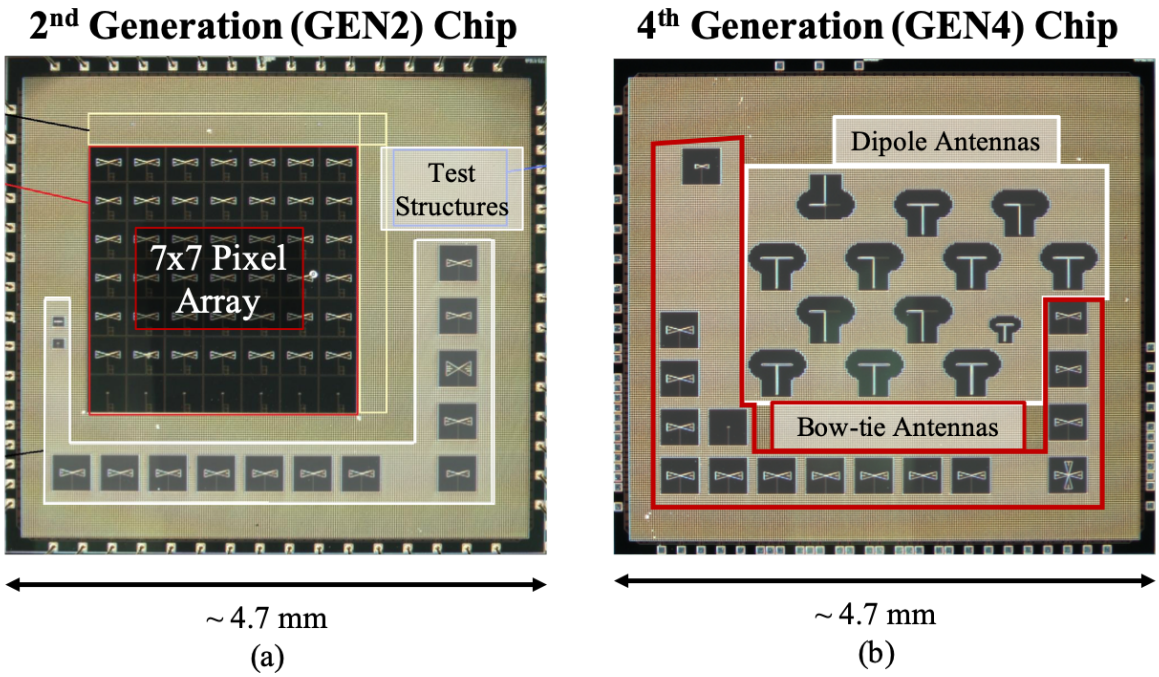

Figure 3.5: The GEN2 (a) and GEN4 (b) images highlighting the major features on each chip taken by the collaboration.

current, and (3) an accurate method of comparison to other THz MOSFET devices was needed and most other works report their responsivity in V/W. Voltage mode consisted of placing a voltage on the gate, grounding the source, and measuring the voltage between the drain and source (or rather drain and ground).

In order to explore the effect of source extension on responsivity, T1 (no source extension—symmetric source and drain) through T10 (4.5 μm source extension) were included in this generation. All 10 of these pixels utilize the 110% antenna (242 μm long) from the previous generation because it resulted in the best response (Horowitz, 2017; Katherine E. Seery, 2018). The rest of the various test structures are all of the same design as T5 (2 μm source extension) with different antenna configurations. There is a T5 Dual Polarization pixel that utilizes 2 bow-tie antennas with one at 90 degrees rotation to the other. This pixel was an attempt to see if a response could be obtained in two polarizations (0 and 90 degrees) on the same FET. There is also a T5 source-drain antenna where the petals of the bow-tie antenna are attached to the source and the drain instead of source and the gate. Other antenna configurations

fall into two categories: CPW (coplanar waveguide) and BSC (broad-side connection) dipole antennas. Variations in the dipole antennas include waveguide widths (2, 3, and 4 μm wide) and antenna length.

The same setup for the previous generation chip was utilized for this generation because the design was developed utilizing the same layout scheme. In order to accommodate twice as many pins for the extra test structures, there was two wire bonding packaging configuration (package A and package B).

The threshold voltage was determined through the ELR method as described in section 2.5. The 350 nm devices are all roughly the same threshold voltages with some manufacturing variation of no more than 10%. The ELR for the 350 nm devices is 0.65 V. T5 110% was taken as the model device in future generation designs.

3.3 65 nm Single Test Structures

This chip design was created using a 65 nm process through MOSIS. Twenty-five pixels were designed as a scaled version of the THz pixels for 30 THz (10 μm wavelength) to see how the response changed in a purely scaled structure. These pixels will not be detailed in this work. There are three pixels designed for 0.2 THz similar to the previous generation chips.

This work will focus only on the 0.2 THz pixels. The three pixels use the T4 design based on the source extension study conducted with the GEN4 source extension series. The bow-tie antenna design could not be used in this process because of the design rules for contiguous metal and corners. A dipole antenna configuration based on the GEN4 devices was used. This chip was packaged in two different configurations to wire out all of the devices. T4 with waveguide and T4 no antenna were in one configuration (package A) and T4 no waveguide and T4 no antenna were included the other configuration (package B). The package A chip was the package tested. T4 no antenna did not respond to 200 GHz as expected from previous results, so the data and analysis presented here will be given for T4 with waveguide. These devices were run in voltage mode like the GEN4 devices.

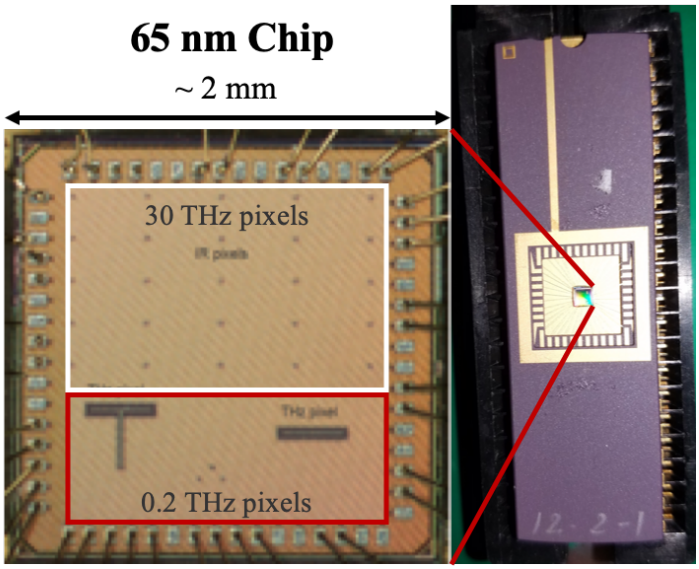

Figure 3.6: Left: The 65 nm chip micrograph image with the different pixels highlighted. Photo taken by the collaboration. Right: The 65 nm chip packaged into a DIP40 package.

3.4 10x10 Pixel Imaging Array (350 nm)

The last set of chips manufactured to be discussed in this work is an integrated 10x10 pixel focal plane array manufactured using the 350 nm CMOS process. The chip has on-chip amplification of 1, 10, or 100 and memory per pixel to set each pixel to its own V_{GS} value within a range set on a control board. The range has been set to 0.37 to 0.44 V. These devices are run by grounding the sources, setting a small current—0.2 μA—onto the drain (similar to GEN1), setting the gate voltage, and measuring out the resulting voltage on the drain. In his dissertation, Moeen Hassanalieragh details the unique amplification and readout scheme designed for this chip (Hassanalieragh, 2019).

All 100 pixels were manufactured to be same design—T5 100%—with the 2 μm source extension and a 220 μm long bow-tie antenna. The PCB board with onboard analog-to-digital converter (A/D) fit within the same Dewar as the previous generations. The Dewar was placed onto a manual vertical stage on an optical table for alignment adjustments. The THz source was placed on another manual vertical stage on the other side of optical table. A motorized XY translational stage was set up in the center between the source and imager where an object could be mounted for transmission raster scan imaging experiments (see Figure 3.8). A

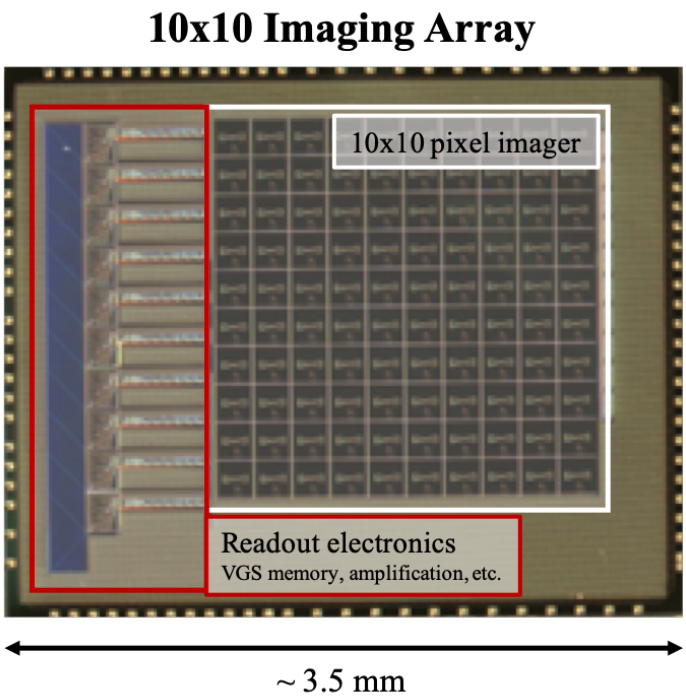

Figure 3.7: The 10x10 imaging array chip micrograph image taken by the collaboration showing the array and image readout electronic areas highlighted.

Teflon lens (opaque to visible wavelengths) was used to collimate the THz beam to uniformly illuminate the object from behind.

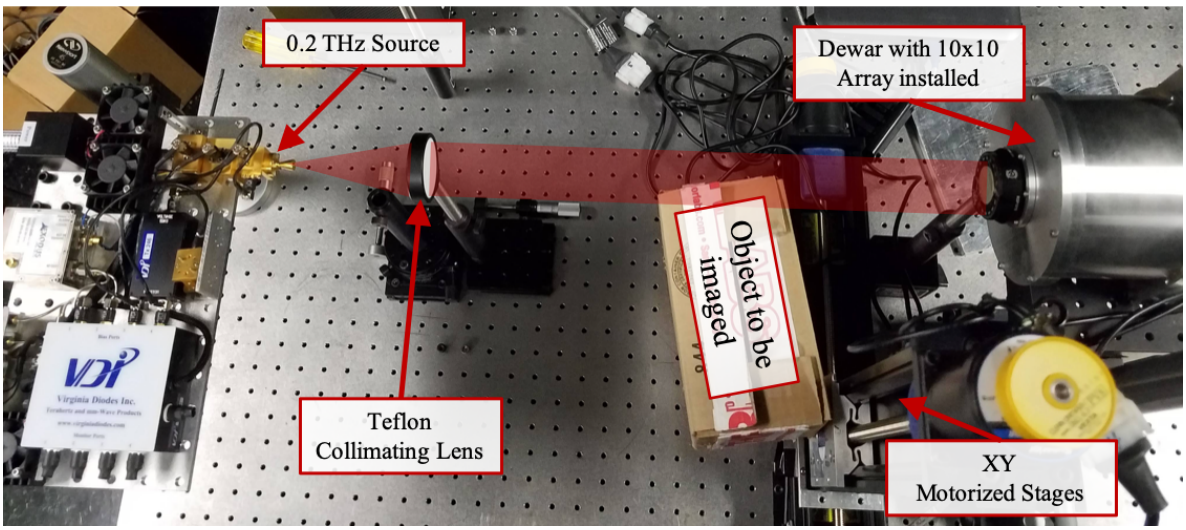

Figure 3.8: An image of the 10x10 imaging array demonstration setup.

3.5 Experimental Setup

Each of the chip designs utilized control boards that would wire out the signals to and from the device under test (DUT). These boards have been mainly designed by Craig McMurtry at the University of Rochester. Each design has be made so that it fits into the custom Dewar.

The GEN2 and GEN4 chips were both wired out into the same package in a similar manner so that the chips could be inserted into the same control boards. A notional diagram of the basic experimental setup can be seen in Figures 3.9 and 3.10. A lock-in amplifier was utilized to sample the devices at a specified frequency instead of DC in some situations to lower the noise of the measurements, like sampling at higher frequencies to avoid more 1/f noise. 1/f noise is described later in section 5.3.

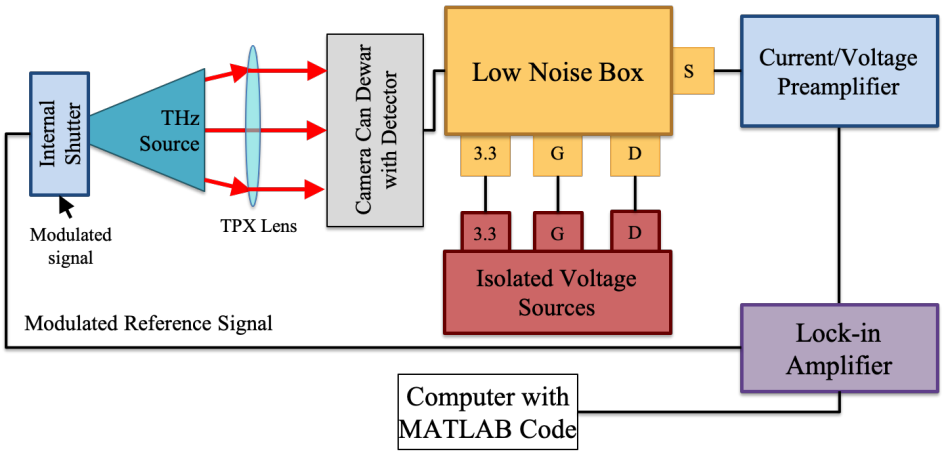

Figure 3.9: A notional block diagram of how the devices were run when modulating the source a specified chopping frequency and using the lock-in amplifier to measure the THz signal from the devices at that frequency.

3.5.1 THz Sources

Three different THz sources were used throughout this work (Figure 3.11). Each of them were made by Virginia Diodes, Inc (VDI). In addition, each utilized the same conical horn antenna to spread out the beam into a Gaussian profile. The first is a 0.188 THz Gunn Diode with approximately 50 mW of power out. The second was a tunable frequency Gunn Diode with about 5 mW of power out. The tunable source could be tuned from 0.17 to 0.25 THz. This

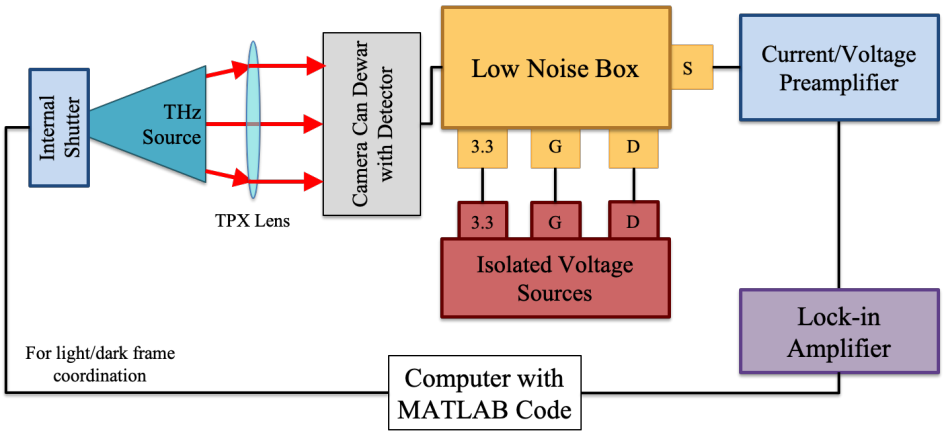

Figure 3.10: A notional block diagram of how the devices were run when utilizing no source chopping and measuring just the DC measurement ability within the lock-in amplifier.

allowed for small-scale frequency characterization of the device responses. Lastly, a 150 mW 0.2 THz source was used.

In order to uniformly illuminate the FETs for characterization, a collimation lens was used. Two types of lenses were utilized throughout this work, a Polymethylpentene (TPX) lens and a Teflon lens. The TPX lens has a similar index of refraction in the THz as with visible wavelengths and transparent to visible light making alignment with a laser simple. Teflon is opaque to visible wavelengths so a sub-wavelength sized hole was drilled through the center of the lens to allow for laser alignment of the source-lens-detector system. The hole did not change the characteristics of the beam since it was sub-wavelength.

3.5.2 Power Meter and Wire-Grid Polarizer

A majority of THz detector groups estimate the power falling on the detector to estimate responsivity of devices. In order to better calculate responsivity and calibrate the detectors, we used a calorimeter from VDI, the Erickson Power Meter 5 (PM5). This measured the power in Watts falling onto the 1092 μm by 546 μm rectangular waveguide opening of the PM5. The PM5 measures the power of millimeter wave radiation, responding to frequencies from 75 GHz up to 3 THz (3000 GHz), and measures powers of less than 1 μW to 200 mW. The PM5 was mounted onto a plate next to the custom Dewar with the DUT (Figure 3.12. This plate was

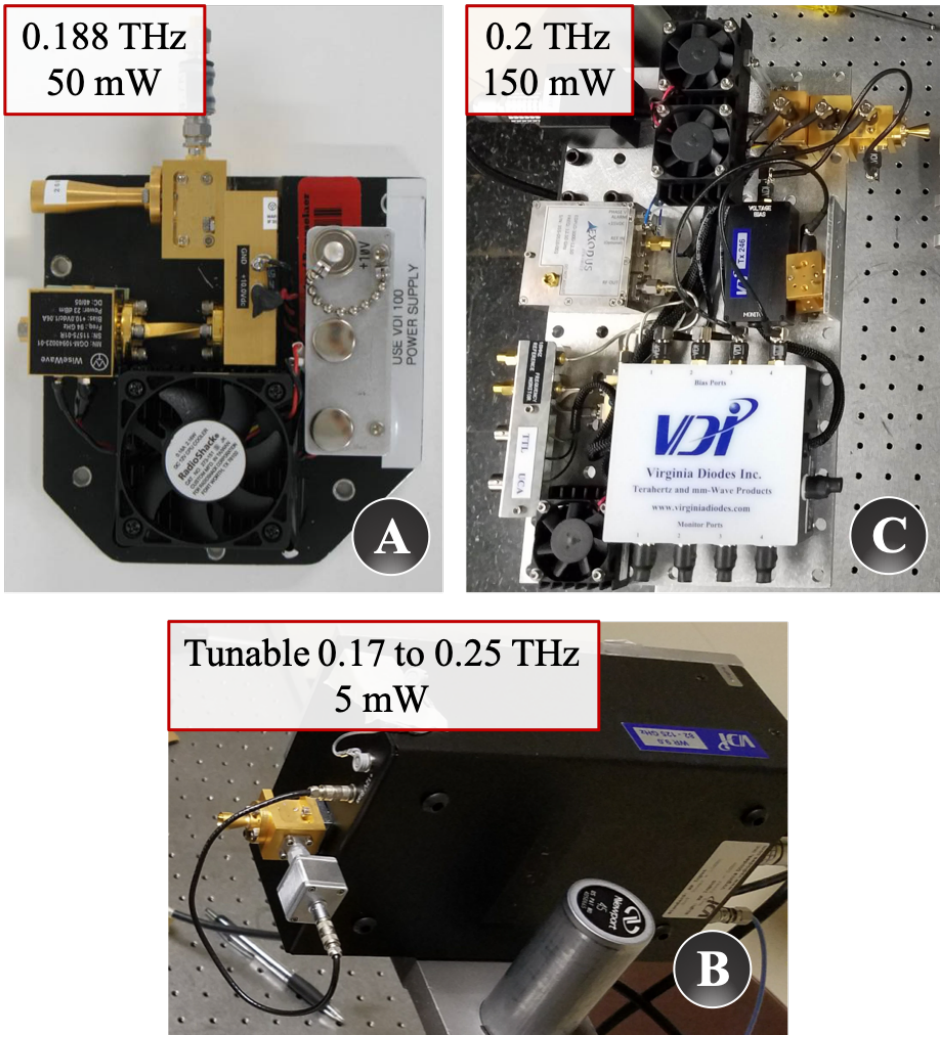

Figure 3.11: The three THz sources utilized in this work: (A) 50 mW Gunn diode, (B) a tunable frequency 5 mW Gunn diode, and (C) a 150 mW Gunn diode.

then mounted onto motorized XYZ stages. The distance between the waveguide opening on the PM5 and the DUT in the dewar was determined and programmed into the MATLAB code that controlled the stages.

Along with uniformly illuminating the chips, a collimated beam ensured that the light was better able to couple down the waveguide on the PM5 and obtain a more accurate measure of the power reaching the chip. Measurements from the PM5 were taken immediately before or after a measurement from the DUT FET so that each measurement could be calibrated to the source power and the different FETs could be compared more accurately. In addition to

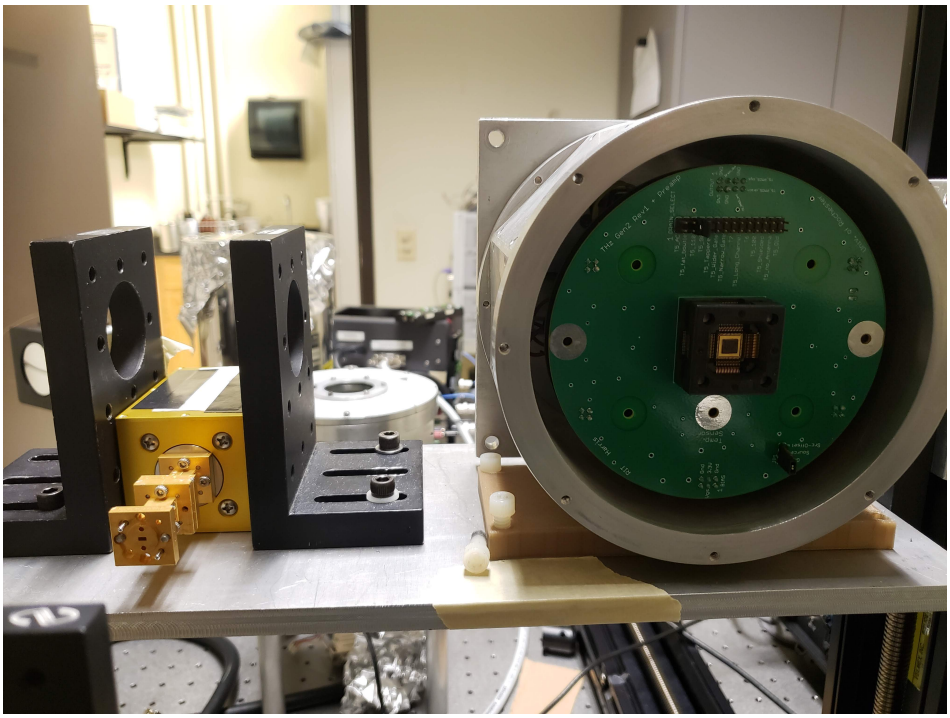

Figure 3.12: The custom Dewar mounted on the plate on the XYZ stages along with the PM5.

coupling the radiation down the waveguide, it also resulted in a uniform illumination of the DUT.

One key experiment for characterizing the detector responses was illuminating the devices with different levels of power. To do this, a wire-grid polarizer was designed to reduce power by a known amount (see Figure 3.13). The polarizer was designed simply through a printed circuit board (PCB). The wire widths and spacing between the wires were designed to be $\frac{\lambda}{10}$. Taking 200 GHz for the frequency, the wavelength is 1.5 mm making the spacing and wire widths 150 μm.

The wire-grid polarizer works on a simple principle of only allowing certain polarizations of light to pass through. The three THz sources are linearly polarized. If linearly polarized light is aligned correctly with the wires, all the light passes through. If the light is antialigned (90 or 270 degrees off), no light will pass through. With angles, only a certain amount of light will pass through. The ideal polarizer works on a simple cosine squared power fall off with angle. This was verified by using the PM5 and can be seen in Figure 3.14.

Figure 3.13: The wire-grid polarizer designed for 0.2 THz using PCB mounted on a manual rotational stage.

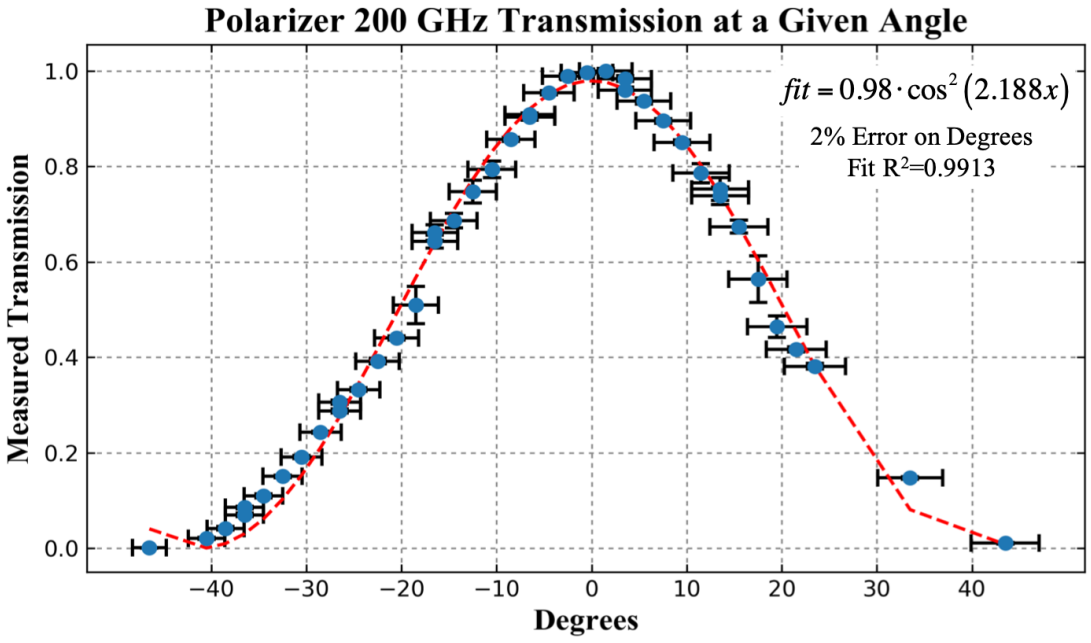

Figure 3.14: Cosine squared power falloff relation of the wire-grid polarizer verified.

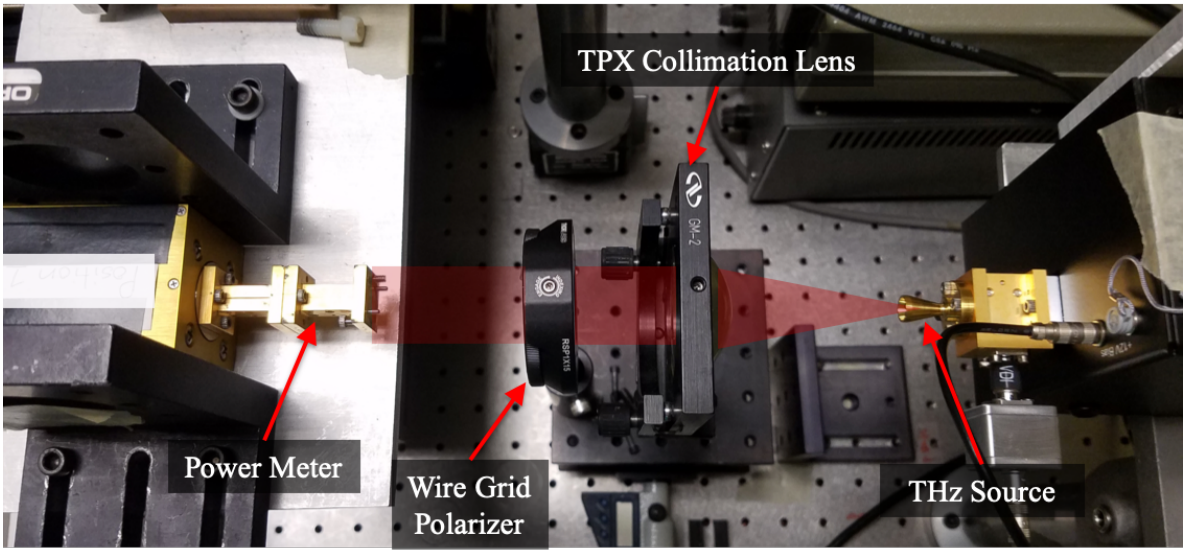

Figure 3.15: A photograph of the measurement setup for verification of the cosine squared power relation for the wire-grid polarizer. The main equipment is highlighted, along with an illustration of the basic beam in red.

3.5.3 Preamplifier Board

Originally, the source was being modulated at a specific chopping frequency to utilize the Stanford Research Systems SR850 lock-in amplifier. The lock-in amplifier had many functions including a built in A/D for DC signals. It was utilized both in sampling at a specific frequency (usually 1 kHz which was the THz sources' internal shutter limit) and when the signal was large enough, the A/D without modulating the sources.

After determining the needs from measuring with the lock-in amplifier a preamplifier board (preamp board) was designed by the collaboration to increase signal and decrease noise close to the chip without needing the voltage or current amplifiers. This board utilized filtering to reduce noise and increase the signal of the chip. This board was designed to be a precursor experiment to an on chip amplification scheme for future applications.

The preamp board was designed as a daughter board to plug into the PCB board holding and wiring out the chip pins. There are multiple circuits on the board in order to test out different readout methods. THz-induced voltage or current can be read out of the device depending on the mode of operation. In order to accommodate different readout methods,

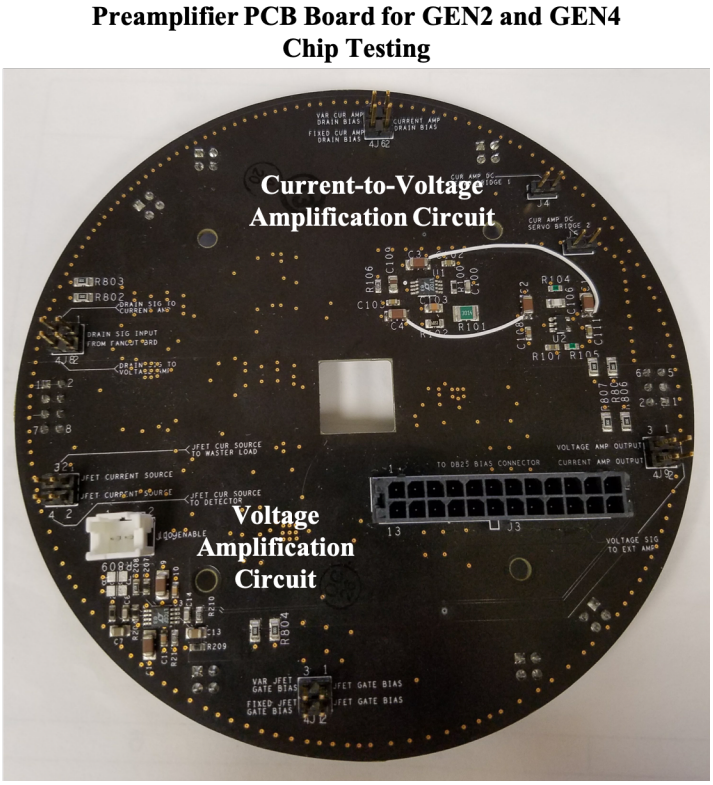

Figure 3.16: A photograph of the preamplifier board with the two main amplification circuits highlighted.

jumper pins on the board were added to allow for selection of readout method. In addition to amplification, the circuits contained some noise filters.

Chapter 4

THz Detection in Si-MOSFETs

Dyakonov and Shur first theorized using transistors as THz detectors in the 1990s (Horowitz, 2017; Fertig, 2014). They proposed a plasmonic detection theory in high electron mobility transistors (HEMTs) (Horowitz, 2017; Fertig, 2014). Later, this THz plasmonic theory was extended to Si-MOSFETs (Horowitz, 2017; Fertig, 2014). The theory was detailed for Si-MOSFETs used above threshold. Observations detailed in this work and others show a maximum detection within the subthreshold to threshold of the devices. This made the plasmonic theory incomplete and invalid for the behavior seen near and below threshold in Si-MOSFETs (Knap et al., 2002). The data from the devices diverged from the theoretical curves at and around the threshold in Knap et al. (2002). In the subthreshold regime, the channel is almost depleted of electrons (Horowitz, 2017) and plasmonic theory does not account for this. The electrons in Si-MOSFETs also have much less mobility compared to the HEMT devices that the theory was based on. The dielectric relaxation frequency within the channel is much lower than THz frequencies. In 2002, Knap et al. (2002) explored the idea of subthreshold plasmonic detection described within the next section.

The results described in this work also have the added feature of an asymmetric source-drain geometry. This feature enhances the THz response (Ryu et al., 2014). This chapter will describe the plasmonic theory that has been used to describe the detection mechanism, outline the theory for the subthreshold detection mechanism, and discuss the enhancement.

4.1 Plasmonic Detection Theory

The electrons within the channel underneath the gate can be conceptualized as an electron fluid. When exposed to THz, the electron fluid can become a resonator and form plasmon waves. These waves change the current within the device which can quantify the radiation (Dyakonov and Shur, 1993, 1996; Fertig, 2014; Knap et al., 2013; Tauk et al., 2006).

Using hydrodynamic equations to describe this fluid, one can calculate this current (Dyakonov and Shur, 1993, 1996; Fertig, 2014).

$$\frac{\partial v}{\partial t} + v\frac{\partial v}{\partial x} + \frac{q}{m}\frac{\partial U}{\partial x} + \frac{v}{\tau} = 0 \tag{4.1.1}$$

This equation of motion can be solved using the local energy conservation continuity equation along with the gradual channel approximation to get (Dyakonov and Shur, 1996; Fertig, 2014; Popov et al., 2011)

$$\frac{\partial U}{\partial t} + \frac{\partial U_v}{\partial x} = 0 \tag{4.1.2}$$

This mechanism depends on the fundamental plasma harmonic frequency, ω_0, and momentum relaxation time, τ Knap et al. (2013). $\omega_0 = \frac{s\pi}{2L_g}$ and τ is on the order of 10^{13} to 10^{14} seconds at room temperature (Zak et al., 2014). The FET becomes a resonant detector when there is high mobility ($\omega_0\tau \gg 1$) (Knap et al., 2013). When $\omega_0\tau \ll 1$, the FET is in a non-resonant detection because the plasma oscillations are overdamped (Fertig, 2014; Knap et al., 2013; Tauk et al., 2006). Plasma wave velocity within the FET can be calculated by the following:

$$s^2 = s_0^2\left[1 + \exp\left(\frac{-qV_0}{\eta kT}\right)\right]\ln\left[1 + \exp\left(\frac{-qV_0}{\eta kT}\right)\right] \tag{4.1.3}$$

where $s_0 = \sqrt{\frac{\eta kT}{m}}$, $V_0 = V_G - V_T$ (V_G is the DC gate voltage and V_T is the threshold voltage), η is the ideality factor (Knap et al., 2013). For more steps, Dyakonov and Shur (1996) go through the derivation of the detection (Fertig, 2014; Knap et al., 2013; Dyakonov and Shur, 1993, 1996).

There are two types of detection: resonant and non-resonant detection. Resonant detection

occurs when $\omega_0\tau_r > 1$ where ω_0 is the fundamental plasmon wave frequency (Fertig, 2014; Dyakonov and Shur, 1993, 1996). The electron relaxation time, $\tau = \mu m_e m_0/q$ where μ is electron mobility within the FET channel, m_e is effective electron mass, m_0 is rest mass of electrons and q is the charge of an electron. ω_0 is calculated as:

$$\omega_0 = \frac{\pi}{2L}\sqrt{\frac{q(V_{GS} - V_T}{m_e}} = \frac{\pi s_p}{2L} \tag{4.1.4}$$

where s_p is the plasmon wave velocity defined as (Fertig, 2014; Dyakonov and Shur, 1993, 1996):

$$s_p = \sqrt{s_0^2(1 + exp\Big(-\frac{qU_0}{\eta k_B T}\Big))ln(1 + exp\Big(\frac{qU_0}{\eta k_B T}\Big))} \tag{4.1.5}$$

In current Si-MOSFETs, electron mobilities are not high enough to support this type of detection. Resonant detection occurs in higher mobility devices like HEMTs (Fertig, 2014; Dyakonov and Shur, 1993, 1996). Non-Resonant detection occurs in Si-MOSFETs. This occurs when $\omega_0\tau_r \ll 1$. The idea here is that the plasmon wave is over-damped prior to reaching the drain side of the channel (Fertig, 2014; Dyakonov and Shur, 1993, 1996). There are multiple theories on determining the detector response due to the two regimes: subthreshold and above threshold. Subthreshold plasmonic response is not well defined and currently does not agree with many of the experimental results from many groups, including this work. For threshold and above, the photoinduced voltage is calculated through (Gutin et al., 2012)

$$\Delta U = \sqrt{V_{GS}^2 + \frac{U_a^2}{2}} - V_{GS} \tag{4.1.6}$$

4.2 THz Detection in the Subthreshold Regime

Above threshold of a MOSFET, the leakage current from the metal gate is small when the current in the channel is high (Knap et al., 2002). When the channel is very small near the threshold of the device, this is not the case and the gate leakage is important to take into account (Knap et al., 2002). The original plasmonic theory did not take this regime into account and only described the detection above threshold. We will follow along with the

theory described in Knap et al. (2002). In the subthreshold regime, electron concentration in the channel is described as

$$n = n^* exp\left(\frac{q(V_G - V_T)}{\eta k_B T}\right) \tag{4.2.7}$$

where η is the ideality factor. In Knap et al. (2002), they start again with the hydrodynamic equations for the electrons in the channel equations 4.1.1 and 4.1.2. Following along the procedure in Knap et al. (2002). This is where we diverge from the previous original above threshold theory and include the gate leakage current. We add in gate leakage current density j_0 and neglecting $\frac{\partial v}{\partial t} + v\frac{\partial v}{\partial x}$ which is small compared to the other terms, one is left with

$$v = \frac{q\tau}{m}\frac{\partial u}{\partial x} \tag{4.2.8}$$

$$\frac{\partial n}{\partial t} + \frac{\partial (nv)}{\partial x} = j_0/q \tag{4.2.9}$$

with boundary conditions of $u\big|_{x=0} = U_0 + u_a cos(\omega t)$ and $v\big|_{x=L} = 0$. From equations 4.2.8 and 4.2.7 one gets:

$$v = -\frac{s_0^2 \tau}{n}\frac{\partial n}{\partial x} \tag{4.2.10}$$

where $s_0 = \sqrt{\frac{\eta k_B T}{m}}$. This can then be substituted into equation 4.2.9.

$$\frac{\partial n}{\partial t} - s_0^2 \tau \frac{\partial^2 n}{\partial x^2} = j_0/q \tag{4.2.11}$$

with boundary conditions $n\big|_{x=0} = n^* exp(A(U_0 + u_a cos(\omega t)))$ and $\frac{\partial n}{\partial x}\big|_{x=L} = 0$ where $A = \frac{q}{\eta k_B T}$.

After expanding the first boundary condition and using it in equation 4.2.11 we get:

$$n = n^*\left[1 + \left(\frac{qu_a}{2\eta k_B T}\right)^2\right] exp\left(\frac{qU_0}{\eta k_B T}\right) + \frac{j_0}{s_0^2 \tau q}\left(xL - x^2/2\right) + \frac{qu_a n^*}{2\eta k_B T} exp\left(\frac{qU_0}{\eta k_B T}\right) \times\left[\frac{ch(a[L-x])}{ch(aL)} e^{i\omega t} + \frac{ch(a^*[L-x])}{ch(a^*L)} e^{-i\omega t}\right] \tag{4.2.12}$$

where ch is shorthand for the hyperbolic cosine (cosh) and

$$\begin{aligned} a &= \sqrt{\frac{i\omega}{s_0^2\tau}} \\ a* &= \sqrt{\frac{-i\omega}{s_0^2\tau}} \end{aligned} \tag{4.2.13}$$

Using equation 4.2.7, the drain voltage ($u\big|_{x=L}$) can be determined by:

$$u\big|_{x=L} = \frac{\eta k_B T}{q} ln \frac{n\big|_{x=L}}{n^*} \tag{4.2.14}$$

By substituting this equation into equation 4.2.12 we get

$$\begin{aligned} u\big|_{x=L} = U_0 + \frac{\eta k_B T}{q} ln \Bigg[a + \left(\frac{q u_a}{2\eta k_B T} \right)^2 + \frac{j_0 L^2}{2 s_0^2 \tau q n^*} \\ + \frac{q u_a}{2\eta k_B T} \left[\frac{e^{i\omega t}}{ch(aL)} + \frac{e^{-i\omega t}}{ch(a^* L)} \right] \Bigg] \end{aligned} \tag{4.2.15}$$

If we expand the logarithm and average over time, we get

$$\frac{q u_a^2}{4 m s_0^2} \left[\frac{1}{1 + \kappa exp\left(\frac{-qU_0}{\eta k_B T}\right)} - \frac{1}{\left[1 + \kappa exp\left(\frac{-qU_0}{\eta k_B T}\right)\right]^2 ch(aL) ch(a^* L)} \right] \tag{4.2.16}$$

where

$$\kappa = \frac{j_0 L^2 m q}{2 C \tau \eta^2 k_B^2 T^2} \tag{4.2.17}$$

which is assumed to be small and much less than 1. Utilizing equation 4.1.3 for arbitrary gate voltage (above or below threshold), we get

$$\Delta u = \frac{q u_a^2}{4 m s^2} \left[\frac{1}{1 + \kappa exp\left(\frac{-qU_0}{\eta k_B T}\right)} - \frac{1}{\left[1 + \kappa exp\left(\frac{-qU_0}{\eta k_B T}\right)\right]^2 \left[sh^2 Q + cos^2(Q) \right]} \right] \tag{4.2.18}$$

where sh is shorthand for hyperbolic sine (sinh) and $Q = \sqrt{(\omega/2\tau) L/s}$. There are a few limiting cases for equation 4.1.3 that reduce the equation. For example, $qU_0 > \eta k_B T$ gives $s^2 = qU_0/m$ and for $U_0 < 0$ and $q|U_0| > \eta k_B T$ gives $s^2 = s_0^2$.

Equation 4.2.18 can be simplified to

$$\Delta u = \frac{q u_a^2}{4\eta k_B T}\left[\left[1+exp\left(-\frac{qU_0}{\eta k_b T}\right)\right]\left[1+\kappa exp\left(-\frac{qU_0}{\eta k_b T}\right)\right] ln\left[1+exp\left(\frac{qU_0}{\eta k_b T}\right)\right]\right]^{-1} \quad (4.2.19)$$

When $qU_0 \gg \eta k_B T$

$$\Delta u = \frac{u_a^2}{4U_0} \quad (4.2.20)$$

but now when $U_0 < 0$ (subthreshold) for our case Δu finally becomes:

$$\Delta u = \frac{q}{4\eta k_B T \kappa} u_a^2 exp\left(-\frac{q|U_0|}{\eta k_B T}\right). \quad (4.2.21)$$

4.3 Asymmetry Enhancement

An effect that is not accounted for in the plasmonic detection theory outlined above, but is observed in this work, is a varied THz response with different sizes of source regions (referred to as extended source regions in this work). Detector response for various devices with multiple extended source regions can be seen in figure 4.1. The plasmonic detection theory only accounts for detection within the channel. The effect observed from the highest responding FET to the lowest responding FET in this series of devices is about a factor of seven. This detector response enhancement effect is believed to be due to two factors. One factor is a change in resistance of the source region enhancing the density of electrons resulting in forming a high-pass filter with the gate-source capacitance and the second factor is better antenna impedance matching that optimizes the absorbed THz radiation in the antenna. Each of these factors affect the effective voltages on the gate and source regions for the theory in section 4.2. See figure 4.2 for a more comprehensive equivalent circuit for a MOSFET to understand the change. Figure 4.3 shows a cross section of a FET with the bow-tie antenna couple to the source and gate.

In the subthreshold regime, the electric field in the source affects the electron density distribution exponentially. With the field applied by the THz signal absorbed by the antenna, charge will begin to accumulate at the source-channel boundary. In the subthreshold regime,

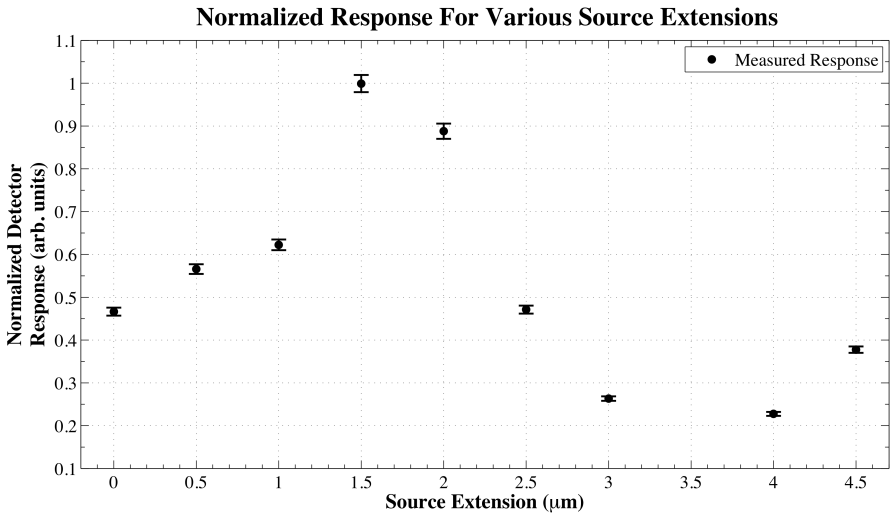

Figure 4.1: Normalized voltage response of the GEN4 source extension series FETs plotted against the source extension.

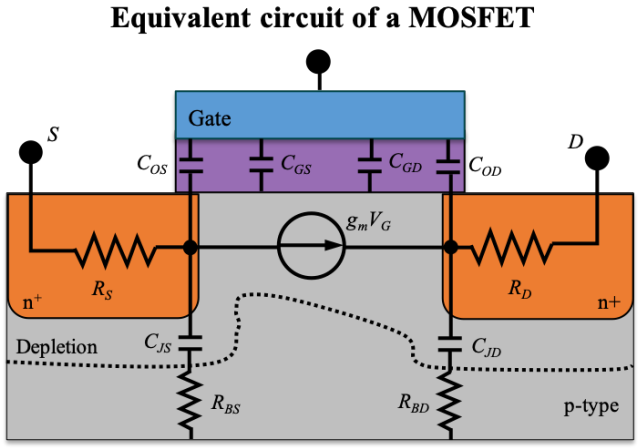

Figure 4.2: Illustration of the equivalent circuit of a MOSFET. Adapted from (Streetman and Banerjee, 2006)

there is a potential barrier in the channel that some electrons are able to overcome and diffuse across to the drain (Hassanalieragh, 2019). The more THz absorbed by the antenna, the more charge accumulates. Due to this accumulation of charge, the barrier is lowered more at this boundary allowing more electrons to diffuse across the channel and turning the FET on more (Hassanalieragh, 2019). This effect has been coined as THz-Induced Barrier Lowering (TIBL) detection by Hassanalieragh (2019).

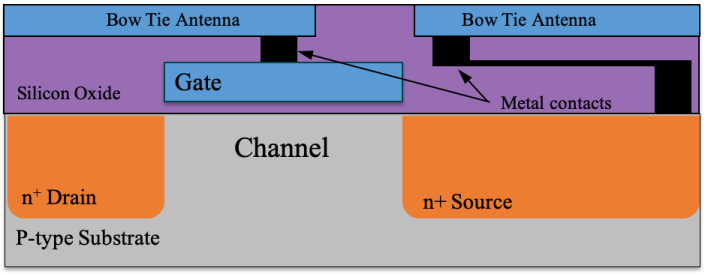

Figure 4.3: Illustration of the cross section of a FET with a bow-tie antenna coupled to it.

The theory can be explained by examining the source region simply. Take block of n-type silicon (the size of the source region) in a dielectric medium. The dielectric medium represents where the depletion region has been formed but the channel has yet to be formed yet (like in the subthreshold regime). Assume a time-varying electric field exists (the THz radiation), $E_x(t)$, in the dielectric medium. To calculate the electron density, we look at the drift-diffusion equation and solve for n:

$$J_n = qn_{(x,t)}\mu E_x(t) + qD_e\frac{dn_{(x,t)}}{dx} \tag{4.3.22}$$

where q is electron charge, μ is electron mobility, D_e is the diffusion constant, and J_n is the electron current density.

We can say that the total current entering and leaving the silicon block is zero because of the dielectric medium so we can set J_n to zero. Utilizing the Einstein relation of $\frac{D_e}{\mu} = \frac{kT}{q}$ and rearranging equation 4.3.22 we get

$$0 = \frac{E_x(t)q}{kT} + \frac{1}{n_{(x,t)}}\frac{dn_{(x,t)}}{dx}. \tag{4.3.23}$$

To find n, equation 4.3.23 can be solved via separation of variables.

$$-\frac{q}{kT}\int_0^{l_s} E_x(t)dx = \int_{n_0}^{n_{(l_s,t)}} \frac{dn_{(x,t)}}{n_{(x,t)}}, \tag{4.3.24}$$

where n_0 is the original electron density in equilibrium within the block and l_s is the length

of the block (the source length). This becomes

$$\frac{q}{kT}(\phi_s(t) - \phi_0(t)) = ln\left(\frac{n_{(l_s,t)}}{n_0}\right). \tag{4.3.25}$$

Solving for $n_{(l_s,t)}$, we get

$$n_{(l_s,t)} = n_0 exp\left(\frac{q}{kT}\phi_s(t) - \phi_0(t)\right). \tag{4.3.26}$$

This equation leads to the density of electrons at the edge of the block (source-channel boundary). The source is grounded (at $x = 0$ where the contact is) and $\phi_s(t) = \phi_E cos(\omega t)$. The density of electrons at the boundary will swing from $n_0 mexp\big(-\frac{q}{kT}\phi_s(t)\big)$ to $n_0 mexp\big(+\frac{q}{kT}\phi_s(t)\big)$ where $m = exp\big(-\frac{q}{kT}\phi_0(t)\big)$. From this, the average electron density over time increases compared to the equilibrium:

$$< n_{(l_s,t)} > |_T = n_0 m cosh\left(\frac{q}{kT}\phi_E\right). \tag{4.3.27}$$

This build up of charge at the boundary lowers the effective potential barrier enabling more electrons to jump the barrier and diffuse into the channel. This follows an increase of current from the subthreshold diffusion current equation, enhancing the amount of electrons available in the channel. This increase of current is directly related to the THz-induced charge accumulation at the source-channel boundary from the antenna.

4.3.1 Frequency Response

The way the two antenna ends are connected—one to the source and the other to the gate—creates a circuit. This can be seen in Figure 4.4. The extended source creates a resistance, R_S, and in combination with the capacitance between the gate and source, C_{GS}, creates essentially a high pass filter circuit. This means that the devices will only be able to respond to certain frequencies depending on the device parameters. For frequencies higher than the cutoff frequency of the RC circuit, the TIBL effect will result in the charge accumulation phenomenon.

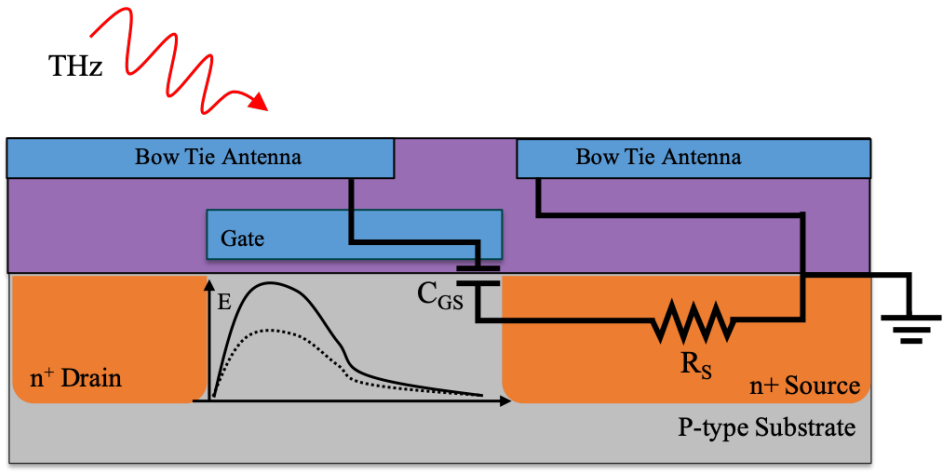

Figure 4.4: Illustration of the RC high pass filter circuit created through the extended source region and the antennas. The energy diagram illustration in the channel represents the potential barrier in the subthreshold regime prior to THz signal (solid) and after (dotted). Adapted from Fertig (2014).

Based on the information given by the foundry for the T5 FET, $R_S \approx 77\Omega$ and $C_{GS} \approx 10fF$. We can then estimate the approximate cutoff frequency of the circuit:

$$f_c \approx \frac{1}{2\pi R_S C_{GS}} = \frac{1}{2\pi(77)(10 \times 10^{-15})}, \tag{4.3.28}$$

With these values, frequencies above approximately 200 GHz will be detected for this antenna and FET parameters. The values given by the foundry are very general, do not account for manufacturing variation, and are not measured directly for each device. It is likely that the resistance and/or capacitance are slightly more than the quoted 77Ω and $10fF$ respectively because the devices are clearly able to detect some frequencies just below 200 GHz (specifically 188 GHz from the original source used in this work). With that in mind, the 188 GHz source is clearly on the lower end of what these devices could be sensitive to. This cutoff frequency is sensitive to both the resistance of the source region and gate-source capacitance which can be changed with different dimensions.

Chapter 5

Device Characterizations for Astrophysical Missions

5.1 Pixel Optimization

In addition to observing the source extension effect on response, the different variations in antenna and FET designs were tested with the same illumination source to systematically find the most optimized design. As discussed in Chapter 3, the GEN2 and GEN4 chips had many different detector designs for this experiment. The results of each of these will be grouped by relevant characteristics in this section for ease of comparisons.

5.1.1 Varied Antennas

Out of the antenna variation series of FETs, the bow-tie antennas gave the greatest responses. Some of this may be due to antenna impedance matching with the extended source region. The best bow-tie antenna FET was over 2.5 times more responsive than the best responding dipole antenna out of these devices (Figures 5.2 and 5.3).

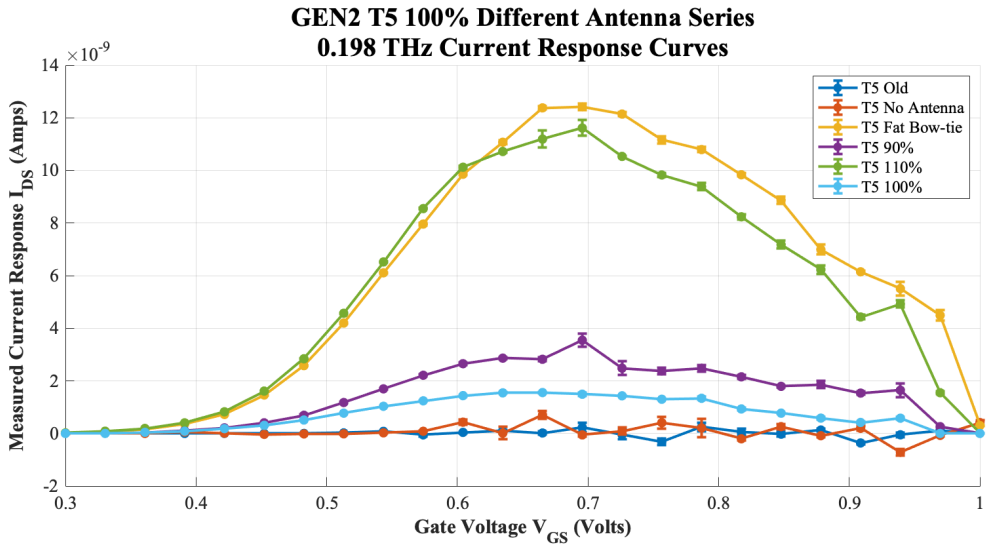

Figure 5.1: Current response, I_{DS} (Amps) versus gate voltage, V_{GS} (Volts) to single frequency of the GEN2 different antenna series devices.

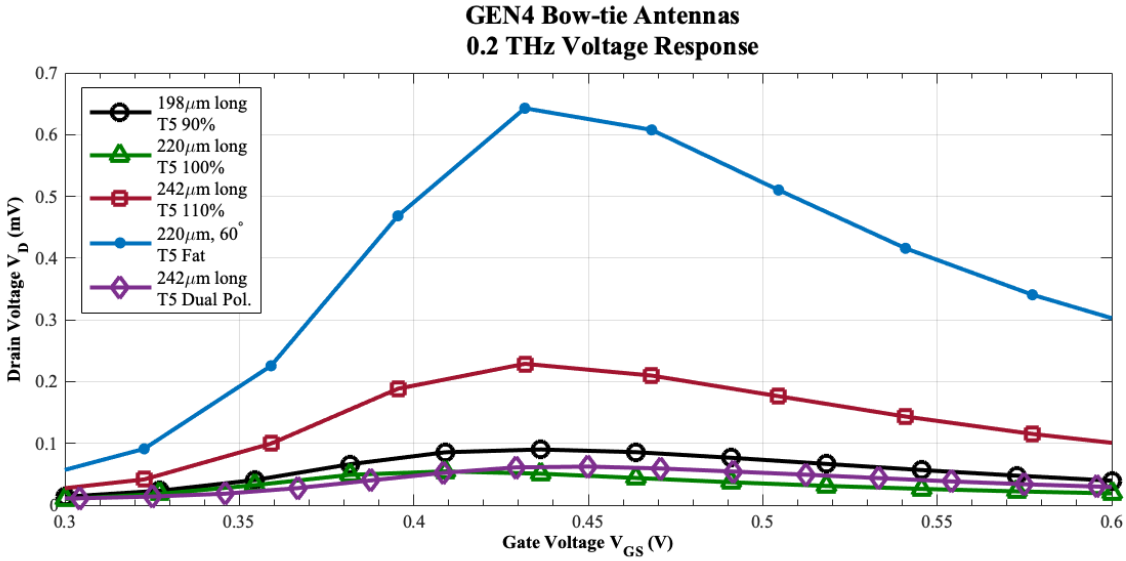

Figure 5.2: Voltage response, V_{DS} (Volts) versus gate voltage, V_{GS} (Volts) to single frequency of the GEN4 different bow-tie antenna series.

5.1.2 Source Extension Series

In the GEN2 chip there was only T5 through T7 (2.0 μm to 3 μm source extension) FETs, out of these T6 yielded the highest response, which suggested there was an optimal extension. Due to this result, GEN4 included an entire series from symmetric FET with no extension

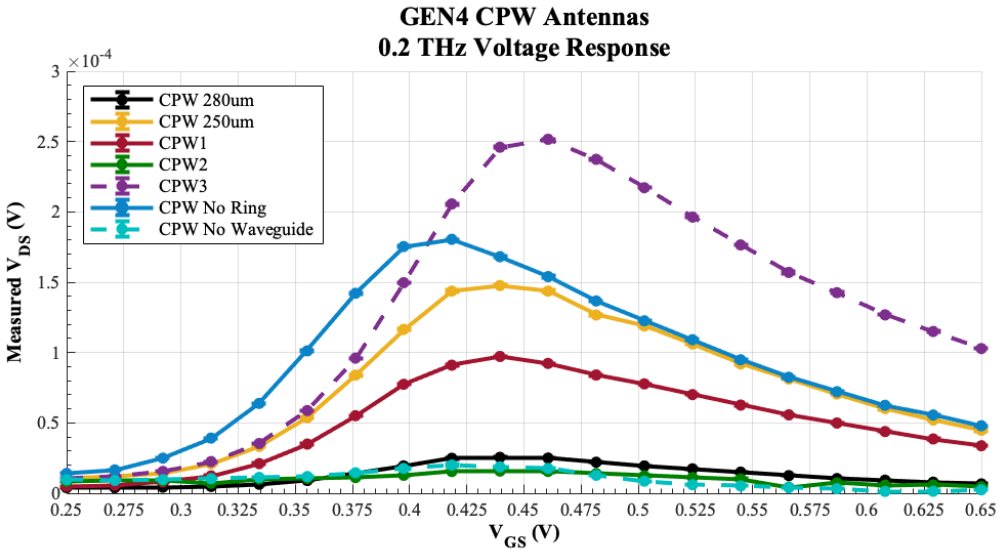

Figure 5.3: Voltage response, V_{DS} (Volts) versus gate voltage, V_{GS} (Volts) to single frequency of the GEN4 different dipole antenna series named co-planar waveguide (CPW). Both antenna petals were fabricated in the same metal layer.

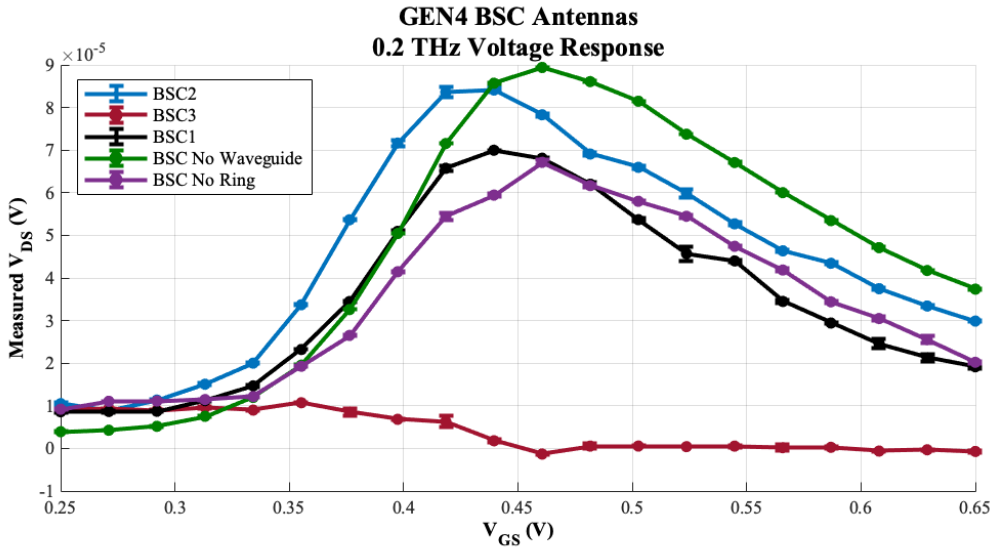

Figure 5.4: Voltage response, V_{DS} (Volts) versus gate voltage, V_{GS} (Volts) to single frequency of the GEN4 different dipole antenna series named broad side connection (BSC). One antenna petal was fabricated in the one metal layer and the second in another, this was in an attempt to see if this changed impedance matching.

(T1) all the way to 4.5 μm (T10). It is important to note however that this series all utilized the 110% antenna. The reason to note this is because that a different antenna results in

a slightly different impedance which would have to be matched. This changes which source extension is the best for impedance matching therefore changing the most optimized extension with most optimized antenna. This is the case for this series exploration. This is why in the GEN2 devices, the longer source extension device (T6) resulted in a better response whereas in GEN4 a shorter source extension device (T4) resulted in a bigger response. The larger antenna in GEN4 (using the 110% antenna) needed less resistance within the source region to match the lower impedance for the same frequency.

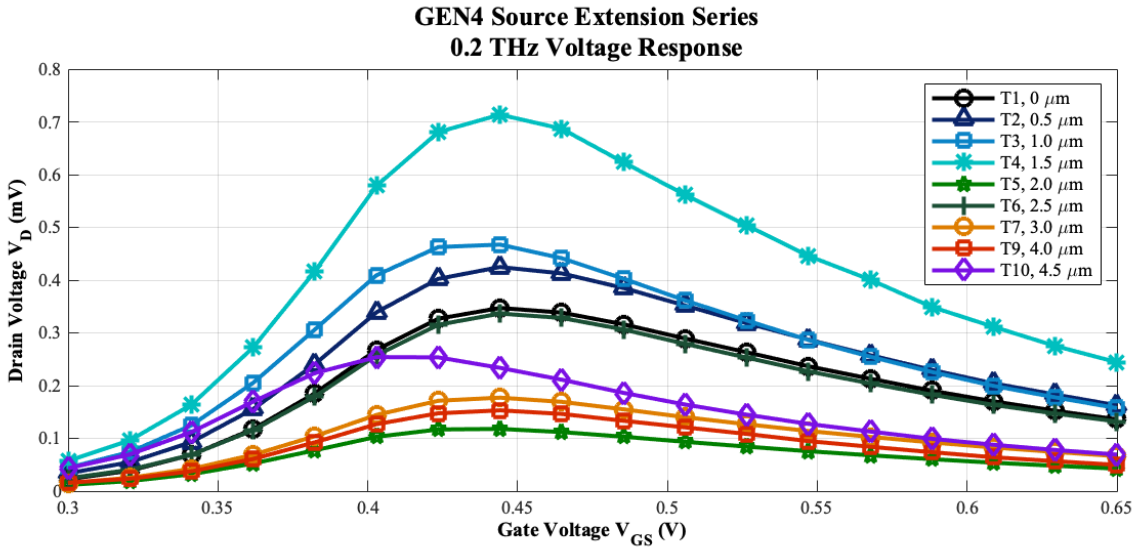

Figure 5.5: Voltage response, V_{DS} (Volts) versus gate voltage, V_{GS} (Volts) to single frequency of the GEN4 source extension series.

5.1.3 Frequency Response

Using the tunable source from VDI, the small scale frequency response (0.17 to 0.25 THz) was obtained for the T5 110% pixel to determine the operational bandwidth of the devices.

Fitting a Gaussian to each of the curves to find an approximate bandwidth, we find that T5 110% device has a bandwidth of about 6.1 GHz. T5 Fat Bow-tie yields a bandwidth of about 6.7 GHz. A larger bandwidth for T5 Fat Bow-tie was expected. The bandwidth of 6.1 GHz will be used for calculations of power falling on the detector calculation for astronomical application in later chapters.

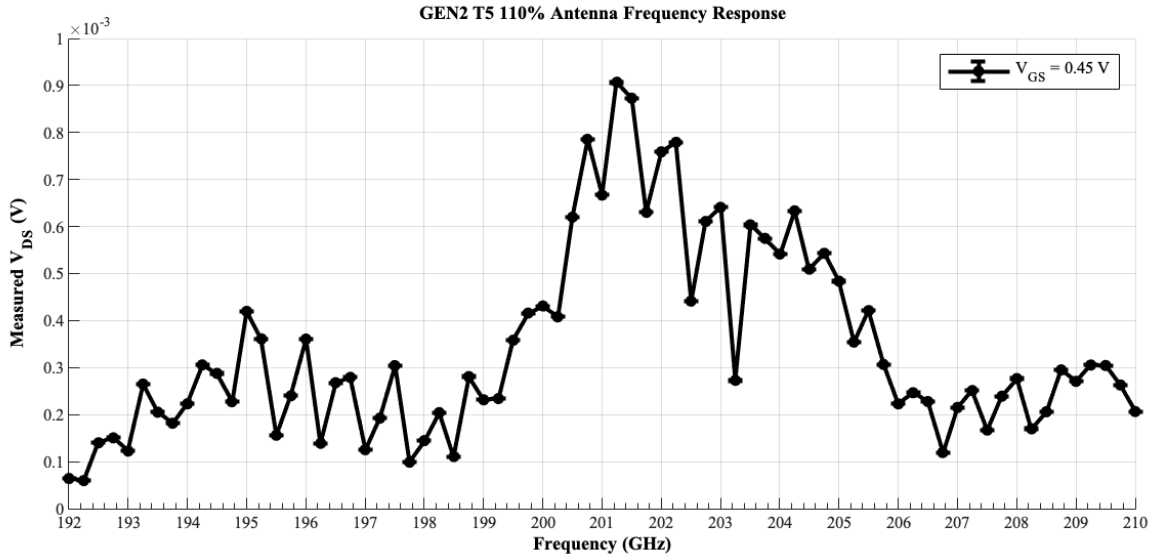

Figure 5.6: Voltage response, V_{DS} (Volts) versus frequency for T5 110 % FET.

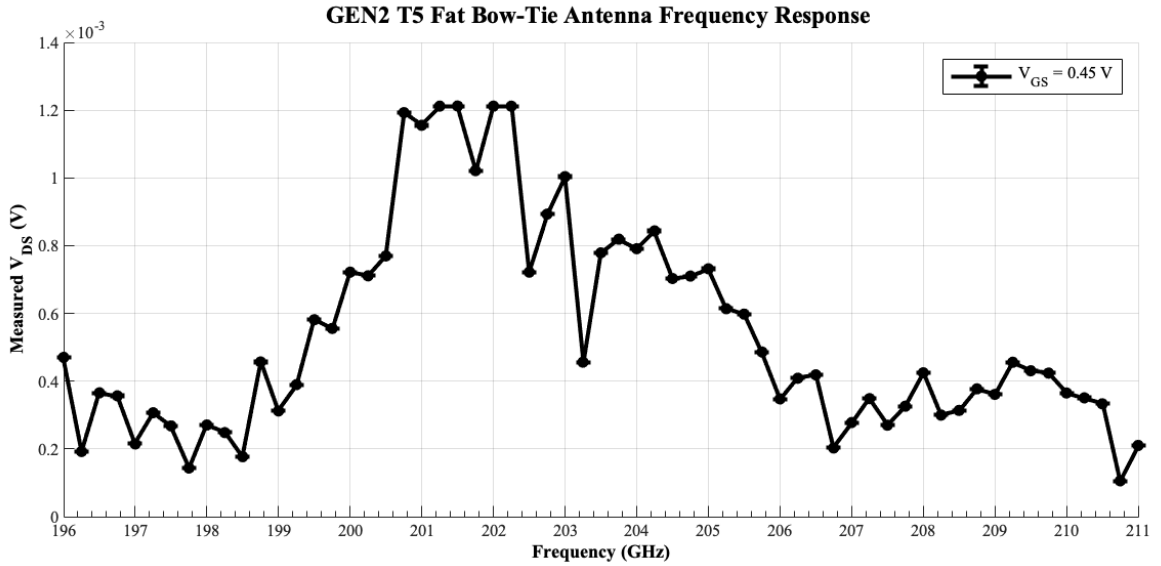

Figure 5.7: Voltage response, V_{DS} (Volts) versus frequency for T5 Fat Bow-tie FET.

5.2 Responsivity

Understanding the detector response with respect to how much power is falling on the device is important in determining whether or not a detection can be made. The metric that is used for this is called responsivity. Responsivity is the ratio of the detector response (e.g. voltage or

current) to the power incident on the detector. The larger this number, the better the response the detector is. Understanding the responsivity is one important metric in determining if these devices will be useful for a planetary remote sensing mission.

Due to the lack of standardization and calibration for THz detectors and sources, this measurement is extremely difficult. Many groups try to estimate the power that is falling on the detector and do not make a direct measurement. In order to counteract this issue and get a direct measurement, we used the PM5 discussed in Section 3.5.2. A comprehensive study of FET response with incident power has not been explored in other works. The PM5 has been calibrated by VDI. The PM5 was mounted to a plate along with the dewar housing the device under test (DUT). The plate was then placed onto XYZ stages. Precise measurements between the input of the PM5 and the DUT were made so that each response was measured from the DUT, the PM5 could be translated into the same position that the DUT was to measure the actual power at that time. In addition to the PM5, a wire grid polarizer was designed to reduce the amount of power falling on the detectors by a known amount.

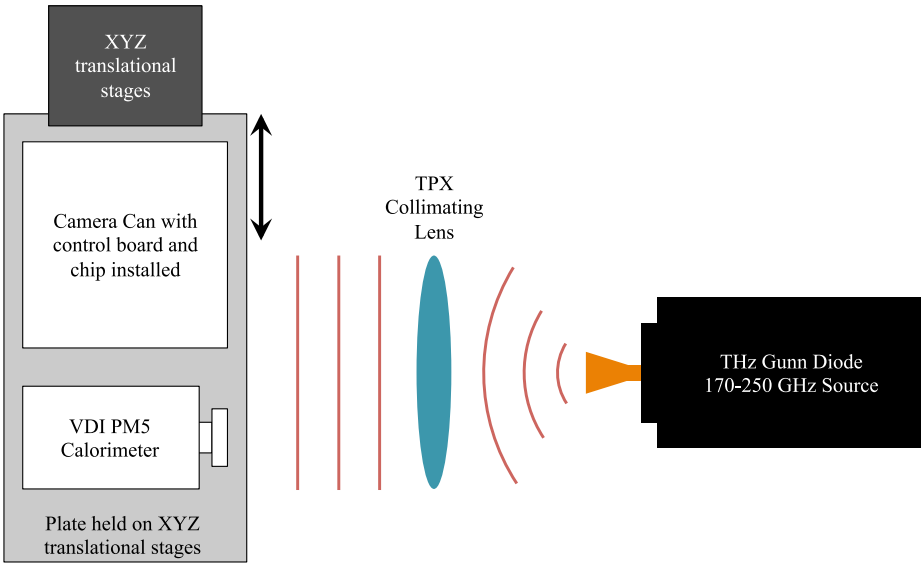

Figure 5.8: Block diagram of the dewar and PM5 setup.

These devices are run in the subthreshold and the subthreshold regime is nonlinear as discussed in section 2. It follows that the detector response will be nonlinear with incident

power. Understanding this relation is important to estimate the output voltage from a known astronomical source power. A polymethylpentene (TPX) lens was used to collimate the Gaussian beam from the THz source for these experiments. Collimation of the beam ensures that the radiation illuminates the DUT uniformly and that it is well coupled down the waveguide to the PM5.

5.2.1 GEN2 and GEN4 Responsivities

The nonlinearity with incident power effect was first observed in the GEN2 and GEN4 devices which can be seen in the log-log plot in figure 5.9. Originally the GEN2 devices were being run in the current mode configuration. This was changed in the GEN4 devices which were mainly run the voltage mode configuration. The same trend of nonlinearity can be seen in both modes.

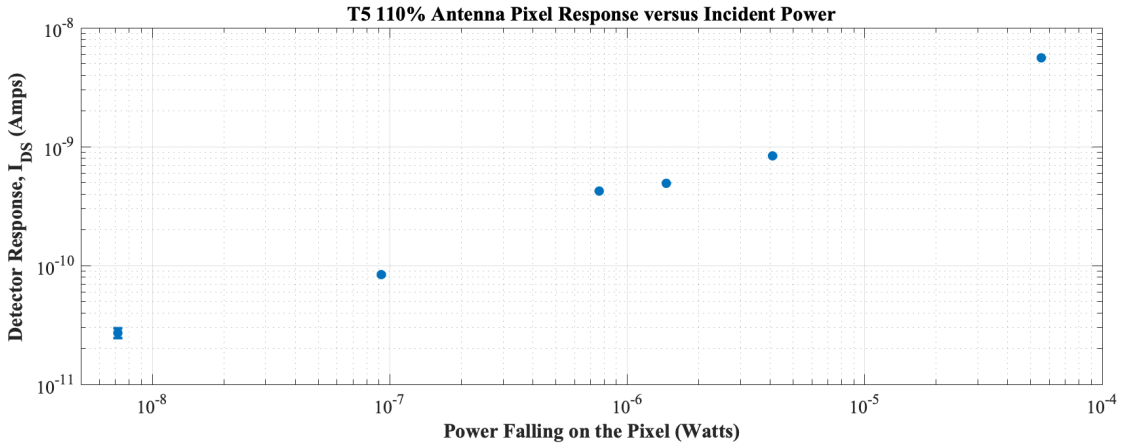

Figure 5.9: Current response (amps) versus incident power falling on the pixel area (watts).

For both generations, the noise at the sampling frequency of the lock-in amplifier was determined utilizing the spectrum analyzer. This allowed for NEP values to be measured and calculated via the following relation:

$$NEP_{current} = \frac{I_{noise}}{R}\left[\frac{Watt}{\sqrt{Hz}}\right] \tag{5.2.1}$$

Responsivities & NEPs at Various V_{GS}					
V_{GS} (V)	I_{DS} (A)	∂I_{DS} (A)	Responsivity (μA/W)	∂R (μA/W)	NEP (nW/$\sqrt{Hz}$)
0.25	2.79×10^{-11}	$\pm 1.70 \times 10^{-14}$	4.36	$\pm$85.3	7.27
0.35	4.01×10^{-10}	$\pm 2.64 \times 10^{-13}$	62.50	$\pm$85.3	2.68
0.40	1.35×10^{-9}	$\pm 2.34 \times 10^{-13}$	211.00	$\pm$85.3	8.34
0.47	6.11×10^{-9}	$\pm 3.09 \times 10^{-12}$	953.00	$\pm$85.3	6.10
0.55	1.86×10^{-8}	$\pm 9.76 \times 10^{-12}$	2910.00	$\pm$85.3	2.77
0.64	2.91×10^{-8}	$\pm 1.04 \times 10^{-10}$	4550.00	$\pm$85.3	7.89

Table 5.1: List of measured responsivities and NEPs for GEN2 T5 110% device (V_T=0.65 V) at various V_{GS}values for current mode detection.

Gate Voltage, V_{GS} (V)	Responsivity (V/W)	NEP (nW/Hz$^{1/2}$)
0.36	336	0.795
0.44	880	0.645
0.5	693	1.580
0.56	492	3.740
0.65	302	5.830

Table 5.2: List of measured responsivities and NEPs for GEN4 T4 device at various V_{GS} values for voltage mode detection.

$$NEP_{voltage} = \frac{V_{noise}}{R}\left[\frac{Watt}{\sqrt{Hz}}\right] \tag{5.2.2}$$

The GEN4 T4 device showed a marked improvement for NEP values in comparison to the GEN2 devices by a factor of 10 for some values. This is likely due better impedance matching with the antenna and source region.

5.2.2 65 nm Responsivities

The nonlinearity relation was verified in the 65 nm chips as well. The responsivity (V/W) versus incident power was plotted to observe if the signal went decreased at a faster or slower rate than the incident power. The responsivity of the device actually increases with lower incident powers (Figure 5.10) by almost an order of magnitude. This trend holds with all of the other devices tested in this work as well. This is an important result for determination of the devices because at lower incident powers, the responsivity of the FETs is higher which

Power, mW	Responsivity (V/W)	NEP ($nW/Hz^{1/2}$)
0.27	360	2.56
0.21	302	3.05
0.16	430	2.14
0.12	390	2.36
0.064	686	1.34
0.022	1413	0.65

Table 5.3: List of measured responsivities and NEPs for the 65 nm T4 device at various incident powers for voltage mode detection.

means it will detect more low-power sources than with the assumption of a linear response with power.

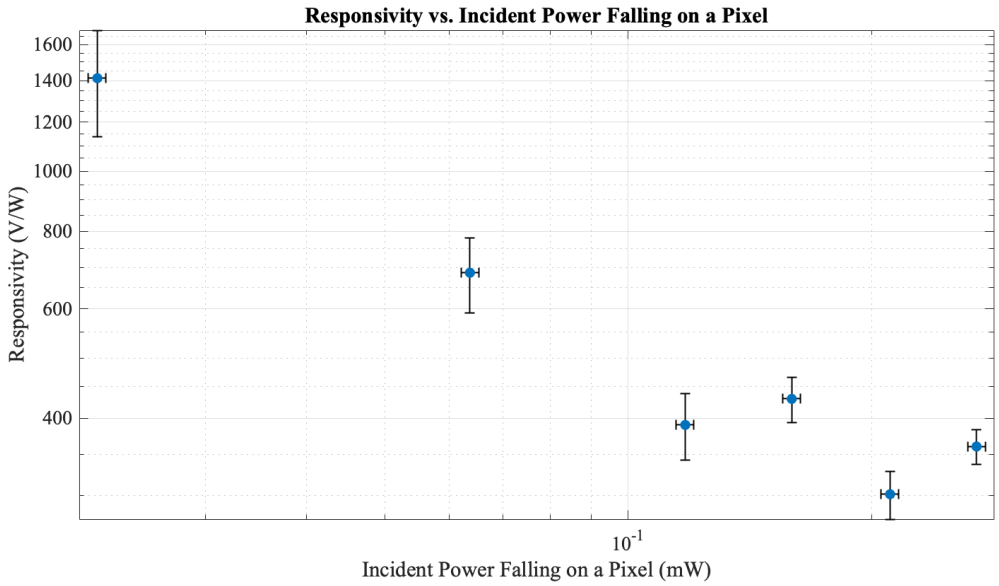

Figure 5.10: Responsivity (V/W) of the 65 nm T4 device versus incident power (W). Power values are shown with a 5% error.

5.2.3 10x10 Imaging Array Responsivities Per Pixel

This nonlinear power relation could be more closely studied using the 10x10 imaging array because it consisted of 100 of the same pixel design. It is important to note that these devices were fabricated using the 350 nm CMOS process which produces more manufacturing variation and more noise than smaller feature sized processes. A certain percentage of these

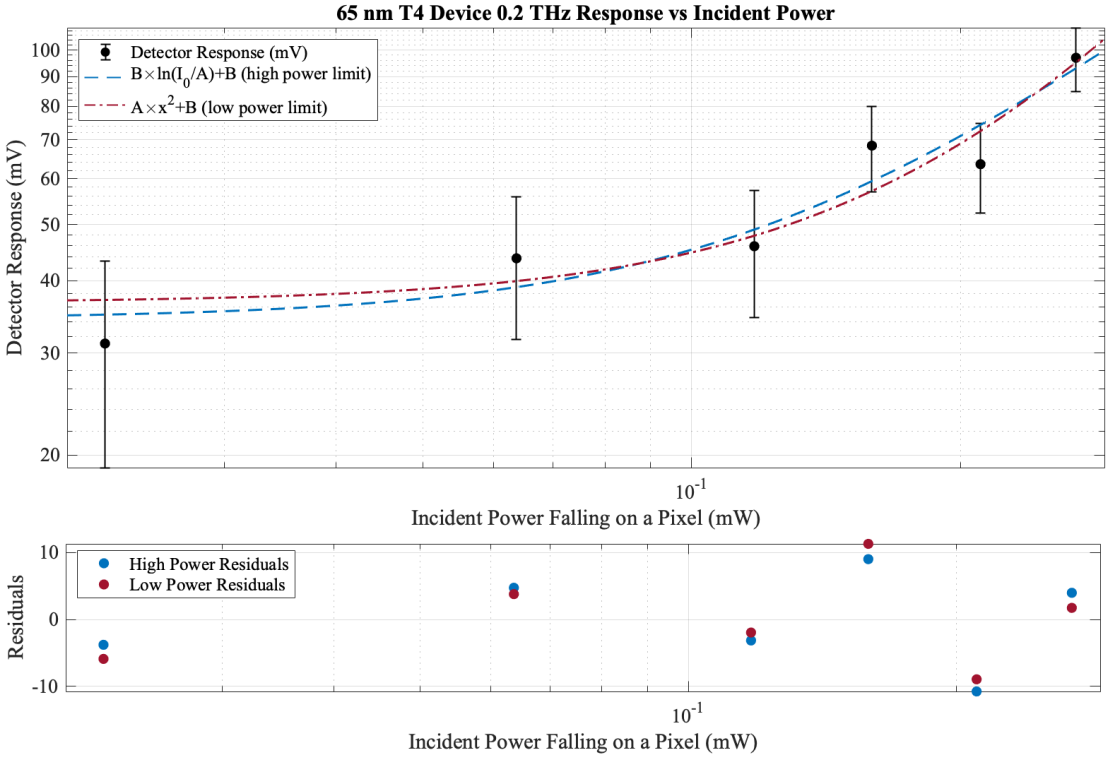

Figure 5.11: 65 nm chip T4 response (millivolts) versus incident power falling on the pixel area (milliwatts). Both the high power limit and low power limit equations were fit and the residuals between each fit and the data points.

devices are expected to produce responses that are off compared to the majority due to the larger manufacturing variation in 350 nm CMOS process.

A new way of running an array was implemented in hopes of counteracting the pixel-to-pixel variation which was expected to be large in the 350 nm technology. Each pixel would have its own V_{GS} value set in order to equalize the drain voltage out of each pixel while under dark conditions. The pixels all also had 0.2 μA biasing conditions as well similar to the work of (Fertig, 2014).

As an imaging experiment to test this, a pair of scissors and a razor blade were hidden within a cardboard box (as seen in figure 5.12) and placed on the XY motorized stages. The box was rastered to get a large portion of the box image. The scissors and razor blade can clearly be seen in 5.13, but there is still a lot of pixel-to-pixel variation resulting in a checkered

appearance from assembling the rastered frames together. This noise was not easily removable by conventional means such as using traditional background and flat frames to remove issues. The pixels respond nonlinearly with incident power which is evident in figures 5.9 and 5.11. This relation is dependent on how far into the subthreshold the pixel is being run at, in other words it depends on the gate voltage. It was not possible to change the gate voltages dynamically in this new configuration.

Figure 5.12: Image of the scissors and razor blade targets suspended inside the cardboard box.

In order to get a cleaner image for this demonstration, the 10x10 pixels were split up into 4 super-pixels where the response from each quadrant were averaged together. This method was able to achieve a clearer image as shown in figure 5.14.

Since the pixels were behaving nonlinearly with incident power, one possibility of fixing this noise was to characterize the pixel output with different incident powers and fit a curve to each pixel. With a relation to each pixel, one could possibly take one pixel in each frame as a reference and correct the rest of the pixels. This correction method was not tested due difficulty of changing the gate voltages and imaging capabilities were not the primary focus. These devices have already been demonstrated to be able to image with the correct conditions using a single pixel raster scan.

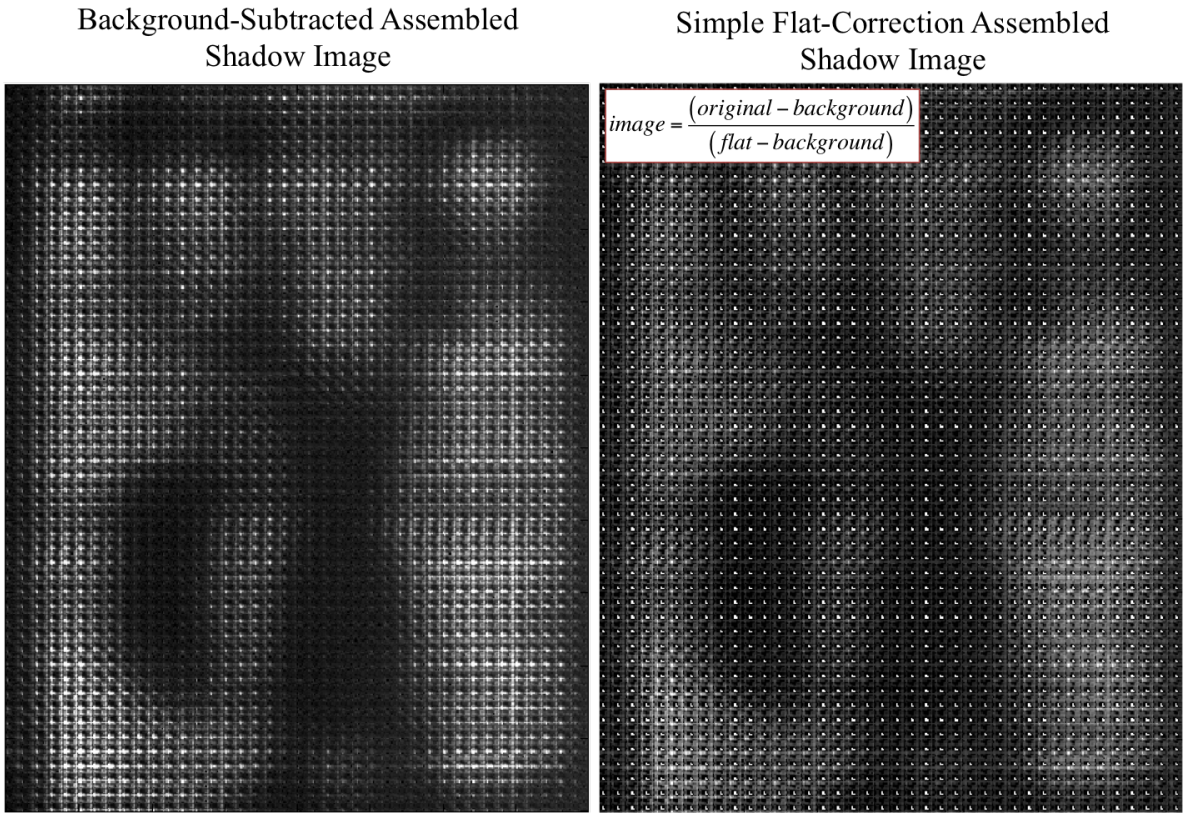

Figure 5.13: The resulting THz images when applying a background correction (left) and applying a background with flat correction (right). Neither method gets rid of the checkered pattern. This effect is due to the nonlinearity with respect to incident power and the lack of control of V_{GS}. Each pixel's response needs to be fully characterized to remove the pixelation.

An attempt to fit the pixels with a similar relation to the 65nm device was attempted, however due to the different V_{GS} and threshold values pixel-to-pixel, the responses of each pixel varied more extremely. This was due to a combination of manufacturing variation affecting the threshold voltage and how far into the subthreshold or threshold regime each pixel was. Determining the best way to set the V_{GS} values and fit the pixels to a response-power relation to discontinue this pixel-to-pixel response variation was left to future work.

Examples of the pixel variations are shown in figures 5.15 through 5.19. The quadratic relation was attempted to be fit, here but the variation of the the fit constants were so varied that the results were not real as ideality factor would not vary that much and change the fit. This effect is believed to be the devices being in different regimes (i.e., subthreshold, above

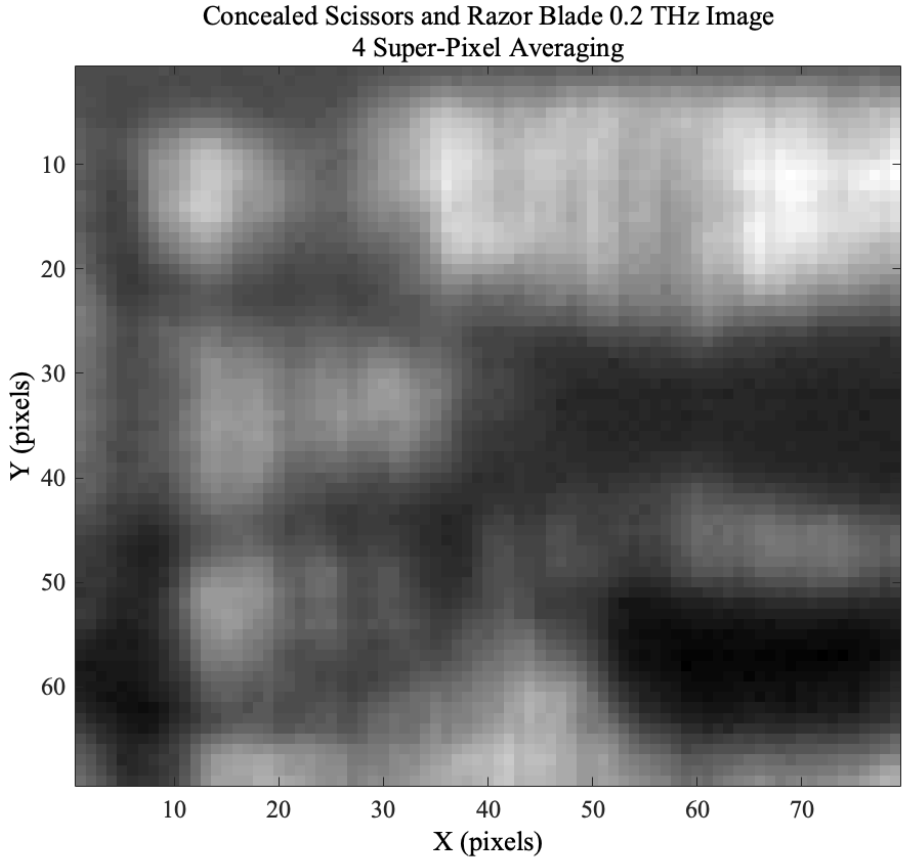

Figure 5.14: Resulting THz image of the concealed scissors and razor blade when averaging pixels into 4 super pixels (25 pixels averaged per super pixel). Vertical striping and variation in the box is due to the corrugation of the box.

threshold, at threshold). A subset of the 100 pixels with the fits can be seen in Figures 5.15, 5.16, 5.17, 5.18, and 5.19. Some devices were very well fit by this relation like columns 10 and 7, but others were completely unreal like columns 1 and 3.

5.3 Noise Characterization

5.3.1 Noise Equivalent Power (NEP) Characterization

Noise equivalent power (NEP) is an important quantity when characterizing a detector. NEP is essentially the amount of power incident on the detector that is required to give an output signal that is equal to the noise, in other words, the amount of incident power to achieve

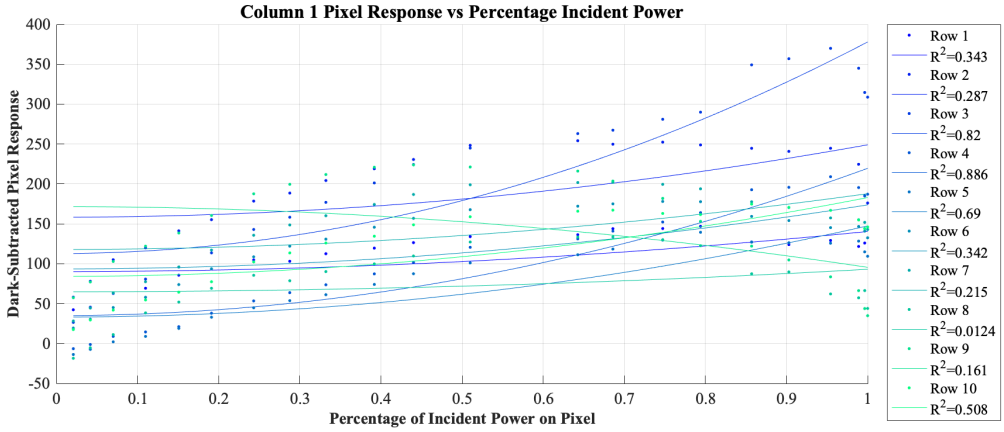

Figure 5.15: First column in the 10x10 array detector response versus percentage of incident power plotted with a quadratic fit attempt $A \times X^2 + B$.

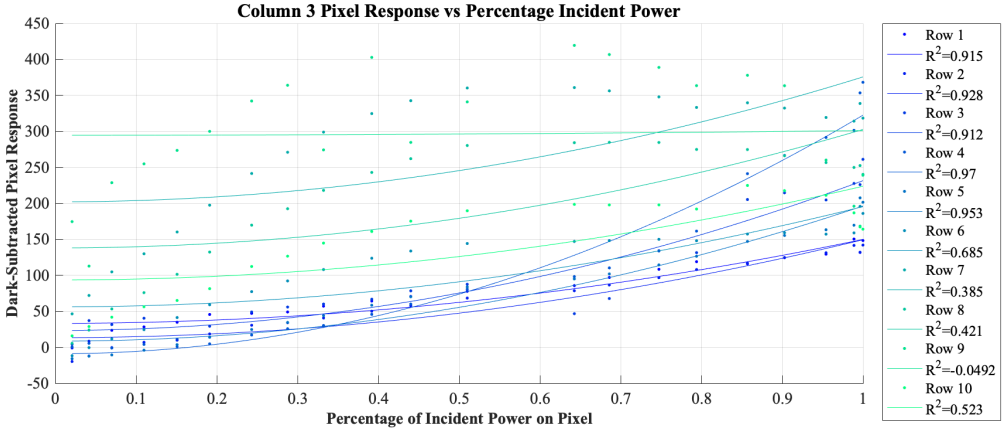

Figure 5.16: Third column in the 10x10 array detector response versus percentage of incident power plotted with a quadratic fit attempt $A \times X^2 + B$.

a signal-to-noise ratio (SNR) of 1. NEP is expressed in the units $Watts/\sqrt{Hz}$ (the power required within a 1 Hz bandwidth).

Some cooled detectors are able to reach much lower NEP. Cooled bolometers for astronomical devices currently have the best NEPs up to 0.4×10^{-19} to 3×10^{-19} $W/\sqrt{Hz}$ with KIDs quickly catching up with NEPs of $10^{-18} - 10^{-19}$ (Farrah et al., 2019; Rogalski, 2011). Cooling the bolometers results in a longer response times (Rogalski, 2011), but KIDs have greatly improved response times compared with traditional cooled bolometers (Farrah et al., 2019). The Cosmic Background Explorer (COBE) instrument Far-Infrared Absolute Spec-

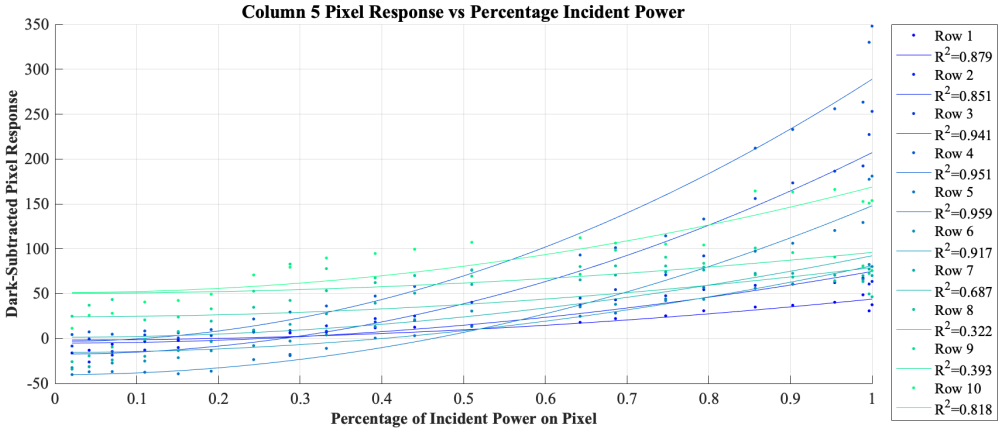

Figure 5.17: Fifth column in the 10x10 array detector response versus percentage of incident power plotted with a quadratic fit attempt $A \times X^2 + B$.

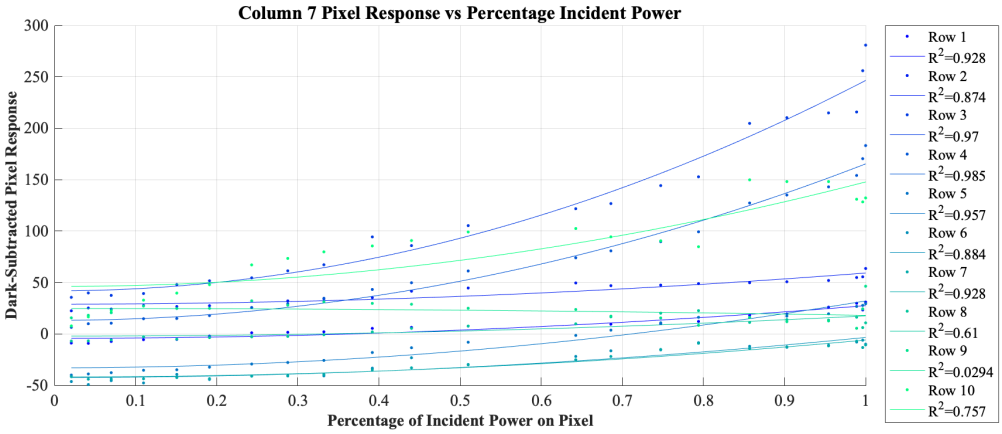

Figure 5.18: Seventh column in the 10x10 array detector response versus percentage of incident power plotted with a quadratic fit attempt $A \times X^2 + B$.

trophotometer (FIRAS) instrument used bolometers (Rogalski, 2011). Hershel Space Observatory also utilized bolometers in a 326-pixel array in its Spectral and Photometric Imaging Receiver (SPIRE) (Rogalski, 2011). Bolometers (and most of these technologies) are often implemented in smaller scale arrays due to isolation and readout limitations. This makes the low NEPs extremely important but larger fields of view are more difficult to obtain. With larger focal plane arrays (FPA), a detector could gather a larger spot on the sky (Rogalski, 2011).

Comparing these devices to uncooled detectors is a fairer comparison than cooled detectors.

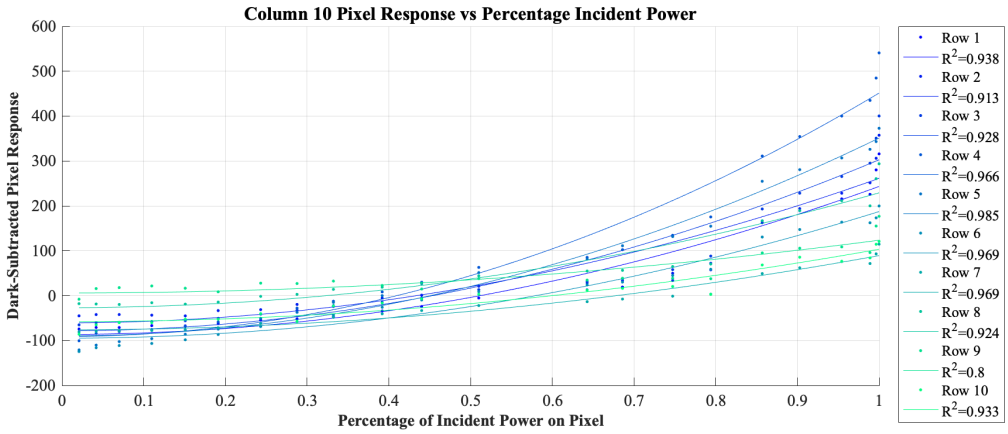

Figure 5.19: Tenth column in the 10x10 array detector response versus percentage of incident power plotted with a quadratic fit attempt $A \times X^2 + B$.

The devices fabricated for this work are not as good as some uncooled single element detectors today (table 1.4) with responsivities of 0.3 to 1.4 kV/W and NEPs of 645 to 5800 pW/(Hz)1/2. It is important to keep in mind that because the responsivity for the devices changes with the power falling on the detector as shown in table 5.3. A true comparison would require knowing the power falling on each of the detectors in table 1.4. Using the data from the studies presented here, a more optimized device could compete with the devices in table 1.4. These optimization recommendations will be discussed in section 6.2.

In order to calculate the NEP of the devices in the system, a noise spectrum was observed at for various VGS using an Agilent HP Signal Analyzer (see Figure 4.6 for the various noise spectra). Flicker noise (or 1/f) can clearly be seen in the spectra (figures 5.21 and 5.20).Flicker noise can be seen in most physical systems and electronic devices. There are multiple models for semiconductor electronic devices (like MOSFETs) including the McWhorter model and the Hooge model (Dutta and Horn, 1981; Hooge, 1994; Lundberg, 2002). The McWhorter model asserts that flicker noise is due to surface effects and the Hooge model asserts that it is due to electron mobility fluctuations.

In either model, it is clear flicker noise is inherent within the device itself and can be improved by using different processes, cleaner foundries, et cetera to minimize nonuniform distributions in materials (Dutta and Horn, 1981; Hooge, 1994; Lundberg, 2002). Flicker

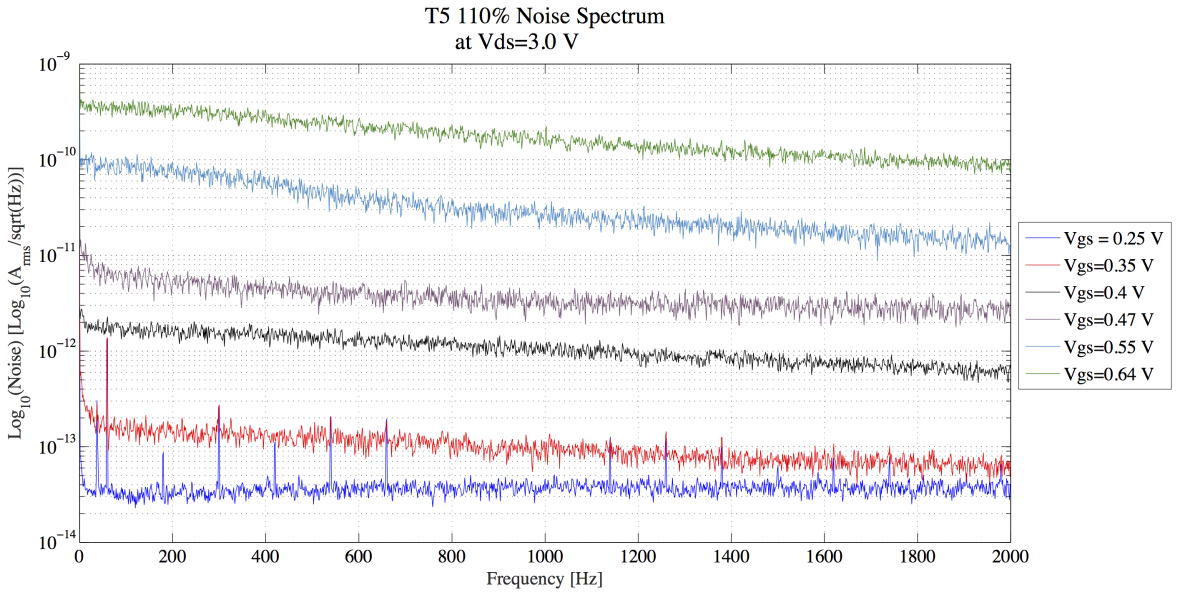

Figure 5.20: Noise spectrum $[Log_{10}(A_{rms}/\sqrt{Hz})]$ taken using the Agilent Signal Analyzer for T5 110% with V_{DS}=3.0 V at various V_{GS} values.

noise is called 1/f because of its relationship with frequency. It follows the relationship:

$$S = \frac{A^2}{f^\alpha} \tag{5.3.3}$$

where S is the power spectral density (in Amps2/Hz), A is a constant, and α is between 0.9 and 1.1. Fitting to the noise spectrum to a GEN2 T5 110% device for $V_{GS} = 0.55V$ in Figure 4.6, $\alpha = 1.1$ and $A = 1.269 \times 10^{-9}$ (Dutta and Horn, 1981). Normally, observing noise spectra at higher frequencies, the corner frequency (the frequency where flicker noise no longer dominates) can be found and Johnson noise can be estimated at higher frequencies. Due to bandwidth limitations from the current preamplifier, higher frequencies are attenuated and a noise spectrum cannot be obtained for those frequencies. The signal measurements were taken when the source was chopped at 170 Hz which is well within the flicker noise.

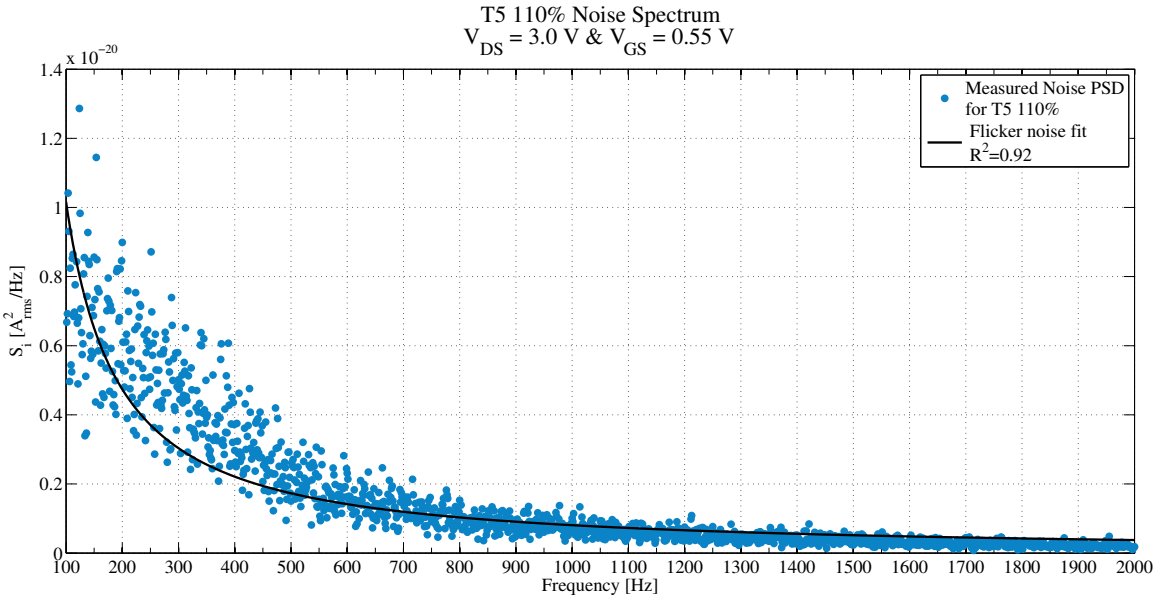

Figure 5.21: Noise spectrum from GEN2 T5 110% with a 1/f noise curve fit.

5.4 Detection Capability

In order to determine if it is possible to detect a planetary source (over the CMBR), we will propose a theoretical satellite specifications. We will take our 10x10 imaging array but the pixels will be the 65 nm T4 design since those were the best performing. This will make the detector 100 pixels (10x10) making the array about 3.5 mm by 3.5 mm. This will be deployed on a theoretical telescope which we will model after Junocam on the JUNO Spacecraft. The opening aperture will be about 15 mm with a focal length of 15 mm (f/1). We will be giving this telescope a theoretical efficiency of 80%. We will assume that, due to orbiting around the planet that the CMBR will be occluded by the planet. This is the main difference from attempting to detect a faint object from orbit of Earth, where the background is about 10^{-18} MJy/sr (Farrah et al., 2019) which makes it extremely difficult to be sensitive enough to detect faint objects.

Similar to equations 1.2.7 through 1.2.9, we will calculate the flux ($W/m^2/m/sr$) for each of the planets based off of table 1.3. Once we have that, we will calculate the power that

Planet	R_{planet} ($10^6 m$)	$D_{orbit,1}$ (km)	$D_{orbit,2}$ (km)	$D_{orbit,3}$ (km)	λ (μm)	$P_{det,1}$ (μW)	$P_{det,2}$ (μW)	$P_{det,3}$ (μW)
Venus	6.05	400	1400	2400	750	30.01	2.45	0.83
	6.05	400	1400	2400	450	193.00	15.76	5.36
Jupiter	69.911	3500	4500	5500	1744	0.94	0.57	0.38
	69.911	3500	4500	5500	1332	2.78	1.68	1.13
	69.911	3500	4500	5500	1049	6.95	4.20	2.81
	69.911	3500	4500	5500	890	14.00	8.47	5.67
	69.911	3500	4500	5500	750	25.47	15.41	10.32
Saturn	58.232	3000	4000	5000	1744	0.74	0.42	0.27
	58.232	3000	4000	5000	1049	4.91	2.76	1.77
	58.232	3000	4000	5000	609	36.48	20.52	13.13
Uranus	24.362	800	3000	10000	1250	4.34	0.31	0.03
	24.362	800	3000	10000	750	32.88	2.34	0.21
Neptune	24.622	800	3000	10000	1250	4.14	0.29	0.03
	24.622	800	3000	10000	750	42.67	3.03	0.27

Table 5.4: Power falling on a pixel for each brightness temperature value in table 1.3. Closest orbital distances are based on closest approach for Venus Express, JUNO, and Cassini for Venus, Jupiter, and Saturn respectively. Uranus and Neptune values are guesses based on the other planets' values. Distance 1 is the closest case, distance 2 is a medium case, and distance 3 is a far case.

would fall on the array by the following

$$P_{det} = E_\lambda A_{tele} \Delta\lambda \epsilon_{tele} \tag{5.4.4}$$

We will utilize the relation in figure 5.11 to determine if the devices will be able to detect the radiation from the planets. For these calculations, A_{tele} is 1.77×10^{-4} m^2, $\Delta\lambda$ is 45 microns (6.1 GHz), and ϵ_{tele} is the telescope optics efficiency which we are saying is about 80%. The power falling on the array at different orbital distances from each planet is tabulated in table 5.4.

Based on the values that were detected by the 65 nm T4 device in the lab, it was easily able to detect 22 μW above the noise of the devices. Many of the values calculated for each planet these devices would be able to detect. It would definitely be able to detect Venus at 450 μm at 400 km. There are a few ways to improve these devices which will be discussed in section 6.2. Another thing that would be relatively easy to do to improve the numbers and

get more signal is change the optics so there is a larger aperture. Detecting a planet from an orbit around that planet is not out of the realm of possibility for these devices.

Chapter 6

Conclusion and Discussion

6.1 Suitability for Astrophysical Missions

Instead of using expensive material like superconductive materials in TES sensors, Si-MOSFETs utilize simple Si CMOS technology that is used today. This can be implemented into many different scenarios because of it's integration into simple readout electronics. These devices can be designed into focal plane arrays and be read out like a regular camera without the need for mixing to a lower frequency. In addition to low-cost devices, many of the optics are also made of low-cost materials, like Teflon and TPX.

These devices will likely never be able to get to the low NEP requirements for a large camera pointed out into deep space and are unlikely to be sensitive enough for photometry overcoming the intense background from the CMBR (requirements can be seen in Farrah et al. (2019) figures 7 and 8). These devices may be a good candidate to develop for low-cost planetary observing missions where the CMBR is occluded by the planet or moon. While the devices cannot fill a need for a low-cost alternative for deep all-sky type missions, developing a THz camera that could be low size, weight, and power (SWAP) that could be sent to planets or moons could make THz planetary science more accessible for small missions.

6.2 Suggested Improvements for Devices

There are quite a few ways that these devices could be improved for even more responsivity and lower electronic noise. The preamp board designed for some lower noise measurements was a good first step, and the 10x10 imaging array utilized some of the on-board and on-chip amplification methods based on that success. Once a mission was planned and optics designed, this could easily be optimized more so that there is even less noise. Utilizing the 65 nm technology would be ideal because it did show the lowest noise levels out of all of the devices.

But et al. (2016) presented work where their devices had different substrate thicknesses and a thinner substrate resulted in a higher responsivity. The devices had four devices with substrate thicknesses of 55, 70, 90 and 125 μm. The average responsivity for the thickest substrate was reported as 62.6 V/W and the thinnest substrate reported an average responsivity of 696 V/W (But et al., 2016). According to But et al. (2016), a reduction of 56% in substrate thickness resulted in an eleven times increase in responsivity.

A few GEN4 devices were manually thinned by Dr. Alan Raisanen at RIT in an experiment to replicate the results of this experiment. Each unpackaged die was mounted on a piece of aluminum on a bed of Apiezon black wax face down. The original die heights were measured using a laser micrometer so that the target heights could be calculated. By utilizing different grits of silicon carbide wet metallurgical sandpaper, the dies were ground to desired thicknesses plus an extra amount. This extra amount was taken away when the devices were polished down on a polishing wheel using a 2-20 micron diamond slurry to remove the extra material and remove scratches. The dies were then removed and soaked in Xylene to remove residual wax, rinsed in deionized water and dried with dry nitrogen. The devices were about 250 μm thick and 125 μm is the target to determine what a change of thickness by half. Three devices made it through the inspection process. After packaging the devices through American Dicing Inc., one device did not run like a regular FET and was eliminated due to being nonfunctional. The other two devices were functional.

The experiment was to run the same device between the two thinned devices and an un-

thinned device with the same source power and conditions to compare devices. The responses the T5 110% devices for each chip can be seen in figure 6.1. The devices did not show the same trend as shown in But et al. (2016), but no trend was shown between the thinned and un-thinned devices. One of the thinned devices had a higher response and the other had a lower response. This is believed to be due to manufacturing variation and the thinning process variation. The process described was developed specially for these devices and was a manual process. This created variations in thickness across each individual die and could have had unforeseen effects on response being done after the entire manufacturing process.

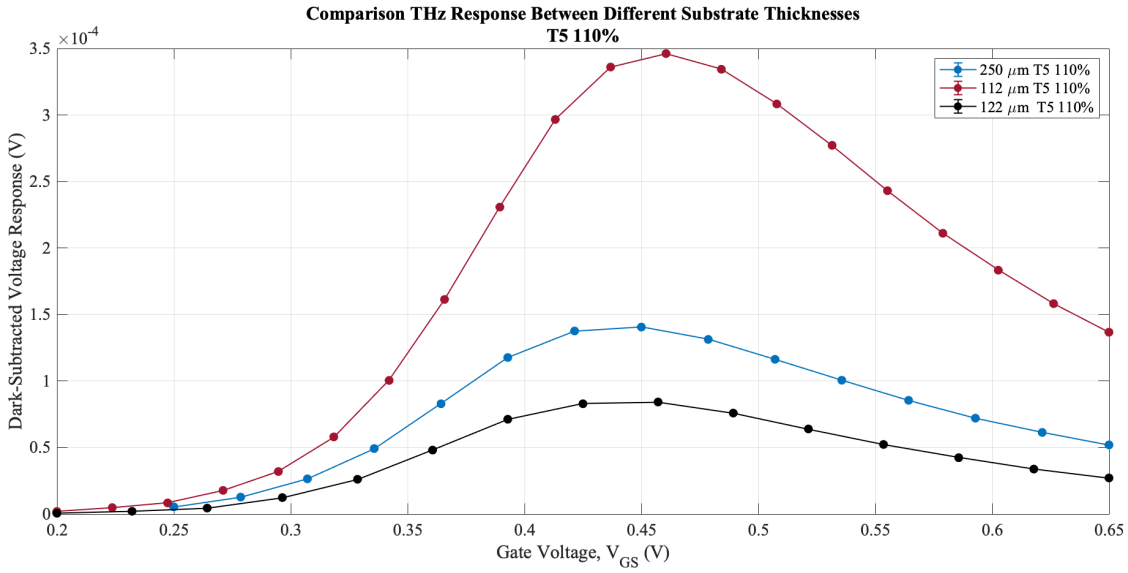

Figure 6.1: T5 110% voltage THz response for different substrate thicknesses.

The results from this experiment should not be taken as evidence against the But et al. (2016) experiment as there was too much variation and too little sample size to accurately verify the results. Should these devices be further developed for any application, the substrate thickness effect should be studied further to possibly increase responsivity by an order of magnitude (and decrease NEP).

Other optimizations for the technology would include utilizing smaller process technologies like the 65 nm devices to reduce noise, including on-chip amplification to read out the device without adding much more noise, and tuning the source regions to the antennas depending on

the target frequencies. Each of these could improve responsivities by a factor of 5 to 10 like the source region matching or reducing noise like 1/f noise in the smaller process technologies.

6.3 Discussion

Si-MOSFETs have some promising applications as THz detectors and cameras. A majority of these applications are terrestrial applications as described in the introduction chapter. These devices unfortunately will not fill the need of low-cost large FPA detectors for all-sky missions looking for faint objects due to the CMBR. Aside from those missions, in the search for understanding our solar system, the devices do fill a need for a small mission satellite or an instrument on a larger satellite mission. The mission would be to study the atmospheric processes and properties that we do not yet understand (such as Mars and the plumes from Enceladus). By doing this science with these devices, it makes way for more missions or Instrument development for all-sky missions and makes some of the THz science more accessible.

In order to accommodate a planetary mission, this work suggests more work be done to determine the most optimized source extension and antenna length for multiple THz frequency windows (instead of 0.2 THz only in this work). It would be possible to design different pixels for different frequencies and monitor multiple different molecular species at one time.

Bibliography

A.J. Barger, et al. Submillimetre-wavelength detection of dusty star-forming galaxies at high redshift. *Nature*, 394:248–251, 2008. doi: 10.1038/28338. 1.2.4, 1.4.2

et al. ALMA Partnership. *The Astrophysical Journal Letters*, 808(1), 2015. 1.2.3

Antonello Andreone, Leopoldo Angrisani, Giovanni Cavallo, Annalisa Liccardo, and Gian Paolo Papari. *THz Measurement Systems*, pages 1–32. 07 2016. ISBN ISBN 978-953-51-4248-5. doi: 10.5772/63734. (document), 1.7

Jochem Baselmans. Kinetic inductance detectors. *Journal of Low Temperature Physics*, 167 (3):292–304, May 2012. ISSN 1573-7357. doi: 10.1007/s10909-011-0448-8. URL `https://doi.org/10.1007/s10909-011-0448-8`. 1.4.3

Dominic J. Benford, Christine A. Allen, Alexander S. Kutyrev, Samuel H. Moseley, Richard A. Shafer, James A. Chervenak, Erich Grossman, Kent D. Irwin, John M. Martinis, and Carl D. Reintsema. Superconducting transition edge sensor bolometer arrays for submillimeter astronomy. In *Proc. Int. Symp. on Space and THz Technology*, 2000. 1.4.2

Mark Birkinshaw. The sunyaevâĂŞzelâĂŹdovich effect. *Physics Reports*, 310(2):97 – 195, 1999. ISSN 0370-1573. doi: https://doi.org/10.1016/S0370-1573(98)00080-5. URL `http://www.sciencedirect.com/science/article/pii/S0370157398000805`. 1.2.6

Jamie Bock. The Future of Far-Infrared Detectors for Space Space-Ready Far-Infrared Detectors Today, 2008. URL `http://www.ipac.caltech.edu/irspace/pres/bock.pdf`. 1.4.2

D. B. But, D. Coquillat, N. Dyakonova, F. Teppe, S. Ruffenach, W. Knap, P. Kopyt, and J. Marczewski. Substrate optimization for a planar antenna of terahertz Si field effect transistor detectors. *2016 21st Int. Conf. Microwave, Radar Wirel. Commun. MIKON 2016*, pages 0–2, 2016. doi: 10.1109/MIKON.2016.7492047. 6.2, 6.2

John Byrd. THz Detectors, 2008. URL `http://uspas.fnal.gov/materials/10MIT/4_THzDetectors.pdf`. Presentation Slides. Accessed: 04/16/19. 1.4.5

JE Carlstrom, PAR Ade, KA Aird, BA Benson, LE Bleem, S Busetti, CL Chang, E Chauvin, H-M Cho, TM Crawford, et al. The 10 meter south pole telescope. *Publications of the Astronomical Society of the Pacific*, 123(903):568, 2011. 1.4.2

Joseph J. Carr. *Practical Antenna Handbook*. McGraw-Hill, 4th edition, 2001. 3.1

Bradley W. Carroll and Dale A. Ostlie. *An Introduction to Modern Astrophysics*. 2nd (international) edition, 2007. (document), 1.1.1, 1, 2, 3, 1.1.1, 1.1, 1.1.1, 1.2, 1.1.1, 1.2.2

Olga Cherkasova, Maxim Nazarov, and Alexander Shkurinov. Noninvasive blood glucose monitoring in the terahertz frequency range. *Optical and Quantum Electronics*, 48(3):217, 2016. 1.3.3

Dan Corcos, Noam Kaminski, Evgeny Shumaker, Ofer Markish, Danny Elad, Thomas Morf, Ute Drechsler, Winnie Tatiana Silatsa Saha, Lukas Kull, Ken Wood, Ullrich R. Pfeiffer, and Janusz Grzyb. Antenna-Coupled MOSFET Bolometers for Uncooled THz Sensing. *IEEE Trans. Terahertz Sci. Technol.*, 5(6):902–913, 2015. ISSN 2156342X. doi: 10.1109/TTHZ.2015.2466470. 1

J. Anthony Murphy Creidhe O'Sullivan. *Field Guide to Terahertz Sources, Detectors, and Optics*, volume FG28 of *SPIE Field Guides*. 2012. 1

Imke de Pater. The Significance of Microwave Observations for the Planets. *Physics Reports (Review Section of Physics Letters)*, 200:1–50, 1991. 1.2.5.2

Konrad Domke and Andrzej Odon. Thermo-electric model of a pyroelectric detector. 06 2012. doi: 10.2495/HT120221. (document), 1.6

P. Dutta and P. M. Horn. Low-frequency fluctuations in solids: 1f noise. *Rev. Mod. Phys.*, 53: 497–516, 1981. ISSN 00346861. doi: 10.1103/RevModPhys.53.497. 5.3.1, 5.3.1, 5.3.1

Michael Dyakonov and Michael Shur. Shallow water analogy for a ballistic field effect transistor: New mechanism of plasma wave generation by dc current. *Phys. Rev. Lett.*, 71(15): 2465–2468, 1993. ISSN 00319007. doi: 10.1103/PhysRevLett.71.2465. 4.1, 4.1, 4.1, 4.1

Mikhail Dyakonov and Michael Shur. Detection, mixing, and frequency multiplication of terahertz radiation by two-dimensional electronic fluid. *IEEE Trans. Electron Devices*, 43 (3):380–387, 1996. ISSN 00189383. doi: 10.1109/16.485650. 4.1, 4.1, 4.1, 4.1, 4.1

R. Moreno M. Allen S. Gulkis P. Hartogh J.-M. Krieg A. Maestrini I. Mehdi A. Coustenis E. Lellough, S. Vinatier. Sounding of Titan's atmosphere at submillimeter wavelengths from an orbiting spacecraft. *Planetary and Space Science*, 58:1724–1739, 2010. 1.2.5.3

Duncan Farrah, Kimberly Ennico Smith, David Ardila, Charles M. Bradford, Michael J. DiPirro, Carl Ferkinhoff, Jason Glenn, Paul F. Goldsmith, David T. Leisawitz, Thomas Nikola, Naseem Rangwala, Stephen A. Rinehart, Johannes G. Staguhn, Michael Zemcov, Jonas Zmuidzinas, James Bartlett, Sean J. Carey, William J. Fischer, Julia R. Kamenetzky, Jeyhan Kartaltepe, Mark D. Lacy, Dariusz C. Lis, Lisa S. Locke, Enrique Lopez-Rodriguez, Meredith MacGregor, Elisabeth Mills, Samuel H. Moseley, Eric J. Murphy, Alan Rhodes, Matthew J. Richter, Dimitra Rigopoulou, David B. Sanders, Ravi Sankrit, Giorgio Savini, John-David Smith, and Sabrina Stierwalt. Review: far-infrared instrumentation and technological development for the next decade. *Journal of Astronomical Telescopes, Instruments, and Systems*, 5(2):1 – 34, 2019. doi: 10.1117/1.JATIS.5.2.020901. URL `https://doi.org/10.1117/1.JATIS.5.2.020901`. (document), 1.2.3, 1.2.6, 1.5, 1.5, 5.3.1, 5.4, 6.1

Gregory J Fertig. Evaluation of MOSFETs for Terahertz Detector Arrays. Master's thesis, Rochester Institute of Technology, 2014. URL `http://scholarworks.rit.edu/theses/8302/`. (document), 1, 1.2.5, 1.3.1, 1.3.2, 1.3.3, 1.4.1, 1.5, 2.1, 2.2, 3.2.1, 3.2.1, 4, 4.1, 4.1, 4.1, 4.1, 4.1, 4.1, 4.4, 5.2.3

Adalyn Fyhrie, Jonas Zmuidzinas, Jason Glenn, Peter Day, Henry G. LeDuc, and Christopher McKenney. Progress towards ultra sensitive KIDs for future far-infrared missions: a focus on recombination times. In Jonas Zmuidzinas and Jian-Rong Gao, editors, *Millimeter, Submillimeter, and Far-Infrared Detectors and Instrumentation for Astronomy IX*, volume 10708, pages 534 – 541. International Society for Optics and Photonics, SPIE, 2018. doi: 10.1117/12.2312867. URL `https://doi.org/10.1117/12.2312867`. 1.4.6

P. F. Goldsmith, C. M. Bradford, M. Dragovan, B. Khayatian, K. Huffenberger, I. J. O'Dwyer, K. Górski, H. W. Yorke, J. Zmuidzinas, C. Paine, C. Satter, and R. Lee. CALISTO: a cryogenic far-infrared/submillimeter observatory. In Howard A. MacEwen and James B. Breckinridge, editors, *UV/Optical/IR Space Telescopes: Innovative Technologies and Concepts III*, volume 6687, pages 261 – 273. International Society for Optics and Photonics, SPIE, 2007. 1.2.6

M. A. Gurwell, E. A. Bergin, G. J. Melnick, M. L. N. Ashby, G. Chin, N. R. Erickson, P. F. Goldsmith, M. Harwit, J. E. Howe, S. C. Kleiner, D. G. Koch, D. A. Neufeld, B. M. Patten, R. Plume, R. Schieder, R. L. Snell, J. R. Stauffer, V. Tolls, Z. Wang, G. Winnewisser, and Y. F. Zhang. Submillimeter Wave Astronomy Satellite Observations of the Martian Atmosphere: Temperature and Vertical Distribution of Water Vapor. , 539:L143–L146, August 2000. doi: 10.1086/312857. 1.2.5.1

A. Gutin, V. Kachorovskii, A. Muraviev, and M. Shur. Plasmonic terahertz detector response at high intensities. *Journal of Applied Physics*, 112(1):014508, 2012. 4.1

Moeen Hassanalieragh. *High Performance THz Detection in Standard CMOS Technology*. PhD thesis, University of Rochester, 2019. 3.4, 4.3

Thomas Henning and Dmitry Semenov. Chemistry in Protoplanetary Disks. *Chemical Reviews*, 113(12):9016–9042, December 2013. doi: 10.1021/cr400128p. 1.2.3

F.N. Hooge. 1/F Noise Sources. *IEEE Trans. Electron Devices*, 41(11):1926–1935, 1994. ISSN 0018-9383. doi: 10.1109/16.333808. 5.3.1, 5.3.1

Jack D. Horowitz. Characterization of Optimized Si-MOSFETs for Terahertz Detection, 2017. 1, 1.3.2, 1.5, 2.1, 3.2.3, 4

Paul Horowitz and Hill Winfield. *The Art Of Electronics*. Press Syndicate of the University of Cambridge, 2nd edition, 1980. 1.4.1, 2.1, 2.2, 2.2, 2.2, 2.3, 2.4, 2.4, 2.4

S. M. Hörst. Titan's atmosphere and climate. *Journal of Geophysical Research: Planets*, 122: 432–482, 2017. doi: 10.1002/2016JE005240. 1.2.5.3

Axel Zeitler Kai-Eric Peiponen and Makoto Kuwata-Gonokami, editors. *Terahertz Spectroscopy and Imaging*. Springer, 2013. 1.3.3

BURCU KARAGOZ, HAKAN ALTAN, and KIVANC KAMBUROGLU. Terahertz pulsed imaging study of dental caries. In *Medical Laser Applications and Laser-Tissue Interactions VII*, page 95420N. Optical Society of America, 2015. 1.3.3

Jack Horowitz Daniel Newman Kenneth Fourspring Andrew Sacco-Paul Lee Craig McMurtry Judith Pipher Zeljko Ignjatovic Moeen Hassanalieragh Katherine E. Seery, Zoran Ninkov. Characterization of si-mosfet cmos devices for detection at 170 to 250 ghz, 2018. URL `https://doi.org/10.1117/12.2288454`. 3.2.3

et al. Kevin France. Co/h_2 abundance ratio âĽĹ 10âĹŠ4 in a protoplanetary diskâĹů. *The Astrophysical Journal*, 794(2), 2014. 1.2.3

W. Knap, V. Kachorovskii, Y. Deng, S. Rumyantsev, J.-Q. Lü, R. Gaska, M. S. Shur, G. Simin, X. Hu, M. Asif Khan, C. A. Saylor, and L. C. Brunel. Nonresonant detection of terahertz radiation in field effect transistors. *Journal of Applied Physics*, 91(11):9346–9353, 2002. 4, 4.2, 4.2

W Knap, S Rumyantsev, M S Vitiello, D Coquillat, S Blin, N Dyakonova, M Shur, F Teppe, a Tredicucci, and T Nagatsuma. Nanometer size field effect transistors for terahertz detectors. *Nanotechnology*, 24:214002, 2013. ISSN 1361-6528. doi: 10.1088/0957-4484/24/21/214002. URL `http://www.ncbi.nlm.nih.gov/pubmed/23618776`. 4.1, 4.1, 4.1

David Henry Lesser. *Techniques for Next Generation Terahertz Telescopes and Telecommunications Systems*. PhD thesis, University of Arizona, 2019. 1

R A Lewis. A review of terahertz detectors. *Journal of Physics D: Applied Physics*, 52(43): 433001, aug 2019a. 1.4.1, 1.4.2

R A Lewis. A review of terahertz detectors. *Journal of Physics D: Applied Physics*, 52(43): 433001, aug 2019b. doi: 10.1088/1361-6463/ab31d5. URL https://doi.org/10.1088%2F1361-6463%2Fab31d5. 1

Darek Lis. CSO Atmospheric Transmission Interactive Plotter, 2007. URL http://www.submm.caltech.edu/cso/weather/atplot.shtml. 1.2.5

Kh Lundberg. Noise Sources in Bulk CMOS. pages 1–12, 2002. doi: 10.1.1.151.7933. URL http://web.mit.edu/klund/www/papers/UNP_noise.pdf. 5.3.1, 5.3.1

Philip R. Maloney, Nicole G. Czakon, Peter K. Day, Thomas P. Downes, Ran Duan, Jiansong Gao, Jason Glenn, Sunil R. Golwala, Matt I. Hollister, Henry G. LeDuc, Benjamin A. Mazin, Sean G. McHugh, Omid Noroozian, Hien T. Nguyen, Jack Sayers, James A. Schlaerth, Seth Siegel, John E. Vaillancourt, Anastasios Vayonakis, Philip Wilson, and Jonas Zmuidzinas. Music for sub/millimeter astrophysics. In *Proc. SPIE*, 2010. doi: 10.1117/12.857751. URL https://doi.org/10.1117/12.857751. 1.4.3

Benjamin Mazin. *Microwave Kinetic Inductance Detectors*. PhD thesis, California Institute of Technology, 2004. (document), 1.4.3, 1.5

Benjamin A. Mazin. Microwave kinetic inductance detectors: The first decade. *AIP Conference Proceedings*, 1185(1):135–142, 2009. doi: 10.1063/1.3292300. URL https://aip.scitation.org/doi/abs/10.1063/1.3292300. 1.4.3

Donald a. Neamen. *Electronic Circuit Analysis and Design*. McGraw-Hill Education, 2nd edition, 2000. ISBN 0072409576. URL http://www.mhhe.com/engcs/electrical/neamen01/etext/ch05.pdf. 2.3

The Editors of Encyclopaedia Britannica. Bohr model. https://www.britannica.com/science/Bohr-model, Jan 2020. Encyclopedia Britannica. 1.1.1, 1.1.1

a. Ortiz-Conde, F. J. García Sánchez, J. J. Liou, a. Cerdeira, M. Estrada, and Y. Yue. A review of recent MOSFET threshold voltage extraction methods. *Microelectron. Reliab.*, 42: 583–596, 2002. ISSN 00262714. doi: 10.1016/S0026-2714(02)00027-6. 2.5

Emma Pickwell-MacPherson and Vincent P. Wallace. Terahertz pulsed imaging—a potential medical imaging modality? *Photodiagnosis and Photodynamic Therapy*, 6(2):128 – 134, 2009. ISSN 1572-1000. doi: https://doi.org/10.1016/j.pdpdt.2009.07.002. URL `http://www.sciencedirect.com/science/article/pii/S1572100009000611`. 1.3.3

Emilio C. Bortolucci Luis Olavo T. Fernandes Grigory I. Kropotov Amauri S. Kudaka Nelson Machado RogÃľrio Marcon Valery Nicolaev Pierre Kaufmann1, AndrÃľ Abrantes and Alexander Timofeevsky. Space and Ground-Based New Tools for THz Solar Flare Observations. 2015. 1.4.5

Robert F. Pierret. *Volume I: Semiconductor Fundamentals.* Addison-Wesley Modular Series on Solid State Devices. Addison-Wesley Publishing Company, Inc., 2nd edition, 1988. 2.2, 2.3

Robert F. Pierret. *Volume IV: Field Effect Devices.* Addison-Wesley Modular Series on Solid State Devices. Addison-Wesley Publishing Company, Inc., 2nd edition, 1990. 2.2, 2.2, 2.2, 2.4, 2.4, 2.4, 2.5, 2.5

V. V. Popov, D. M. Ermolaev, K. V. Maremyanin, N. a. Maleev, V. E. Zemlyakov, V. I. Gavrilenko, and S. Yu Shapoval. High-responsivity terahertz detection by on-chip InGaAs/-GaAs field-effect-transistor array. *Appl. Phys. Lett.*, 98(October), 2011. ISSN 00036951. doi: 10.1063/1.3573825. 4.1

A. Redo-Sanchez and X. Zhang. Terahertz science and technology trends. *IEEE Journal of*

Selected Topics in Quantum Electronics, 14(2):260–269, March 2008. ISSN 1077-260X. doi: 10.1109/JSTQE.2007.913959. 1

P. L. Richards. Bolometers for infrared and millimeter waves. *J. Appl. Phys.*, 76(1994):1–24, 1994. ISSN 00218979. doi: 10.1063/1.357128. 1.4.1

F. Rogalski, A.; Sizov. Organic field-effect transistors. *Opto-Electronics Rev.*, 18(3):121–136, 2011. ISSN 1230-3402. doi: 10.2478/s11772. URL `http://www.unm.edu/~solgel/CourseStuff/HorowitzAdvMater1998.pdf`. (document), 1, 1.2.6, 1.4.1, 1.4.4, 1.4.5, 1.4.5, 1.4, 1.4.6, 1.5, 5.3.1

Min Woo Ryu, Jeong Seop Lee, Kibog Park, Wook Ki Park, Seong Tae Han, and Kyung Rok Kim. Photoresponse enhancement of plasmonic terahertz wave detector based on asymmetric silicon MOSFETs with antenna integration. *Jpn. J. Appl. Phys.*, 53, 2014. ISSN 13474065. doi: 10.7567/JJAP.53.04EJ05. 4

Hideo Sagawa. Terahertz remote-sensing of the venusian atmosphere: Observations using the nobeyama millimeter array. *Journal of the National Institute of Information and Communications Technology*, 55(1), 2008. 1.2.5.2

Smithsonian Astrophysical Observatory SAO. Scientific prospects for a terahertz telescope. `https://www.cfa.harvard.edu/srlab/secure/rxlabTerahertzScience.html`, 2017. Accessed: 2018-11-08. 1, 1.2.3, 1.2.4

J. Schlaerth, A. Vayonakis, P. Day, J. Glenn, J. Gao, S. Golwala, S. Kumar, H. LeDuc, B. Mazin, J. Vaillancourt, and J. Zmuidzinas. A Millimeter and Submillimeter Kinetic Inductance Detector Camera. *Journal of Low Temperature Physics*, 151:684–689, 2008. 1.4.3, 1.4.4

Sherif Sharroush, Y.s Abdalla, Ahmed Dessouki, and El-Sayed El-Badawy. Subthreshold mosfet transistor amplifier operation. In *Design and Test Workshop (IDT), 2009 4th International*, pages 1–6, 11 2009. ISBN 978-1-4244-5748-9. doi: 10.1109/IDT.2009.5404144. 2.3

Hani Mahmoud Sherry. *Terahertz Circuits and Systems in CMOS*. PhD thesis, University of Wuppertal and University of Lille 1, 2013. 1.3.2, 1.3.3

Peter H. Siegel. THz instruments for space. *IEEE Trans. Antennas Propag.*, 55(11):2957–2965, 2007. ISSN 0018926X. doi: 10.1109/TAP.2007.908557. 1.4.2

P.H. Siegel. Terahertz technology. *IEEE Trans. Microw. Theory Tech.*, 50(3):910–928, 2002. ISSN 00189480. doi: 10.1109/22.989974. URL `http://ieeexplore.ieee.org/ielx5/22/21335/00989974.pdf?tp=&arnumber=989974&isnumber=21335$\delimiter"026E30F$nhttp://ieeexplore.ieee.org/lpdocs/epic03/wrapper.htm?arnumber=989974`. 1.4.1, 1.4.2, 1.4.4, 1.4.5

F Sizov. Terahertz radiation detectors: the state-of-the-art. *Semiconductor Science and Technology*, 33(12):123001, oct 2018. 1, 1.2.6, 1.4.2

Gordon J. Stacey. Thz low resolution spectroscopy for astronomy. *IEEE Transactions on Terahertz Science and Technology*, 1:241–255, 2011. 1, 1.2.4, 1.2.5.1

Ben G. Streetman and Sanjay Kumar Banerjee. *Solid State Electronic Devices*. Pearson Education Inc., sixth edition, 2006. (document), 2.1, 2.3, 2.3, 4.2

Bruce Swinyard and Wolfgang Wild. Far-infrared imaging and spectroscopic instrumentation. *ISSI Sci. Rep. Ser.*, 9:261–281, 2013. doi: 10.1007/978-1-4614-7804-1_14. 1

S. M. Sze and Kwok K. Ng. *Physics of Semiconductor Devices*. John Wiley & Sons, Inc., 3rd edition, 2007. 2.1, 2.3, 2.5

Paul Szypryt. *Development of Microwave Kinetic Inductance Detectors for Applications in Optical to Near-IR Astronomy*. PhD thesis, University of California, Santa Barbara, 2017. 1.4.3

R. Tauk, F. Teppe, S. Boubanga, D. Coquillat, W. Knap, Y. M. Meziani, C. Gallon, F. Boeuf, T. Skotnicki, C. Fenouillet-Beranger, D. K. Maude, S. Rumyantsev, and M. S. Shur. Plasma wave detection of terahertz radiation by silicon field effects transistors: Responsivity and

noise equivalent power. *Appl. Phys. Lett.*, 89:3–5, 2006. ISSN 00036951. doi: 10.1063/1.2410215. 4.1, 4.1

Jonathan Tennyson. *Astronomical Spectroscopy*. Imperial College Press, 1st edition, 2005. (document), 1.1.2, 1.1.2, 1.1.3, 1.1

Christopher K. Walker, Craig Kulesa, Christopher Groppi, and Dathon Golish. Future prospects for THz spectroscopy. In William D. Duncan, Wayne S. Holland, Stafford Withington, and Jonas Zmuidzinas, editors, *Millimeter and Submillimeter Detectors and Instrumentation for Astronomy IV*, volume 7020, pages 320 – 327. International Society for Optics and Photonics, SPIE, 2008. doi: 10.1117/12.790286. URL `https://doi.org/10.1117/12.790286`. 1

C.K. Walker. *Terahertz Astronomy*. CRC Press Taylor & Francis Group, 2016/2019. (document), 1, 1.1.1, 1.2.2, 1.2, 1.3

V. P. Wallace, A. J. Fitzgerald, B. Robertson, E. Pickwell, and B. Cole. Development of a hand-held tpi system for medical applications. In *IEEE MTT-S International Microwave Symposium Digest, 2005.*, pages 3 pp.–639, 2005. 1.3.3

Susanna L. Widicus Weaver. Millimeterwave and submillimeterwave laboratory spectroscopy in support of observational astronomy. *Annual Review of Astronomy and Astrophysics*, 57 (1):79–112, 2019. doi: 10.1146/annurev-astro-091918-104438. URL `https://doi.org/10.1146/annurev-astro-091918-104438`. 1, 1.4.6

Adam L. Woodcraft. Detectors for sub-millimetre continuum astronomy. *Nucl. Instruments Methods Phys. Res. Sect. A Accel. Spectrometers, Detect. Assoc. Equip.*, 604:30–33, 2009. ISSN 01689002. doi: 10.1016/j.nima.2009.01.082. 1.4.1, 1.4.2

Kasai Yasuko and Seta Takamasa. Atmospheric Propagation Model of Terahertz-Wave. *Journal of the National Institute of Information and Communications Technology*, 55(1), 2008. 1, 1.2.5

D. Yavorskiy, J. Marczewski, K. Kucharski, P. Kopyt, W. Gwarek, M. Ratajczyk, W. Knap, B. Pietka, and J. Lusakowski. A THz scanner based on planar antenna-supplied silicon field-effect transistors. *Photonics Lett. Pol.*, 4(3):100–102, 2012. ISSN 20802242. doi: 10.4302/plp.2012.3.06. 2.1

Trond Ytterdal, Yuhua Cheng, and Tor a Fjeldly. *Device Modeling for Analog and RF CMOS Circuit Design*. John Wiley & Sons, Ltd, 2003. ISBN 9780471498698. 2.1

Audrey Zak, Michael a. Andersson, Maris Bauer, Jonas Matukas, Alvydas Lisauskas, Hartmut G. Roskos, and Jan Stake. Antenna-integrated 0.6 THz FET direct detectors based on CVD graphene. *Nano Lett.*, 14:5834–5838, 2014. ISSN 15306992. doi: 10.1021/nl5027309. 4.1

Chao Zhang. *Optical simulation of terahertz antenna using finite difference time domain method*. PhD thesis, Rochester Institute of Technology, 2014. URL `http://scholarworks.rit.edu/theses/8738/`. 3.2.2

B Zhu, Y Chen, K Deng, W Hu, and Z S Yao. Terahertz Science and Technology and Applications. *PIERS Proc.*, pages 1166–1170, 2009. 1, 1.3.2, 1.3.3